Ultrasensitive and Hysteresis-free Magnetic Sensing using Magnetic Tunnel Junctions

by

Guanyang He

B.S., Wuhan University, 2014

A Dissertation submitted in partial fulfillment of the
requirements for the degree of Doctor of Philosophy
in the Department of Physics at Brown University

Providence, Rhode Island

February 2021

This Dissertation by Guanyang He is accepted in its present form by

the Department of Physics as satisfying the dissertation requirement for

the Degree of Doctor of Philosophy

Date…………………. ……………………………………………………………

Professor Gang Xiao, Advisor

Recommended to the Graduate Council

Date…………………. ……………………………………………………………

Professor Alexander Zaslavsky, Reader

Date…………………. ……………………………………………………………

Professor Jia Li, Reader

Approved by the Graduate Council

Date…………………. ……………………………………………………………

Andrew G. Campbell, Dean of the Graduate School

Vita

Guanyang He was born in 1992, China. He received his B.S.

in Physics from Wuhan University, China in 2014.

The research for this thesis started in 2016. His scientific publications include:

PUBLICATIONS

Size-dependent plasmon relaxation dynamics and saturable absorption in gold nanorods, Qiu, Yun-Hang, Fan Nan, Ya-Fang Zhang, Jia-Hong Wang, **Guan-Yang He**, Li Zhou, and Qu-Quan Wang, *Journal of Physics D: Applied Physics* 49, no. 18 (2016). [doi.org/10.1088/0022-3727/49/18/185107]

PicoTesla magnetic tunneling junction sensors integrated with double staged magnetic flux concentrators, **He, Guanyang**, Yiou Zhang, Lijuan Qian, Gang Xiao, Qiang Zhang, J. Carlos Santamarina, Tadeusz W. Patzek, and Xixiang Zhang, *Applied Physics Letters* 113, no. 24 (2018). [doi.org/10.1063/1.5052355]

Magnetotransport and electronic noise in superparamagnetic magnetic tunnel junctions, Zhang, Yiou, **Guanyang He**, Xixiang Zhang, and Gang Xiao, *Applied Physics Letters* 115, no. 2 (2019). [doi.org/10.1063/1.5110715]

Nonhysteretic Vortex Magnetic Tunnel Junction Sensor with High Dynamic Reserve, **He, Guanyang**, Yiou Zhang, and Gang Xiao, *Physical Review Applied* 14, no. 3 (2020). [doi.org/10.1103/PhysRevApplied.14.034051]

Magnetic Tunnel Junction based Gradiometer for Detection of Cracks in Cement, **Guanyang He**, Yiou Zhang, Yuebin Hu, Xixiang Zhang, and Gang Xiao, *submitted to Applied Physics Letters*

PRESENTATIONS

Contributed talk “PicoTesla Magnetic Sensors based on Magnetic Tunneling Junctions with Double-staged Flux Concentrators” at the APS March Meeting, 2019.

Poster presentation “Effect of Magnetic Domain Structures on Magnetic Sensing Properties of Magnetic Tunnel Junctions” at the MMM Conference, 2019.

HONORS AND AWARDS

2018 Forrest Award (Excellent work in experimental apparatus, Brown University)

2014 Honor undergraduate of “National Plan for Top-notch Students in Basic Sciences” program

Acknowledgment

First of all, I want to thank Professor Gang Xiao from the bottom of my heart, who has been my advisor since I became a graduate student at Brown University. He has been helpful in both my life and research, who is always there for all his students and me. Whenever I run into trouble in my experiments, I can always resort to him for guidance and inspiration. I am so grateful to work in his laboratory to study all the exciting projects of spintronics.

I would like to sincerely thank all my labmates working together with me in Gang's group, Shutong Wang, Wenzhe Chen, Lijuan Qian, Yiou Zhang, Kang Wang, Shiyu Zhou, for their assistance in completing all of my projects, and their advice in our daily discussions.

I also wish to thank Professor Alexander Zaslavsky and Professor Jia Li, for reading my thesis and serving as members of my thesis defense committee. I thank Michael Jibitsky, manager of the microelectronics facilities, for helping me in using all the equipment in the Microelectronics Facility.

Last but not least, my parents have always been greatly supportive for my pursuit of learning and research with their love and attention. To them, I dedicate this thesis.

Abstract

This project's primary objective is to apply a quantum device called the magnetic tunnel junction (MTJ) for ultrasensitive magnetic field sensing. Towards this goal, we have systematically improved the MTJ system using novel physical ideas. Firstly, by optimizing the magnetron sputtering conditions of the magnetic flux concentrator (MFC), we managed to enhance the field detectability of MTJ to unprecedented $30\ \mathrm{pT}/\sqrt{\mathrm{Hz}}$ at $10\ \mathrm{kHz}$.

As another way to boost sensitivity, we have also tuned the magnetic anisotropy in the MTJ free layer, where an interfacial perpendicular magnetic anisotropy (PMA) is induced. By tuning PMA with temperature, a compensation between PMA and demagnetization energy enhances the MTJ sensitivity to 1.2 %/Oe. Besides, an interesting voltage-dependent random telegraph noise is discussed.

As the MTJ sensitivity is greatly enhanced by MFC and PMA, the intrinsic hysteresis still prevents MTJ from detecting small fields. Therefore we have attempted to eliminate the hysteresis at a fundamental level using a superparamagnetic free layer. We experimentally observed a transition from ferromagnetic to superparamagnetic states by raising the temperature, and the sensor in the latter state is non-hysteretic with good sensitivity.

We have also resorted to the vortex magnetic states, where a topologically protected vortex magnetization in the MTJ free layer can evolve without hysteresis. The generation of vortex magnetization was revealed using the MUMAX simulation package first. We then experimentally fabricated vortex MTJ sensors, with outstanding sensing performances such as a sensitivity of 0.3 %/Oe, a thermal stability of 400 ppm/K, and an extensive dynamic range of 200 Oe.

To demonstrate the application prospect for MTJ sensors with our improvements, we have developed a magnetic gradiometer prototype and applied the device in the wellbore crack detection. The gradiometer can detect defects with a large stand-off distance of 22 mm.

In brief, we have used MFC and PMA as methods to raise the sensitivity of MTJ. We have taken advantage of the superparamagnetic effect and vortex magnetic states to eliminate ferromagnetic hysteresis. From these results, we have generalized the scaling relation between the magnetic sensitivity and noise of MTJs in the ferromagnetic, superparamagnetic and vortex states, to propose that hysteresis elimination is indispensable for a favorable linear scaling.

Contents

List of Figures

Chapter 1 Introduction

1.1 Motivation

Spintronics is a new breed of study about the intrinsic spin of electrons in electronic technology, widely applied in chip-scale information storage and processing, spintronic immunoassay, non-destructive evaluation, and industrial metrology [1-4]. Relevant spintronics devices have enabled biomedical imaging or magnetoresistive sensors, with their attractive features such as adjustable sensing properties, broad operating conditions, compatibility with complementary metal-oxide-semiconductor (CMOS) and industrial mass production. Unlike conventional electronic devices that rely on the electron charge to control its motions for information transfer, spintronics uses the spin degree of freedom of electrons to build a close connection between magnetic and electric phenomena.

Due to the quenching of the orbital angular momentum, in a ferromagnetic thin film, the electron spin polarization is directly related to the magnetic moment of the material, which can then be manipulated by external magnetic fields or interfacial spin-orbit torques. Building on this fact, in a thin-film structure with an insulating layer sandwiched by two ferromagnetic layers, the theory of tunneling magnetoresistance (TMR) was first proposed by Julliere in 1975[5]. Since electrons with different spin polarizations also experience different electron-atom scattering in ferromagnets, the giant magnetoresistance (GMR) effect was later discovered in 1988. Afterward, it led to a new thin-film device called spin valves, whose core is a sandwich structure of a non-magnetic metal between two ferromagnetic layers[6]. Following the discovery of GMR in metallic multilayers, the magnetic tunnel junction (MTJ) as a TMR device is realized later, consisting of an amorphous aluminum oxide insulating barrier and two ferromagnetic electrodes, with an MR value around 20%[7]. Later on, the MgO insulating barriers are implemented in MTJs to give 100% MR, due to a special coherent tunneling effect. As the MgO-based MTJ replaced the intermediate metal of spin valves with an insulating layer to magically achieve such improvement[8,9], we will continue to work on it through this project.

In the core structure of an MTJ, the decaying rate of tunneling current is dependent on the relative spin polarization between two ferromagnetic layers, which results in TMR. To be more precise, as shown in the Figure1.1, electrons tunnel through an insulating tunnel barrier between two electrodes, where one is defined as the free layer and the other as the reference layer. By changing the relative magnetization directions between these two electrodes, the junction resistance can be changed correspondingly, to give a high resistance at antiparallel "AP" state and low resistance at parallel "P" state. In the application of read-write heads in data storage devices, the high and low resistance state of MTJ is used as a new way to represent logic "one" and "zero", which turns out to be a non-volatile and energetically efficient device.

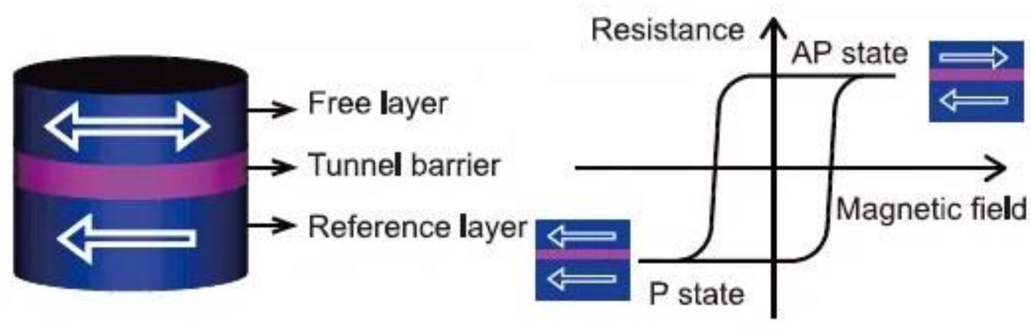

Figure 1. 1 The principle of tunneling magnetoresistance effect. A typical MTJ thin-film device is shown on the left with its core layers, and on the right is its transfer curve under magnetic fields. In the "AP" state for antiparallel magnetizations, the device shows high resistance, while in the "P" parallel state it shows low resistance.

From all properties mentioned above, the high magnetoresistance ratio is a superior property that allows the MgO-based MTJs to generate large signals in response to a weak external magnetic field[10,11]. This implies its great potential to be a magnetic field sensor. As many aspects such as sensitivity, frequency response, size, and power consumption are all needed to decide the suitable sensor for specific applications, below is a comparison among different magnetic field sensors. Ultra-sensitive magnetometers such as nitrogen-vacancy centers, optically pumped magnetometer, and SQUID have reached detectability of few $fT/\sqrt{Hz}$ [12-15]. Their shortcoming is the incapability of miniaturization for industrial fieldwork, to operate without additional requirements of laser, magnetic shielding, or cooling dewar. Giant magneto-impedance and fluxgate magnetometer have detectability around $pT/\sqrt{Hz}$. Nevertheless they are relatively large in few centimeters with the need of high frequency excitation current, which is short of spatial resolution [16-18]. Their operating conditions at quasi-DC frequency also mean inconvenient long measuring time.

Comparatively, solid-state sensors with wide bandwidth up to GHz and micrometer size pose solutions of better utility, like anisotropic, giant, and tunneling magnetoresistance sensors. The first two sensors have field noise from 10 to 100 $nT/\sqrt{Hz}$, but low sensitivities (0.05%/Oe), small dynamic range (10Oe), or low resistance-area product ($0.05\Omega \cdot \mu m^2$) [19-24]. To be mounted onto an integrated circuit, they give rise to parasitic resistance or non-negligible preamplifier noise. Tunneling magnetoresistance sensors like MTJ generally have higher sensitivity and better operational characteristics. It is noteworthy for its high sensitivity, ease-of-use, robustness, small size, low cost, and power consumption, which are favorable to bridge the gap between sophisticated technology and practical applications[25].

Nevertheless, one challenge for MTJ is to reach sensitivity beyond a state-of-art picoTesla limit. For magnetic resonance imaging applications, a miniaturized magnetometer with femtoTesla detectability can immediately make the imaging of the human brain activities possible, and MTJ has such potential. Combing MTJ with auxiliary devices like a magnetic flux concentrator could help. However, the integration of flux concentrators with MTJ on a microscopic scale has been another research task, where the flux concentration material needs to be extremely soft magnetically to have high permeability. In other words, by standard microfabrication methods, the material needs to be made extremely amorphous with small saturation fields, but also with relatively high magnetization to generate an amplified magnetic field. On the other hand, atomic layer engineering also improves MTJ performance to some extent, such as the replacement of the MgO barrier with $MgAl_2O_4$. Moreover, since the most limiting factor is the magnetic noise coming from the magnetization of the MTJ free layer at low frequency, introducing other possible magnetic states might lead to a better signal-to-noise ratio (SNR). A careful study about all these optimizable factors helps to exploit all the potentials in MTJs, shedding light on the best candidates for magnetic sensing.

In these efforts discussed above to improve MTJ devices, the magnetic hysteresis has been an inevitable issue as shown in Fig 1.2:[26]

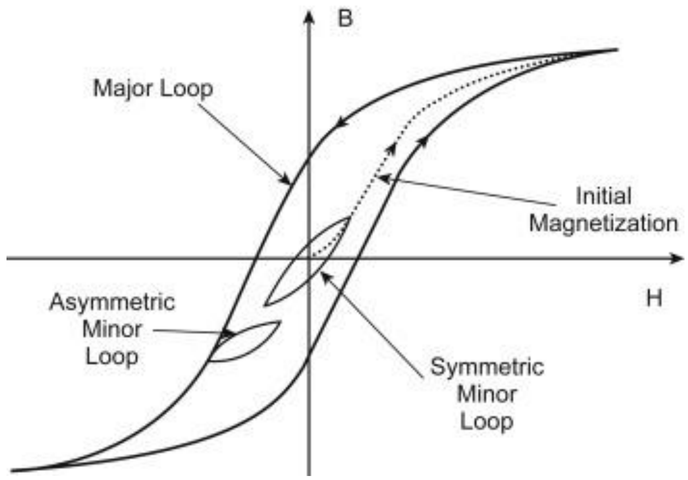

Figure 1. 2 Typical hysteretic loops of a coercive ferromagnet cited from reference [26]. The magnetic flux density B initially follows the "initial magnetization" curve under external magnetic field H, and shows coercivity in repetitive magnetic field scans. For scans of smaller ranges, different minor loops can be observed locally as shown.

When the applied magnetic field is within the hysteresis of such transfer curve, the sample's corresponding magnetization is unpredictable. The magnetization under external fields follows the initial magnetization curve initially, but will fall into specific minor loops inside the major transfer loop. Not only does the hysteresis give an uncertainty in the response for each magnetic field, but it also leads to an ultimate limitation for low-field detection. As reported in the literature, the actual sensitivity of magnetic sensors with hysteresis decreases significantly in low-field measurements, compared to their sensitivities calculated from the major transfer loop[27]. Hysteresis usually comes from pinning sites or domains in a magnetic layer, which is inert to small changes in the external field within its coercivity. Instead, it is responsive to large changes during the magnetic transfer curve measurement. As a result, the ongoing pursuit of high sensitivity in the literature about magnetic sensing must consider the impact of hysteresis. To relieve low-field measurements from the bottleneck of magnetic hysteresis, we will introduce several physical ideas such as superparamagnetism and vortex states in MTJ systems, to realize the complete elimination of hysteresis. As a result, we have achieved perfect linearity, superior field detectability in our new MTJ sensors, which can provide guidance for the designs of non-hysteretic magnetic sensors.

As the magnetic moments inside a ferromagnetic thin film are mostly influenced by the magnetic anisotropy, tuning the magnetic anisotropy turns out to be an effective way to modify the magnetic response. Voltage-controlled magnetic anisotropy has already been applied to spintronic devices as a suitable control method, and in-plane shape anisotropy is also used to reduce the hysteresis significantly[28,29]. Besides, introducing a stable perpendicular magnetic anisotropy (PMA) in MTJs helps to modify its sensing performance, and many MTJ free layer designs in literature have shown strong PMA[30,31]. Therefore, in this research we intend to study the influence of anisotropy on MTJs in more detail, to further enhance the sensing performance.

1.2 Outline

This thesis is divided into four parts. In the first part (chapters 2-3), we present an overall description of our experimental instruments, fabrication techniques; all the relative physical theory will be present, relative to the functionalities of our MTJ devices. The second part (chapter 4) describes the optimization and integration of magnetic flux concentrators into MTJ, which leads to a magnetic field sensor of ultra-low field detectability. The third part (chapter 5) will discuss two strategies to eliminate hysteresis that we tried in MTJ sensors, including superparamagnetism and vortex magnetization. Next, in chapter 6, we will discuss the use of perpendicular magnetic anisotropy (PMA) to improve the sensitivity of MTJ, and its interesting random telegraph noise (RTN) noise. In the last part (chapter 7), we will show a practical application of the new MTJ sensors in a non-destructive evaluation. A summary will be given with generalized conclusions (chapter 8). Details are enumerated as below.

Chapter 2 introduces a series of standard nanofabrication techniques in our laboratory, including magnetron sputtering, photolithography, ion milling, and magnetic field-assisted thermal annealing. The characterization devices for the magnetic moment, magnetoresistance, temperature dependence of thin-film samples include the vibrating sample magnetometer in Physical Property Measurement System (PPMS), four-terminal sensing probe station, cryogenic refrigerator, and X-ray diffraction device. Possible experimental upgrade options are discussed.

Chapter 3 gives a brief review of the theoretical development of MTJ layer structure, where we show the underlying physics process such as buffering, crystallization, interlayer magnetic coupling, and electron tunneling in this multilayer thin film. Several layer modifications in the system are introduced with their underlying mechanisms. As another important aspect of sensors, noise physics theories are reviewed, so are different types of noise in the MTJ system. New physical mechanisms applied to the MTJ system for hysteresis elimination are introduced, such as superparamagnetism and vortex magnetization. The generation of interfacial PMA and how it helps to increase the sensitivity will be discussed.

Chapter 4 introduces the fabrication of magnetic flux concentrators (MFC) and the benefits they bring to MTJs as a typical magnetic field sensor. We will report the optimized fabrication conditions to grow flux concentration materials of good quality, and the relation between the MFC concentration efficiency and its geometrical shapes. Such a study leads to a highly effective MFC, integrated with MTJ to reach a pico-Tesla AC magnetic field detectability.

In Chapter 5, we are going to discuss two methods for hysteresis elimination in MTJs. One is to induce a superparamagnetic state in MTJ by fine-tuning its free layer's thickness and morphology. Varying the measurement temperature, we can see a transition from ferromagnetic to superparamagnetic states in such MTJ. Such experiments enable us to figure out the properties of different magnetic states. Another linearization method is introducing vortex magnetization into the free layer of MTJs. Since vortex magnetization is strongly dependent on sample geometry, we will present comprehensive micromagnetic simulations to exhibit such dependency. With this guidance, we have fabricated and measured the vortex MTJ sensors experimentally. The non-hysteretic magnetic responses and noise information of them will be given. The merits and disadvantages of both methods are compared.

In Chapter 6, we modified the layer stacks of MTJ to induce PMA in the free layer. Different designs and fabrication parameters are tested to tune PMA strength. MTJs are measured under various temperatures to give a relation between PMA and the sensing performance, where a situation with compensated anisotropy between PMA and in-plane anisotropy gives high sensitivity. A clear observation of random telegraph noise (RTN) is further reported in this system, explained by a generation-recombination process.

Chapter 7 will demonstrate our magnetic gradiometer based on the MTJ research mentioned above. Such a magnetometer prototype has been readily applied to the non-destructive detection of surface cracks on a magnetic cement, with all necessary computer programming and electronics on the printed circuit board. The consistency and stability in linearized MTJ sensors result in a high common-mode rejection ratio. This gradiometer proves to be a viable solution for surface crack detections.

Chapter 8 gives an overall summary of all the previous results. The advantages and potential applications of multiple MTJ systems we developed in this thesis will be discussed, with several generalized conclusions.

Operational instructions and potential problems for all laboratory instruments will be further elaborated in the Appendix.

Chapter 2 Experimental Technique

2.1 Introduction

The synthesis of thin-film materials is a fundamental process in modern industry, with a layer thickness in the nanometer scale. A series of experiment instruments in our lab to fabricate thin-film devices like MTJ will be introduced. In the sequence of fabrication, they include the oxidation furnace baking, magnetron sputtering, photolithography, ion milling, and thermal annealing. After these procedures, we can characterize the magneto-electronic transport properties of the samples by a typical probe station with electromagnets, a commercial Physical Property Measurement System (PPMS), a noise measurement system, an atomic or magnetic force microscopy, and the X-ray crystallography. These experimental techniques are used for all the experiments in the later chapters. Detailed operational manuals of these devices are provided in the appendix.

2.2 Materials and devices preparation

2.2.1 High vacuum magnetron sputtering

Before the deposition of any material, our sputtering chamber needs to be evacuated by a cryogenic pump for one to two days after loading substrates. It usually reaches a high vacuum level of 10^{-8} torr, if not we will need to bake the chamber with a heating band to 80℃ for few hours, to get the chamber free of water vapor inside. Other methods such as pump regeneration, argon gas flushing, and repetitive evacuation can also help.

Solid debris due to a historical sputtering process is not critical because of their low vapor pressure, which does not evaporate during sputtering to contaminate the process. Other matters like Argon or Nitrogen are frequently passed into the chamber. Due to their high vapor pressure as gases at room temperature, they can be evacuated quickly by pumping. The critical remnant impurities in the chamber is water vapor, which has a medium vapor pressure and takes an arduous process to be removed. The low evaporation rate enables the water vapor adheres to the chamber wall indefinitely, if no baking or gas flushing method is applied. During magneto-sputtering, a small amount of water moisture becomes diffusive in the chamber and gets absorbed by the fabricated sample, while such moisture is detrimental to the MTJ quality and needs to be strictly avoided. Therefore, all the mentioned cleaning operations might need to be performed alternatively and repetitively several times for the exclusion of water vapor in the chamber.

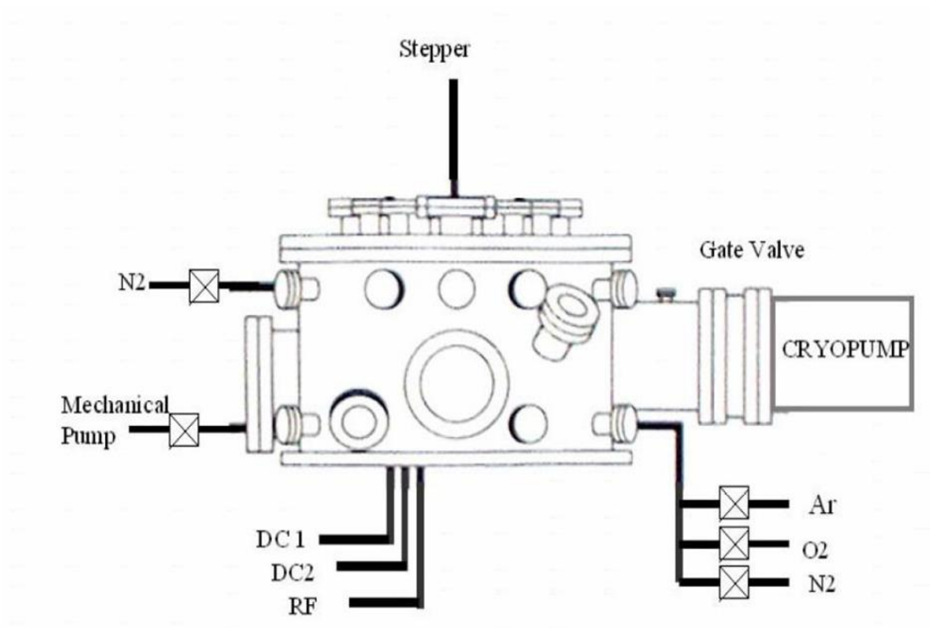

Figure 2. 1 Sketch of our magnetron sputtering high vacuum chamber used in this research. Before sputtering, the "Gate valve" opens so that the main chamber is evacuated by the "Mechanical Pump" and the "Cryopump". Several gases such as "Ar", "O_2" can be introduced into the chamber to generate plasma for sputtering. During sputtering, the sample substrate will rotate driven by the top "Stepper" motor. The "DC" and "RF" power supplies are used to ionize the processing gas or gases into a plasma to sputter targets, generating the necessary atomic vapors for thin film deposition.

As shown in Figure 2.1 above, the substrates will be loaded on the sample holders on the top of the chamber, whose self-spinning rate is 4 cycles per second. The center of the substrate holder is placed off-axis horizontally to the sputtering target below it by half of the radius, around 4cm. This rotation configuration improves the uniformity of deposition on the substrate's surface, although the deposition rate still varies by around 15% from the center to the edge of the substrate. By controlling the sputtering time, we can deposit a thin film of the target material on the substrate of a few angstroms. Unlike molecular-beam epitaxy, which can grow a single crystalline structure, our sputtering is quick and flexible, but the films grown are amorphous or polycrystalline.

Several issues should be concerned in the physical process of the sputtering. First, material growth on one substrate can contaminate several nearby substrates, as the target particles from the magnetron sputtering are scattered in every direction. For a long-time sputtering of insulating targets like Si, the deposition rate changes mostly due to the temperature rise in both targets and substrates. It can form a more uniform thin film if the sputtering switching back and forth from multiple substrates alternatively, with every sputtering thickness less than 50 nm. Long-time sputtering requires a rest time every ten minutes, to prevent the overheating of the target which would generally cause the crack of targets.

2.2.2 High-temperature oxidation process

To prepare a clean substrate before growing materials onto it by magnetron sputtering, we first put it through a baking procedure. The silicon substrates we use are polished on one side and have a thickness of 0.29 mm, 2 inches in diameter. These substrates are placed in a glass tube to be heated up to 1050℃, and then oxygen is passed into the tube for oxidation. The flow rate is set as 0.5 liters per minute, and the whole oxidation takes 24 hours. Such high-temperature oxidation enables the growth of SiO_2 insulating layers, which is the suitable insulating substrate we need. Both metallic and insulating materials can successfully grow on it without any peeling off issues. During the baking process, we can observe a color change from white Si wafers to green and finally to purple. The color is an indicator for the SiO2 layer thickness due to Brag's scattering in microscopic structures. The baking process also removes all surface impurities and organic residues, which is vital for material growth. After this oxidation, the substrate can have a clean surface for MTJ to successfully grow upon.

2.2.3 Photolithography

Lithography is an indispensable nanofabrication techniques to make microscopic structures quickly, heavily used in industry[32]. The spatial resolution of optical lithography is limited by the wavelength of the laser we use and is typically limited to 3 to 10 micrometers. To make more delicate structures we need to resort to electron beam (E-beam) lithography, which uses a high energy electron beam instead of a laser for the exposure. E-beam lithography can create much finer patterns in the nanometer scale due to its smaller beam spot[33]. Compare to traditional photolithography, it requires no physical mask as the beam directly scans over the e-beam resist coated sample with computer controls. However, such a lithography method is slow and inefficient, which takes hours to pattern only a region of several tens of micrometer square. Due to such vital limitations, we still use photolithography for all the MTJ patterning process, which allows us to make a few hundreds of MTJs on a 2-inch silicon substrate at a time.

To transfer a two-dimensional pattern designed in AutoCAD software to the thin-film we deposited on our substrate, we use the standard photolithography together with the ion etching technique, as shown in Figure 2.2.

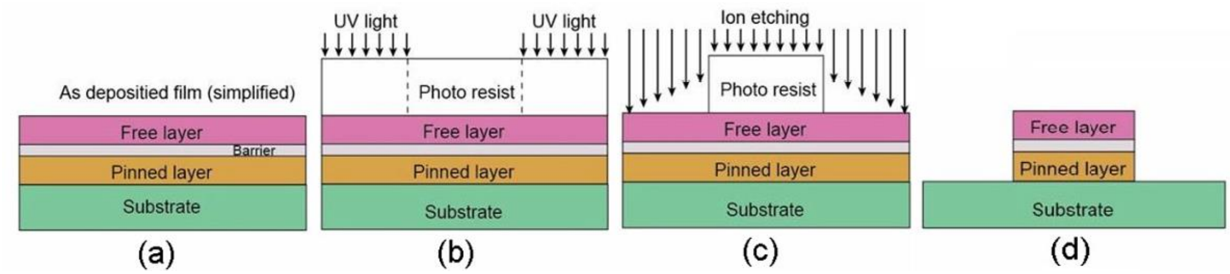

Figure 2. 2 The operations to create micro-structures on thin films, in the order from left to right. After the "Photoresist" is placed on the MTJ, its shape is modified by the ultra-violet light beam during photolithography. Then the sample surface is shaped by an ion etching process, as the region below "Photoresist" is protected from etching.

First, we use a spin coating device to spread a photoresist (PR) layer uniformly onto the surface of as-deposited thin film, as thick as few micrometers. This photoresist AZ5214 is a commercially available polymer sensitive to ultraviolet (UV) lights, denoted by the red region in Fig 2.3. After being exposed to UV lights in a positive or negative manner as shown, the region exposed to or shaded from the light could become soluble in a developer solution.

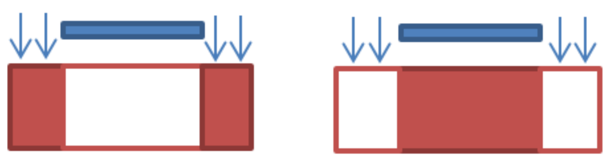

Figure 2. 3 The outcomes of positive patterning (left) and negative patterning (right). In positive pattering the photoresist (in red) exposed to ultra-violet light remains after development; in the negative pattering, the outcome is reversed.

In Figure 2.2(b), such PR after exposure to UV lights are removed by rinsing in the developer solution. As a result, only the region not exposed to UV lights will have remaining PR on top. Next, in Figure 2.2(c) an ion milling process etches all the material on the whole wafer. The region covered by PR is protected from the etching, so in the outcome in Figure 2.2(d) an intermediate MTJ structure is created.

2.2.4 Physical ion milling

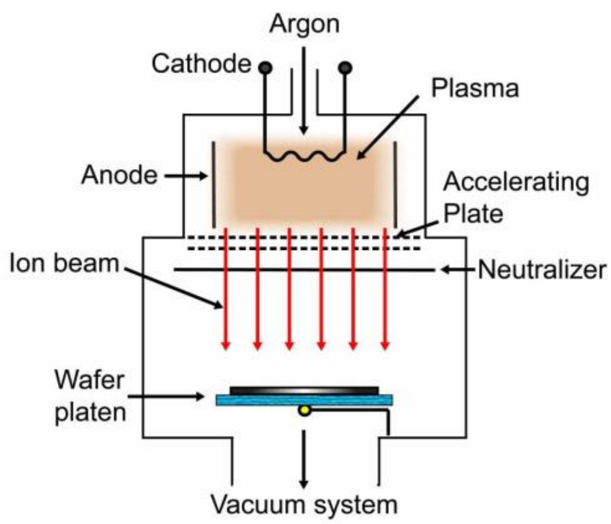

Figure 2. 4 The internal structure and working principle of ion milling device. As argon gas is passed into the chamber it is ionized by the “Cathode” and “Anode” to generate plasma. Argon ions are then accelerated by the “Accelerating Plate” to bombard the wafer. A “Neutralizer” is further installed to neutralize the accelerated ions, thus preventing charge accumulation on the wafer surface.

With the patterned PR on the sample, ion milling can transfer the pattern to the sample by indiscriminate etching. The ion milling machine and its etching principle are shown in Figure 2.4. Electrons generated by the hot cathode filament collide with argon atoms, to create a plasma of ions under a threshold voltage of 40V. A 100 G magnetic field is often used to trap the electrons for a higher ionization rate. Such argon ions accelerate towards the sample wafer under a strong electric field of 500 to 1000 volts, with a neutralizer between the ion source and the sample to prevent positive charge accumulation on the sample surface. The argon ions bombard the sample, etching different materials at nearly the same rate. The etching rate increases linearly on the ion current density, and non-linearly with the ion bombardment energy.

The ion milling angle can be changed by a lever at any time during sputtering, and there are two common etching modes. The first mode uses a constant ion milling angle of 80 degrees, with an etching rate of roughly 220 angstroms/minute. This mode is used to define the bottom electrode as the pedestal of each MTJ element out of a continuous as-deposited film, which has a large etching rate but many sidewall contaminations. This sidewall contamination is the re-deposition of etched material onto unexpected regions, sometimes shorting the junction from the side. The second mode etches at 45 degrees and 10 degrees alternatively, staying at each angle for 45 seconds. The sidewall contamination accumulated during the 45 degrees etching will be cleaned by the 10 degrees etching, since at 10 degrees the argon ions bombard in the direction parallel to the thin-film surface. Changing the etching angle back and forth helps to remove the sidewall contaminations. One etching period is defined as a 45 degrees etching followed by a 10 degrees etching, and this second mode has a lower etching rate of roughly 170 angstroms/period. It is used to define delicate MTJ structures above the bottom electrode, where sidewall contamination can easily short the whole MTJ. After a deep etching of the first mode, the sample will be patterned with PR again, and a second mode etching defines delicate structures on top of the existing structure defined in the previous etching.

2.2.5 Magnetic thermal annealing

The final step is to use the thermal annealing to define the intrinsic magnetic axis of magnetic layers in the MTJ, with a controllable temperature up to 400°C and an assistant magnetic field of 0.5 T. Thermal annealing is a common method to change the microscopic morphology of a material and its magnetic or electrical properties. For our multi-layer thin films, such a process can facilitate magnetic order formation in ferromagnetic or anti-ferromagnetic layers. Besides, it boosts the crystallization process in specific amorphous layers, removes lattice mismatches, but also accelerates the interlayer diffusion of composition element in a microscopic scale.

2.2.6 Device patterning process

With all the fabrication instruments introduced above, a series of patterning in our MTJ fabrication are enumerated here. After the magnetron sputtering to deposit the initial layer stacks, patterns will be created on the thin-film sample by a series of consecutive photolithography and ion milling treatments, as indicated step by step in the figure.

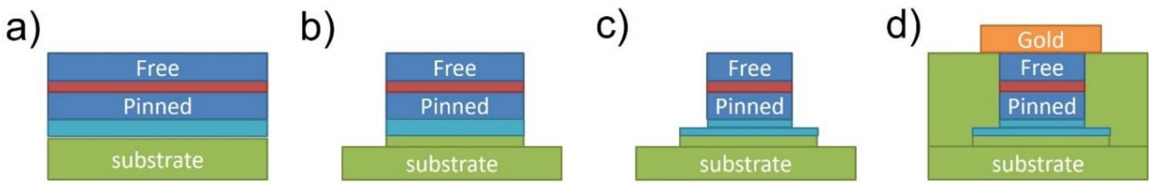

Figure 2. 5 Multiple patterning process of MTJ fabrication in the order from left to right. The bottom electrode is first defined in (b), and afterward the MTJ element is shaped in (c). In (d) the MTJ structure is finally protected by an additional SiO_2 (green) layer, and a capping gold electrode is also deposited.

The as-deposited MTJ multilayer is shown in Figure 2.5 a) on the silicon substrate, with its free layer and pinned layer separated by a red insulating barrier. Afterward, every patterning process consists of a photolithography process to cover the sample with PR of a specific pattern, and a following ion milling process to transfer the pattern to the sample surface. The operation details can be found in the Appendix.

The first patterning defines the bottom electrical contact, with Figure 2.5 b) as its outcome. The ion milling etches other irrelevant regions down into the insulating SiO_2 substrate, and the remaining region becomes the bottom contact connecting multiple MTJ elements. During ion milling, the first mode is used for large etching depth as large as 100nm. The sidewall condition is not crucial, because the MTJ structure is not created yet.

The second patterning is used to define the MTJ structure on the bottom contact, as shown in Figure 2.5 c). The MTJ elements can be of various geometrical shapes, and are connected to the bottom contact below. During ion milling, the second mode is used, because the MTJ shape needs to be precisely defined. The side-wall contamination also needs to be reduced in case of a lateral short circuit. The etching depth is typically around 70nm, which etches from the surface to the IrMn layer. Etching deeper into the bottom electrode is acceptable, unless the bottom contact becomes insulating.

Figure 2.5 d) shows the final structure for a complete MTJ sensor. After MTJs are defined through the second ion milling process, the PR on the sample should be reserved for another SiO_2 deposition. Indicated by the green structure, this SiO_2 capping serves to insulate the top and bottom electrodes and protect the MTJ from oxidation. Afterward, the PR can be removed altogether with the SiO_2 sputtered on it, opening a window for the top gold contact to contact the MTJ top electrode.

In the final structure, the external current flows from the top electrode to the bottom, amid which it tunnels through the MgO barrier. Currents flow into another nearby MTJ connected by the same bottom electrode, so that two MTJs are connected in series. The current will leave the other MTJ from its top contact, and go to the next MTJ or a gold pad wire-bonded to external electronic devices.

2.3 Physical measurement

2.3.1 Probe station

Our home-made probe station is used for the magneto-electrical measurement of thin-film samples, which can measure the resistance of micrometer-sized junctions placed in a uniform magnetic field up to 80Oe, by either two-point or four-point method. This station is set on a leveled table with a vibration reduction basement below. The probe we use is mostly made of non-magnetic material like brass to avoid any magnetic field disturbance as shown in Figure 2.6. On top of the brass base is a probe position manipulator, where three adjustment screws for three-dimensional positions of the probe respectively. A long metal rod connects the manipulator with the probe holder, and in the tip of the holder, a gold needle probe is fixed. This gold probe is in good electrical connection to wires inside the metal rod and will be eventually connected to external electronic devices. When we adjust the probe position through the manipulator, the gold tip gently touches the sample surface. Therefore by using a pair of this probe, we can apply an electrical current to a specific region of the sample and perform electrical measurements.

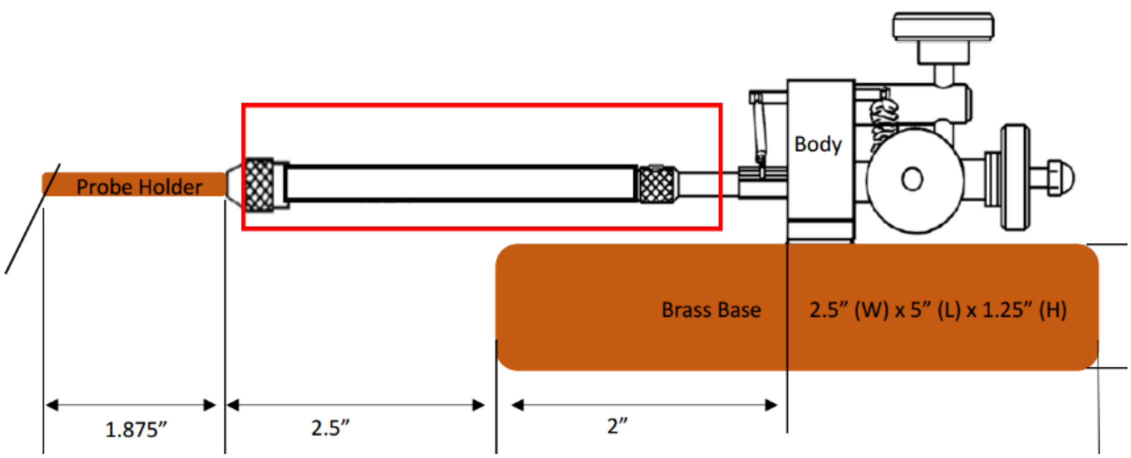

Figure 2. 6 The probe used in touch with the sample for electrical measurement. The needle tip on the left will be pressed onto the sample surface for electrical contact, and it is wire-connected to the terminal of external electrical devices. The three knobs shown on the right are used to adjust the needle's position in three dimensions.

The probes and the sample below it are all observed under a microscope on the probe station table. By careful manipulations, while observing under the microscope, the adjustment screws can smoothly change the probe tip position. When the tip slightly bends due to the touch of the sample surface, solid contact is made without further mechanical damage.

Besides the non-magnetic probes, two pairs of electromagnets are set on the probe station to apply external magnetic fields to the sample during measurements. They can be configured to apply fields in the direction perpendicular or parallel to the sample surface. In actual measurements the amplitude of the field is applied by Kepco power supply controlled by the computer Labview program, in coordination with an electrical measurement device Keithley 2400 connect to the back of the contact probes. In this way, a series of measurements under varying magnetic fields can be performed automatically.

2.3.2 Wire bonding

Besides the probe station, a more reliable way to make an electrical connection with the micrometer-sized thin film samples is to use wire bonding technology. For this purpose, we first need to deposit a layer of gold contact pads on the wafer with Chromium as the adhesive layer, which joins the layer structure to be measured of the sample. The contact pads should have a small size of a few hundred micrometers so that the wire bonder can correctly do operations under a microscope. The wire bonder has a wedge needle as its bonding tip, with a gold or aluminum wire threads. This needle bonds the wire to the sample by ultrasonic vibration, with controllable amplitude and frequency, which melts the wire onto the gold contact pads. The other side of the wire is connected to external electronic devices, in this way a good electrical connection is made with the microscopic sample. It is much more reliable than the tip contact used in the probe station, and can sustain typical nearby vibrations. To make a successful wire bonding, the bonding parameters such as bonding force, bonding time, and the cleanness of contact pads are vital. An assistant tweezer can be used to hold and fix the sample during the bonding vibrations. The tweezer is also needed for subtle adjustments of the bonding wire position, to make sure the wedge needle, the wire, and the sample contact pad aligns well before the start of bonding.

2.3.3 Physical property measurement system

Quantum Design® Physical Property Measurement System (PPMS) is a commercial experimental instrument that measures vast kinds of physical quantities of microscopic samples. The measurements can be performed in our lab at a temperature from 1.5 to 400 Kelvin with magnetic fields up to 9 Tesla. For our research, the PPMS is mostly used for vibrating sample magnetometry (VSM) and Electrical Transport Option (ETO). Here we will introduce how we commonly manipulate the system to conduct experiments.

Fig 2.7 is the outside appearance of PPMS, with multiple electrical lines, pumping lines responsible for conditioning the internal chamber and measuring multiple properties of the loaded sample inside. To load the sample in the first place, on the right figure is the puck component as the sample holder, where thin-film samples are adhered to by a vacuum-applicable glue from Apiezon and electrically connected by wire bonding. A long manipulating rod is the insertion tool that installs such puck with a mounted sample, to the bottom of the sample chamber where an electrical connection will be built with the puck by

12 pins. This installation tool can also grab the puck by a groove in the outer rim firmly, with a switch on its other end. It should be withdrawn only if the sample puck is loaded in the right position, matching the notch of the chamber bottom. An unsteady grip can result in the sample puck falling off halfway, which is extremely hard to extricate if it falls off from the tool into the chamber. The strongly adhesive fishing tool is the last resort to get the remnant out of the PPMS chamber.

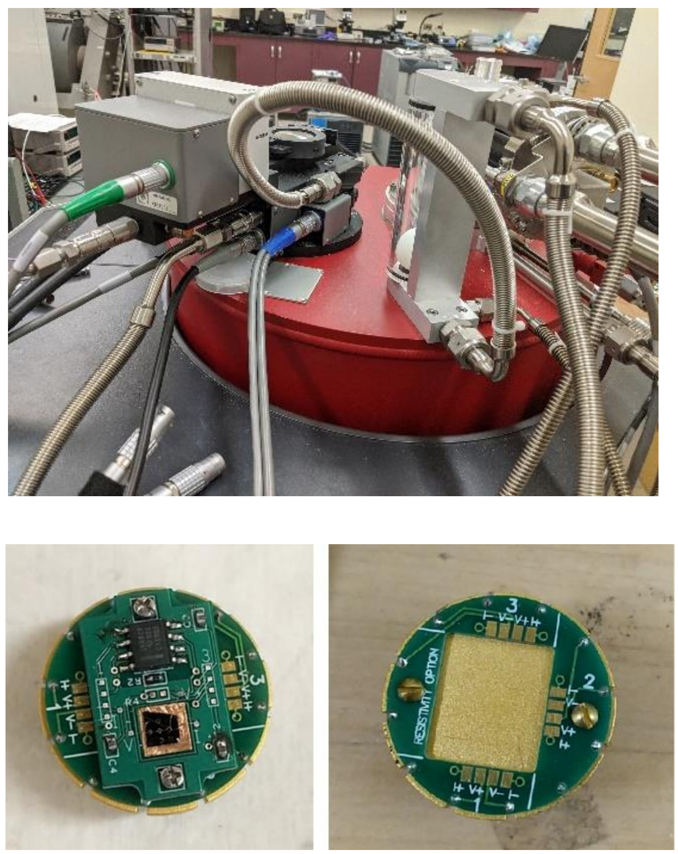

Figure 2. 7 The outside look of PPMS (top) and its puck components (bottom). Such a puck carries necessary electronics to process the signal from the sample mounted on it. It communicates with the PPMS system after being placed into the red chamber.

For PPMS temperature control, the sample chamber is inside an evacuated region with a cooling annulus and aluminum heat shield, which separates the probe from an outer liquid-helium Dewar bath. With good heat insulation, the probe temperature is only influenced by its minimized thermal exchange with the annulus and the heater. The sample chamber after evacuation is usually kept at a pressure at a few torrs of Helium gas, so that the sample is still in weak thermal contact with the walls of the chamber. Liquid Helium can be passed from the bath by a vacuum pump, and flows through the cooling annulus to cool the outside of the sample chamber down to liquid-helium temperature 4.2K. An inside heater is used for increasing temperature, which warms the vapor in the cooling annulus directly, altogether with the sample space. A thermometer is mounted directly beneath the sample puck to monitor its temperature. The helium in the bath is gradually being consumed and a drop in the Helium level can be read, thus the helium supply bottle needs to be replaced roughly every six months.

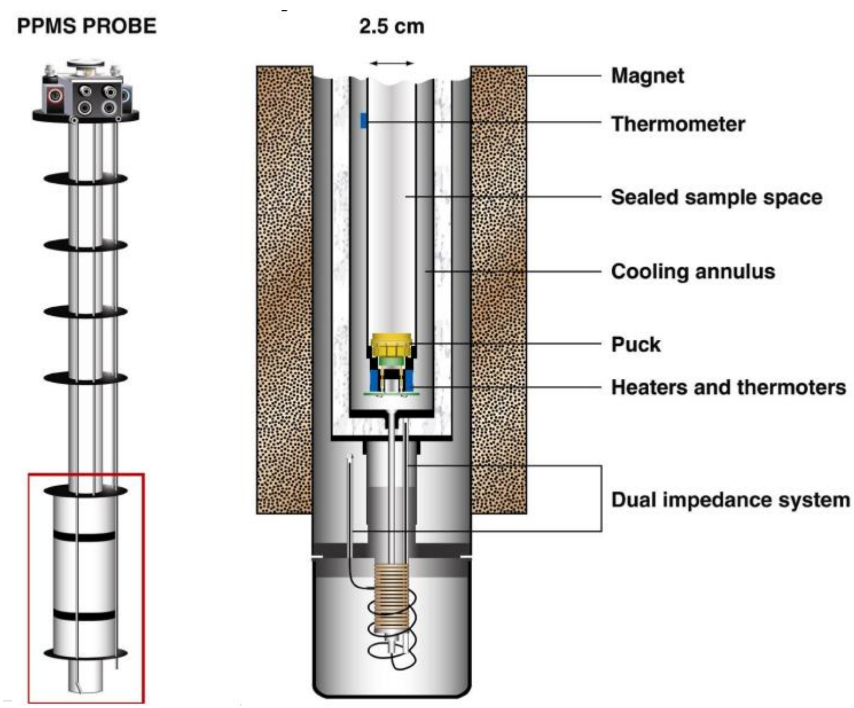

Figure 2. 8 The internal structure of PPMS is designed for insulation and temperature control. As the “Puck” with a sample mounted on is placed into the PPMS, its temperature is controlled by the “Heaters and thermoters” beneath. The “Magnet” on top applies magnetic fields to the sample. The chamber space is well-sealed in vacuum, and liquid Nitrogen in its “Cooling annulus” can cool it down.

For magnetic field control in later experiments, it is applied by superconducting coils inside PPMS to the sample chamber. To generate a maximum magnetic field of 9 T, the magnets need to be covered entirely by liquid helium for cooling down to a superconducting state. The system calibrates the field by measuring the superconducting electromagnets' current, which passes through two standard resistors. The voltage drop on these resistors is proportional to the current and, therefore, to the electromagnets' magnetic field. The remnant field sometimes appears after long-term use, usually of dozens of Oersted. We can set the field to zero from a high field of a few Tesla, in a positive-negative oscillating manner, to eliminate such offset fields if they exist. Besides the oscillating approach, the magnetic field can reach the set point in the linear or non-overshoot approach. The linear approach directly charges electromagnets to the set point, which might induce specific undesirably hysteresis effects. The non-overshoot approach is much slower but the field charging direction is never reversed. After the field reaches the set point it can stay in either driven mode or persistent mode. The driven mode is used if frequent field changes are needed during measurement, which keeps all electronics of the electromagnet active and provides evident more noise from the power supply. In Persistent mode, the power supply is turned off and the current in the superconducting magnet does not dissipate. The magnetic field is applied in the vertical direction of the chamber, while it can have other relative orientations to the sample by the use of a rotatable module or a self-designed printed-circuit-board (PCB). PCBs of proper size can be integrated with the PPMS sample puck, to provide flexible mounting options of samples or first-stage electronic signal amplification.

PPMS is operated by its Ever-cool Multivu software, which performs multiple kinds of measurements and monitors all system status, including pressure, temperature, magnetic field, Helium supply and so on. Customized operation sequences can be programmed in the software, to perform measurements automatically day and night, such as continuous resistance measurements during a temperature scan.

VSM is a module to measure the magnetization of our samples under specified temperature or magnetic fields. The sample is mounted on a sample holder shown in Fig 2.9 and loaded into the magnetic field region inside PPMS. The uniform magnetic field is constant and will first induce specific magnetization in the sample. During the measurement, the sample holder is driven by a motor to mechanically vibrate the sample. A sinusoidal motion of the magnetized sample will result in magnetic flux changes in the pickup coils, which transfers to a voltage that is proportional to the magnetic moment of the sample. In this way, the sample magnetization can be measured at different ambient conditions.

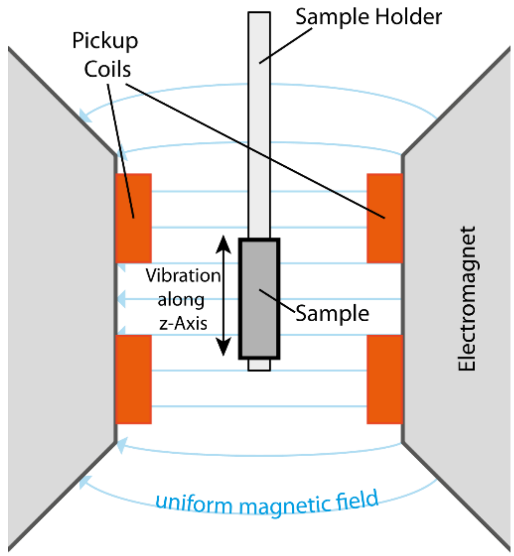

Figure 2. 9 The working principle of VSM measurements. The sample is driven by the sample holder to vibrate, and also magnetized by the electromagnet. The magnetic field signal from the sample at the driving frequency is picked up by two pairs of coils, to estimate the magnetization of the sample.

The sample to be mounted can be thin film, powder or liquid sealed in a capsule. Different sample holders like quartz paddle or a brass-half tube provide different mounting options, either perpendicular to or in the sample plane. Notice that the quantity VSM measures is the total magnetic moment of a loaded sample, to obtain magnetization it needs to be divided by the physical volume of the ferromagnetic layer. The layer thickness is precisely determined by the magnetron sputter process, so more accurate the area value is obtained, the closer magnetization can be calculated. The area can be roughly estimated if the sample has a regular shape. To be more precise, measuring the weight of the sample and dividing it by the density of SiO_2 is viable, since the SiO_2 substrate of the sample takes more than 99% of the mass and volume of a wafer. Another way is to take a photo of the sample under a microscope, and analyze its pixels using software like Photoshop, to get an accurate sample area in any shape.

The electrical transport module provides transfer measurements in multiple ports on the puck. Two-probe or four-probe measurements can be performed by different wire-bonding connections to the pins of a sample puck. PPMS is equipped with a precise current source and voltage amplifiers, which can provide multiple electrical signals like a pulse or stable current to the sample with a precision of 1 nA and a maximum current of 100 mA. Both DC and AC measurements are available, with bandwidth between 0.1 and 200 Hz. The resistance measurement ranges from 10 nΩ to 5 GΩ.

2.3.4 Noise measurement system

Noise as an essential index of sensing performance is measured in the PPMS system combined with our home-made noise measurement system. As shown in Fig 2.10, a typical MTJ sample to be measured is wire-bonded to a PCB, whose electrical circuit is illustrated. This PCB is integrated onto the PPMS sample puck and loaded together into the PPMS sample chamber, as indicated in the dashed line. It is functional under external magnetic fields up to 7 T and temperatures from 150 K to 400 K.

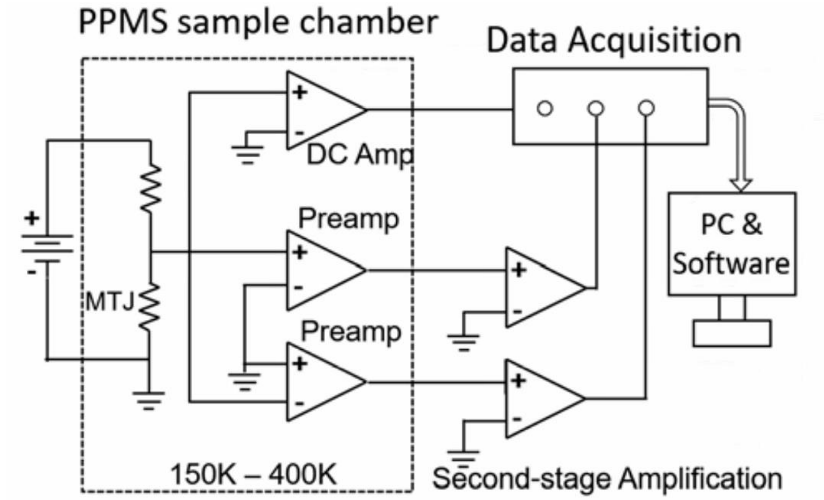

Figure 2. 10 The circuit block diagram of our noise measurement system. An MTJ sensor is connected in series with a resistor, whose voltage signal is amplified by two preamps. These two amplified signals go through cross-correlation to filter out the irrelevant noise from the measurement system. The correlated signal undergoes a second amplification and is read by the data acquisition device.

The PCB is loaded with MTJs mounted on it with a wire bonding connection, so that the signal from the MTJ can be immediately boosted by two first-stage electronic pre-amplifiers. After such immediate amplification, the signal becomes large and robust enough against all possible noise from a temperature gradient, electrical power cord, ground loop, electromagnetic interference, and so on. Such design is indispensable because the noise signal we want to detect is between micro-volts to nano-volts, which can be easily overwhelmed by environmental noise. A two-channel cross-correlation method was used for signals from two pre-amplifiers, eliminating noise coming from sources other than MTJ itself. Afterward, the signal is further amplified by a second-stage amplifier outside the PPMS crater and transmitted to data acquisition devices and computers. The noise measurement system is calibrated by measuring the thermal noise of standard metal film resistors, to exhibit a background noise of $3nV/\sqrt{Hz}$ which is negligible in most cases. The data acquisition devices used in this system have a bandwidth up to 10 kHz. The Labview program controls the noise performance on a computer, which will perform multiple times of averaging and Fourier transform to output the noise power spectrum. In addition, on this PCB few current leads is embedded to apply a modulating field ($\delta H = 0.25$ Oe) at a few Hz near the sample. Such small AC fields are used to measure the sample sensitivity, which usually turns out much smaller than the value estimated from major hysteresis loops. Further detail is introduced in our works [34,35], where many noise spectrums are characterized by such a system.

2.3.5 Atomic and magnetic force microscopy

The visualization of the shape, surface roughness, crystal grains, or magnetization of micro-sized samples can be achieved by atomic or magnetic force microscopy[36]. During its measurement, the AFM tip scanning over the sample surface with a sharp tip in the size of tens of nanometer, in either a mode of touching or tapping.

As shown, these AFM devices have a scanning tip as shown in the left figure of Figure 2.13, whose vertical position changes due to the surface morphology of the sample will be significantly amplified and read using an ordinary laser reflection method. The tip is usually connected to a cantilever in an oscillation motion of 75 kHz driven by a piezoelectric element, and this motion will be influenced by the atomic scale interaction between the sample and the tip. Therefore, we can measure the interaction from the sample beneath, which is due to microscopic atomic or magnetic force by monitoring the tip motion. Since the force is a function of the separation distance or the sample magnetization, such measurements reflect the sample surface roughness or magnetic domains.

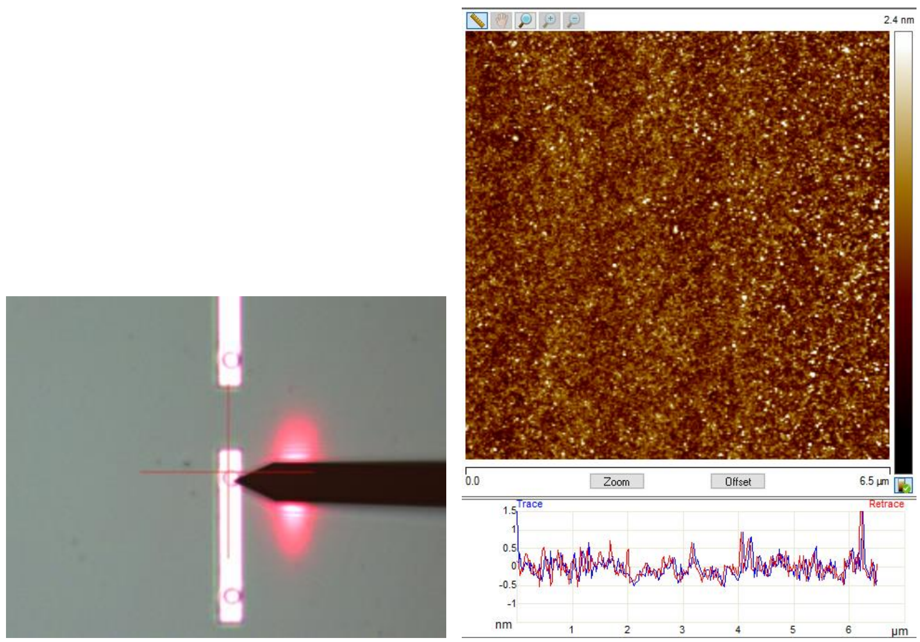

Figure 2. 11 The microscopic scanning image (left) and its immediate output result (right). The shadow shows the position of the scanning tip, sweeping across the circle for an MTJ below it. The AFM graph shows its planar height distribution, and the curve below is the roughness measured in one single scan.

A standard scanning setting uses a lift scan height between 20nm and 100nm, where a smaller height means a smaller separation between the tip and the sample surface. Putting the tip closer to the sample surely boosts the signal, but could lead to tip damage. The scanning speed is usually a few micrometers per second. The right figure of Figure 2.12 reflects the surface condition of our MTJ, which has a small circular shape observable at the left tip position. It shows a roughness between ±1 nm indicating a good sample quality.

2.3.6 X-ray crystallography

X-ray crystallography consists of X-ray diffraction (XRD) and X-ray reflectometry (XRR). These two structural characterization techniques provide lots of information on crystal textures, film thickness, and grain size, usually combined with morphology characterization like AFM[37]. XRD is used to determine the crystalline structure and phase of samples, where the crystalline structure of the sample diffracts the X-ray beam and the interference pattern is observed. XRR is used to determine thin-film layer stacks' thickness and roughness, applicable to both crystalline and amorphous materials. In this case, the beam is reflected by the flat surface or interface of a sample, and the intensity of the reflected beam is measured at different reflection angles. The detector should be set in low reflective angle ranges for XRR, and the measurable thickness is below 100nm. The sample roughness can be deduced from the deviation of reflected beams by the law of Fresnel reflectivity. These working principles are illustrated in Fig 2.14 below.

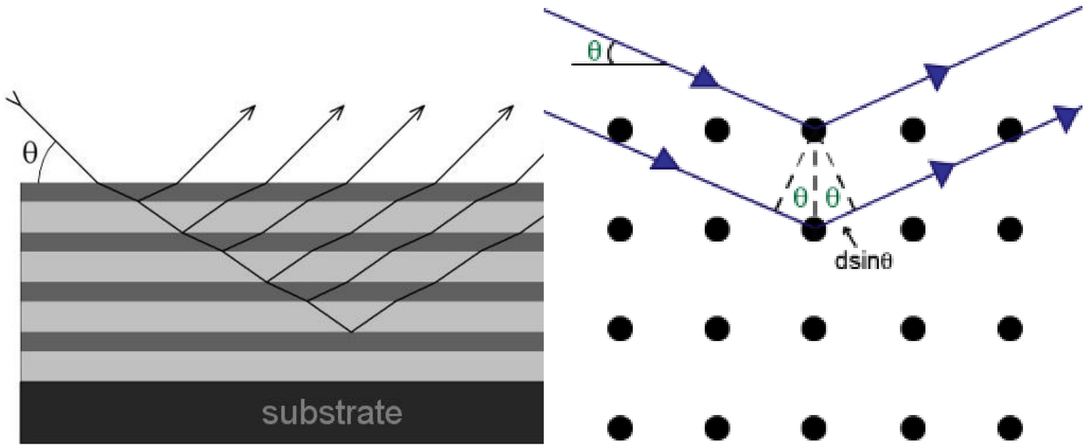

Figure 2. 12 The principle of XRR and XRD, where the incident X-ray is either reflected by the interface between thin-film layers (left) or diffracted by multiple atoms of a crystal lattice (right).

Assume θ to be the incident angle which equals the angle of reflection, λ the X-ray wavelength, and d the thin-film thickness. By XRR theory they are related by

$$d \approx \lambda(\theta_{m+1} - \theta_m)/2$$

where θ_{m+1}, θ_m are two angles corresponding to two successive peaks of X-ray intensity (denoted by "Counts" for our detector).[38] For XRD measurements, the data of diffraction peaks can be compared to standard diffraction cards of all known elements, to determine the composition of measured samples. Below is a typical result of ours:

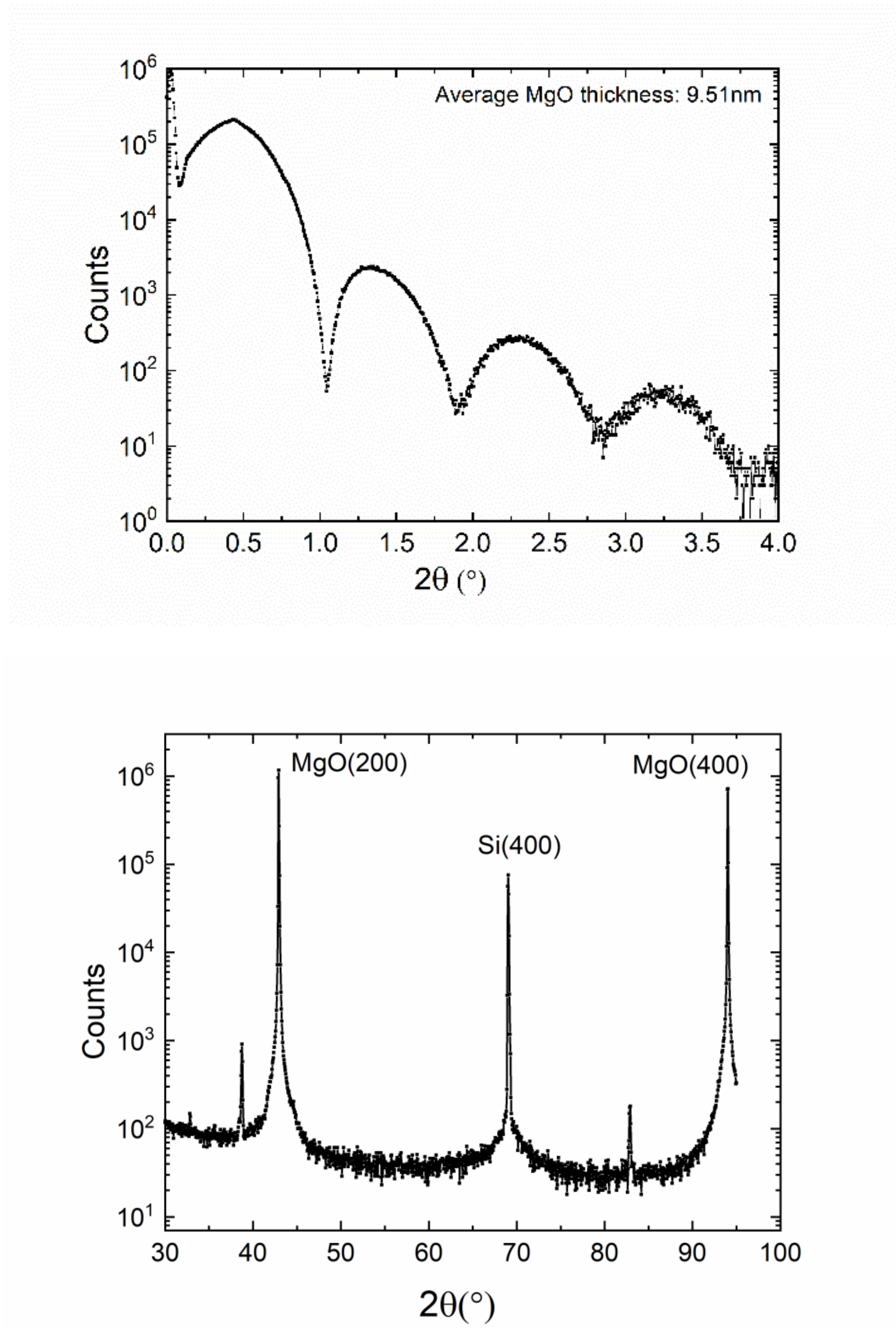

Figure 2. 13 Our typical XRR (top) and XRD (bottom) counts from the X-ray receiver, where θ is the incident angle in Fig 2.12. The peak positions in these results indicate the layer thickness or the lattice structure of a certain element.

Two results shown in Fig 2.13 above are shown as examples. For the XRR result, the wavelength of the Cu beam is λ =1.54A, which is obtained by performing Gaussian fitting on each peak to retrieve the peak position accurately. The peak positions are then averaged and used to calculate the MgO layer thickness. It is noteworthy that the measurable thickness should be no more than 30 nm. The 9.51nm XRR result confirms the expected thickness of 10 nm in an MgO sputtering process. In the XRD result, we observed several characteristic peaks determined by comparisons to standard XRD cards of MgO and silicon elements. The composition of each peak is then revealed and labeled according to the result.

Chapter 3 Theoretical Background

3.1 Introduction

This chapter gives the theoretical backgrounds that support the experimental works in later contents. We will first describe the MgO-based magnetic tunnel junction (MTJ), fabricated by equipment in chapter 2. MTJ is a multilayer stack where each layer has functions such as buffering, magnetic coupling, interlayer crystallization, and so on. The mechanisms of electron tunneling in such a multilayer structure will be discussed. The physics of noise in general signals is introduced, paving the way for later discussions about the MTJ sensing performance. The recipe iterations of our MTJ recipes will be presented, with new insertions of auxiliary layers. The physics mechanisms of flux concentrators, superparamagnetism, and vortex magnetization, and their contributions to the overall MTJ properties will be discussed fundamentally. The idea of applying interfacial perpendicular magnetic anisotropy (PMA) in our MTJ free layer will also be discussed.

3.2 Magnetron sputtering

3.2.1 Sputtering chamber

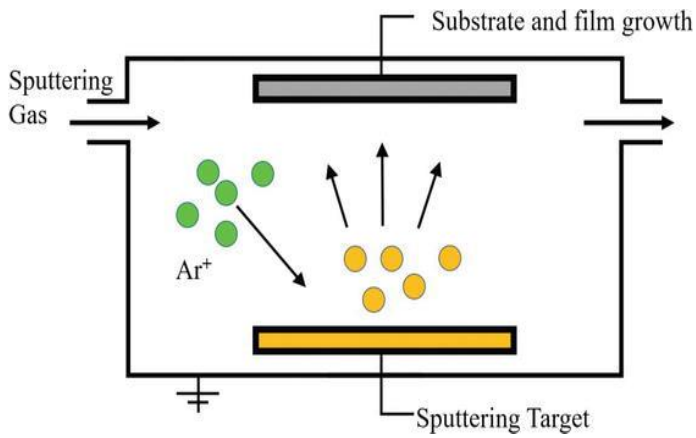

Figure 3. 1 Schematic working principle of magnetron sputtering. After the sputtering gas is passed into the chamber, it is ionized to bombard the target; the target particles are then scattered into the substrate on top.

Fig 3.1 above demonstrated the physical process of our magnetron sputtering. During the deposition, Argon gas is passed into the chamber and ionized by a strong electrical field of a few hundred volts. The Argon ions form a purple plasma and get accelerated by the electric field to bombard the target. To enhance the sputtering efficiency, a magnetic field is present to confine the trajectory of ions close to the target by Lorentzian force. To sputter insulating materials, radiofrequency power needs to be used, to prevent electrical accumulation on the surface of the target, which cannot be conducted anywhere. As a result of the Argon ion bombardment, the particles of the target sputter towards every outward direction, and a portion of it accumulates on the substrate surface, forming a thin film structure.

3.2.2 Thin-film morphology

For materials that we hope to obtain a polycrystalline structure by sputtering, such as the MgO layer in MTJs, we usually use lower Argon gas pressure around 0.8 mtorr during its sputtering. For materials where an amorphous film is expected, we will use higher Argon pressure around 1.4 mtorr. The physical explanation is that for constant sputtering power, the less the Argon ion numbers, the higher the average energy for each ion. Correspondingly, the target particles bombarded by the ion also have larger kinetic energy, to be scattered towards the substrate. The target particles with high energy are more capable of forming a crystalline structure on the substrate, where each particle finds its energetically favorable position. On the other hand, if the particles are easily trapped randomly everywhere on the substrate surface without sufficient kinetic energy, an amorphous state is formed.

Besides the sputtering pressure, other options like in-situ post-annealing during sputtering can meanwhile be adopted to form a desired atomic structure, where the substrate is subjected to heating or cooling during sputtering[39]. With various methods, the morphology of each layer in a thin-film stack can be controllable.

3.3 Tunneling magnetoresistance

3.3.1 Julliere’s model of magnetic quantum tunneling

With a specific sputtering recipe, we can make MTJs with tunneling magnetoresistance ratio (TMR) up to 100% in our sputtering chamber, as we are going to introduce. The tunneling process of electrons of majority spin or minority spin is considered independent events, as shown in Fig 3.2. Electrons of different spins have different densities of states (DOS) at the Fermi energy level, and they will only tunnel into the electron band of the same spin on the other side of the tunneling barrier. The tunneling resistance is thus related to the DOS of each spin on both electrodes, where the magneto-resistance ratio (MR) is defined and given by:

$$\mathrm{MR} = \frac{R_{AP}-R_P}{R_P} = \frac{2P_1P_2}{1-P_1P_2}$$

R_{AP} and R_P denote the resistance of antiparallel and parallel magnetization orientation between two electrodes respectively; P_1 and P_2 are the spin polarizations of two ferromagnetic electrodes, which can be related to the DOS of their electron bands.

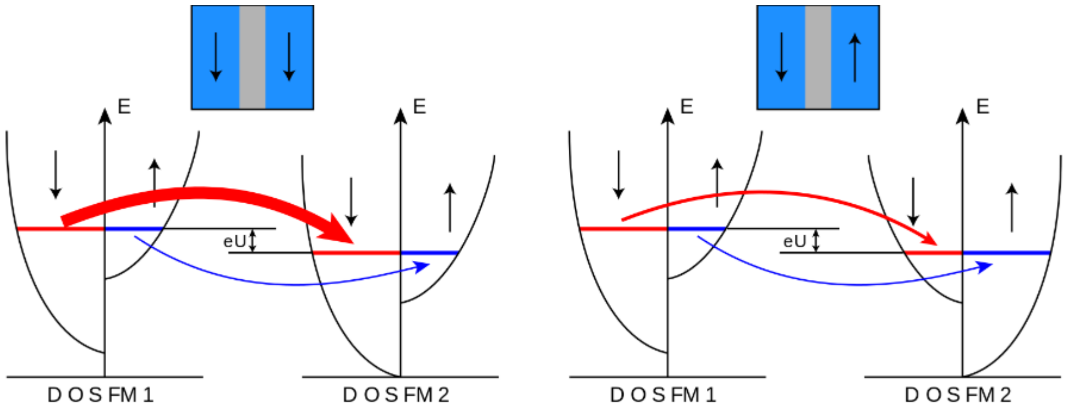

Figure 3. 2 Julliere's model for tunnel magnetoresistance. In the parallel configuration on the left, electrons of a certain spin tunnel into the same band on the other side of the barrier; in the antiparallel configuration on the right, they tunnel into the band of opposite spin.

Slonczewski later explained the tunneling process in 1988, by a model of two ferromagnetic electrodes separated by a non-magnetic barrier, with the free-electron approximation of the spin-polarized conduction electrons. The tunneling electron transmissivity can generally be expressed by[40]:

$$j = \frac{e(2s+1)}{h} \int dE[f(E) - f(E+eV)] \int \frac{d^2 k_{//}}{(2\pi)^2} D(E, \boldsymbol{k}_{//})$$

where the integration is overall energy of a specific electron band, f is the Fermi-Dirac distribution and $\boldsymbol{k}_{//}$ the wave vector component of Bloch electrons parallel to the plane of the junction. The transmissivity $D(E, \boldsymbol{k}_{//})$ is required to be calculated as a function of the electron states. Consider an incident plane wave of an electron of up or down spin, exponential decay in the barrier, and the matching condition of wave functions, the transmissivity of such electrons can be solved[41]. Afterward, by integrating the transmissivity for all occupied electron states in a typical free electron band, the total tunneling current can be obtained. The electron conductance obtained in this way has shown a cosine dependence on the relative angle θ of the magnetizations in two electrodes separated by the tunnel barrier:

$$G = G_0(1 + Pcos\theta)$$

G_0 is the mean surface conductance, and P is the effective spin polarization.

Unlike the Julliere model, TMR here has shown a direct dependence on the polarization as a function of both electrodes' effective wave vectors. Such a simplified model has been supported by experiments and sheds light on the tunneling phenomena. However the assumption of a square potential corresponding to a thick tunnel barrier is not realistic, and a more accurate evaluation of the transmissivity needs to be found using the Wentzel-Kramers-Brillouin (WKB) method. In addition, optimization of the MTJ is still difficult with this model as many relevant parameters are lost. Many features of MTJ like the temperature and bias voltage dependences, can hardly be accounted for since the transmission across the tunnel barrier needs to be treated more carefully. Later on, Zhang rigorously solved the quasi-one-dimensional free electron model using a transfer matrix method, where a linear potential for the barrier and the WKB approximation is applied.[42,43] Although several matrix elements cannot be analytically calculated, numerical methods using this transfer matrix results and a parabolic band of free electrons have correctly described many MTJ features in experiments. Nevertheless, the actual bands of ferromagnetic electrodes are not considered, which are far more complicated.

3.3.2 MgO tunneling barrier for symmetry filtering

In early times, the Aluminum oxide is used as the insulating tunnel barrier, which is amorphous with no crystalline symmetry. In this case, the Bloch states of various symmetries couple with all evanescent states inside the barrier, and such incoherent tunneling process usually exhibits low MR values. On the other hand, in MgO-based MTJs the crystalline MgO (001) barrier contains few kinds of evanescent states, among which only the state with Δ_1 symmetry have a slow decay rate. Since the symmetries of wave functions are conserved during tunneling, and the Bloch states in both electrodes couple with the evanescent states within the barrier of the same symmetry. Such tunneling is denoted as coherent tunneling, where the momentum and coherency of electron states are preserved. As a result, only the electrons in the band with Δ_1 symmetry can tunnel through with the most extended decay length, which is often called a symmetry filter effect. For an anti-parallel magnetization configuration, the Δ_1 electrons after tunneling have to continue decaying since there are no corresponding bands for the opposite spins. Thus the conductance for anti-parallel configuration becomes much lower, dependent on the polarization of electrons. Since Δ_1 bands of material like Iron is fully polarized, a highly spin-polarized tunneling current and a high MR ratio are expected.[44]

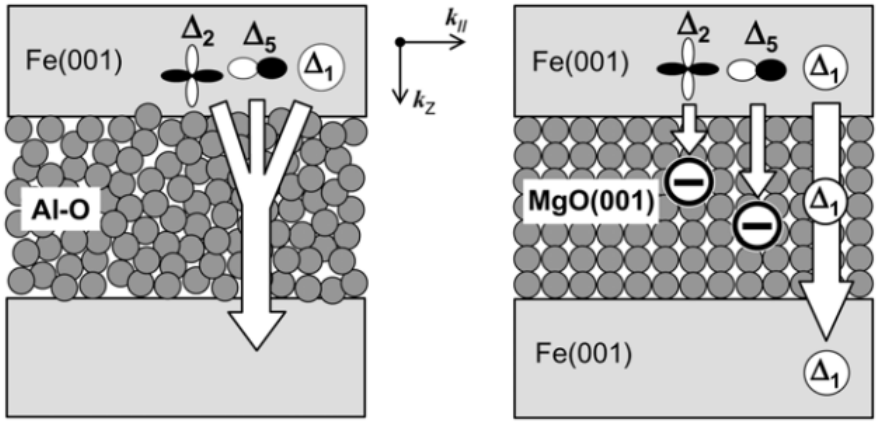

Figure 3. 3 The mechanism of incoherent (Left) and coherent (Right) tunneling, from reference [4]. For the AlO barrier, electrons in the bands of several kinds of symmetry tunnel through the barrier indiscriminately; for the MgO barrier, only the spin-polarized electrons in Δ1 band tunnel through with high probability.

Figure 3.3 schematically described these two processes. In a nutshell, the symmetry of Bloch electron states near the Fermi energy and the symmetry of the evanescent states in the insulator needs to be matched for a slow decaying rate, which is found by the Korringa-Kohn-Rostoka (LKKR) calculation[43]. A crystalline MgO layer serves as a symmetry filter to provide highly spin-polarized Δ1 electrons, which results in a high TMR ratio. Also, the density functional theory (DFT) is used to calculate the materials' electronic band structure and the Bloch waves were calculated using the layer LKKR formalism based on the DFT results, giving more accurate transmission coefficients.

However, such theoretical prediction of high MR ratio requires a fully epitaxial MTJ with a perfect crystalline MgO tunnel barrier, and also an ideal interface structure without pin-holes and inter-diffusion or lattice mismatch which leads to ohmic contact. These requirements are relatively strong, as oxidation of even a monolayer at the interface significantly suppresses the TMR effect. Water molecules can also severely jeopardize the barrier material MgO. Therefore, in the experiment a typical MR value is around 100% to 600%, much lower than theoretical predictions.

3.4 Magnetic tunnel junction (MTJ) multilayers

3.4.1 Atomic layer engineering and functionality

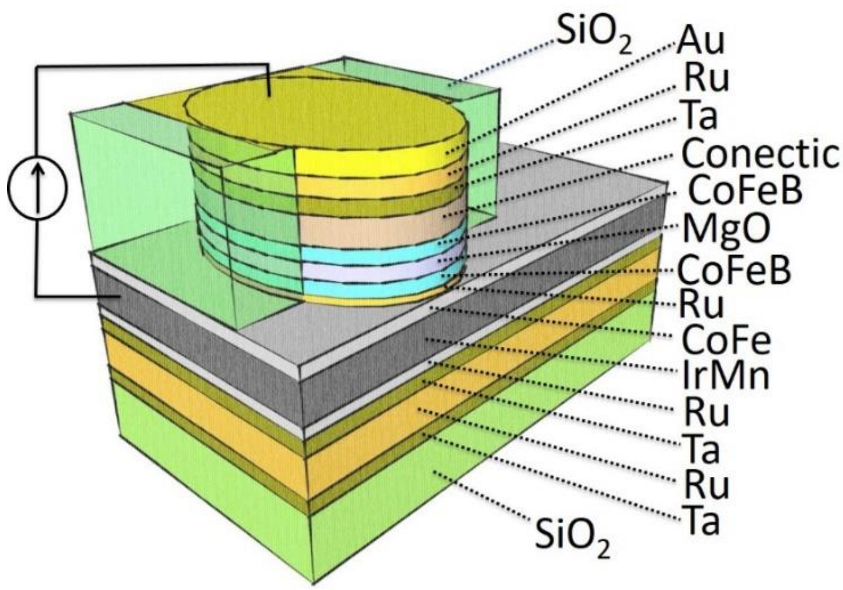

Figure 3. 4 Our conventional MTJ layer structure diagram. The bottom electrode is grown on the SiO_2 substrate, and on top of that is the oval-shaped MTJ multilayer capped by gold. An additional SiO_2 layer is protecting the MTJ from all around.

In Figure 3.4 is our conventional MTJ containing the following layer stacks Si/SiO2/Ta(5)/Ru(30)/Ta(5)/Ru(2)/IrMn(18)/Co50Fe50(3)/Ru(0.85)/Co40Fe40B20(3)/MgO(2.9)/Co40Fe40B20(2.5)/Ta(5)/Ru(10), where the numbers in parentheses represent the thickness of each layer in nanometer. Another gold layer above 100nm will be sputtered on top later as an extension of electrical contact.

Starting from the bottom, the SiO2 substrate surface is first made by the thermal annealing device, which is around 2μm thick on the substrate surface. During the magnetron sputtering process, an iteration of Tantalum and Ruthenium layers Ta(5)/Ru(30)/Ta(5)/Ru(2) are deposited as the bottom conducting electrode of MTJs. They also serve as a flat seed layer that enables subsequent materials of other lattice constants to be successfully deposited onto the wafer without peeling off. The top Ruthenium can also take in the diffusive Manganese elements from the IrMn layer above.

The next composite layers to deposit are IrMn(18), which applied the pinning field to the reference layer. Since the lattice constant of CoFe is between IrMn and Ta, a thin layer of CoFe can be inserted below IrMn as a seed layer to reduce the lattice mismatch and provide IrMn a good spin texture. The anti-ferromagnetic (AFM) IrMn with (111) surface plane functions to provide a strong exchange bias to pin the magnetization of an adjacent ferromagnetic (FM) layer, while itself being immune to external magnetic fields. Such exchange bias needs to be established during the field-assisted thermal annealing. After IrMn is heated above its Ne´el temperature near 280K to become paramagnetic, a magnetic order along the external magnetic fields will be induced during the field cooling. The interfacial exchange coupling aligns the magnetization of an adjacent FM layer with its nearest AFM spins, and as a consequence the FM layer is effectively pinned by a biasing magnetic field of three hundred oesterd.

The composite layers $Co_{50}Fe_{50}$(3)/Ru(0.85)/$Co_{40}Fe_{40}B_{20}$(3) serve as the reference layer of MTJ. It is called the synthetic anti-ferromagnetic (SAF) layer, composed of two magnetic layers coupled by Ruderman–Kittel–Kasuya–Yosida (RKKY) interaction through a non-magnetic spacer in an anti-ferromagnetic manner. The RKKY coupling strength as a function of the thickness of the spacer layer is oscillatory, switching from positive to negative with a period of few angstroms[45]. Thus the Ru thickness is critical, and a 0.85 nm thickness gives a large coupling strength for our samples. Compared to a single ferromagnetic layer, the SAF layer is reported to apply a stronger pinning field to the reference layer. It also has higher thermal stability and less small stray fields. The stability comes from the opposite direction of two ferromagnetic layers, which can be effectively seen as an AFM layer with no net magnetization, insusceptible to external magnetic fields. Such a reference layer pinned by the AFM layer below serves as one side of the electron tunneling process.

The MgO insulating layer serves as the barrier potential for electron tunneling. This layer is sputtered by radio-frequency power with 8 minutes long pre-sputtering time to clean the target. Besides this, the chamber must be baked and evacuated well beforehand to eliminate all impurities and water vapor, as hydroxylation is devastating to MgO. To deposit a high-quality MgO layer in a clean, smooth, and free of pinholes condition is the most vital part for MTJs. The sputtering pressure of Argon gas will be decreased to make the MgO layer more poly-crystallized as explained in section 3.2. MgO needs to be highly oriented with (001) lattice plane, which will further serve as a template to crystallize adjacent amorphous CoFeB layers in the post-deposition thermal annealing process. This interfacial crystallization leads to a spin filtering effect which is the origin for high tunneling magnetoresistance (TMR) ratios of MTJ. Boron elements in adjacent CoFeB layers serve to prevent CoFe from forming its own poly-crystalline structure during sputtering. In the post thermal annealing process, these Boron will diffuse away to other layers, and then the remnant CoFe component follows MgO to form bcc (001) crystalline texture (perpendicular to the layer plane). The formation of interfacial perpendicular magnetic anisotropy in perpendicular MTJ (pMTJ) fabrication also requires such an important crystalline structure, enabling the hybridizations of iron and oxygen electron orbitals through a spin-orbit coupling. The thickness of this insulating layer determines the resistance of MTJ, which increases exponentially with thickness due to the physics of tunneling.

The next is the free layer composed of $Co_{40}Fe_{40}B_{20}$ (2.5). As explained in section 3.3, the MTJ magnetoresistance is dependent on how the spins in its free layer respond to external magnetic fields. Thus by modifying the magnetic phase, domain structure of this layer, we will obtain MTJs with different magnetic properties. The geometrical parameters, annealing condition, and magnetic anisotropies are several factors that we can control to modify the magnetization state in this layer. The internal magnetic fields at the free layer will be observed as an undesired bias field in the MTJ hysteresis loop, which could come from dipole interaction, exchange coupling or Neel coupling from adjacent layers.

Finally capping layers of Ta(5)/Ru(10) is deposited to seal and protect the MTJ from ambient oxidation and hydroxylation. It is noteworthy that if the light reflective capping layers are made too thick, the free can be too deeply embedded to be measured by any MFM or magneto-optic Kerr measurements.

3.4.2 Hysteresis and offset field

Our MTJ with CoFeB as the free layer typically shows hysteretic coercivity of tens of oersted, which is intrinsic to the CoFeB material and is not ideal especially for low field measurements. Inserting Ta(0.3)/Co-Netic(40) layers between the free layer and the top capping layer during sputtering can reduce the overall coercivity observed in the MTJ hysteresis loop down to a few oersted, where Co-Netic is the commercial name of a soft magnetic alloy $Ni_{77}Fe_{14}Cu_{5}Mo_{4}$. In this case, the free layer effectively becomes a composite of $Co_{40}Fe_{40}B_{20}$(2.5)/Ta(0.3)/Co-Netic(40), where original $Co_{40}Fe_{40}B_{20}$ and Co-Nectic are magnetically coupled. The coherent tunneling conductance is still determined by CoFeB magnetization, but now the spin orientation is linked to the magnetization of the Co-netic layer above it. In this way, the total free layer's magnetic property is improved, thanks to the small hysteresis and large saturation field of Co-Netic alloy.

Despite the hysteresis, MTJ also suffers from offset fields that shift the center of the hysteresis loop and saturates the free layer at zero external fields. The coercivity is due to the irreversible evolution of magnetic domains when responding to external fields. The offset field comprises of the dipolar stray fields and Néel fields from nearby magnetic layers, which disables it to sense low magnetic fields near zero field position.

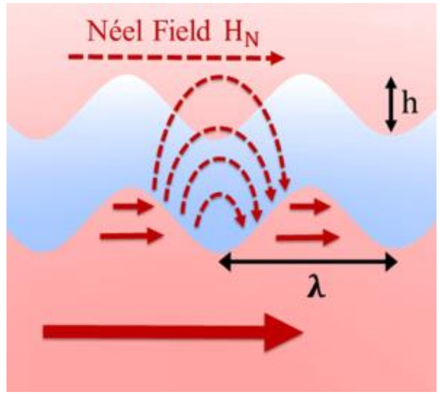

Figure 3. 5 The Néel fields due to surface roughness, from Reference [46]. Due to the surface roughness of a magnetic layer, the surface bumps with a wavelength λ and height h exert a stray field as shown.

In our MTJ the offset field is mainly contributed by the Néel fields, which depends on the correlated roughness of adjacent ferromagnetic layers, as shown in Figure 3.5. The magnitude of the offset field from this sinusoidal roughness is theoretically given by:[46]

$$H_N = \frac{\pi^2}{2}\frac{h^2}{\lambda t_F} M e^{-2\sqrt{2}\pi t_S/\lambda} \qquad (3.3)$$

t_F is the free layer thickness (top layer), t_S the thickness of the non-magnetic spacer (middle blue layer), M the saturation magnetization (bottom layer), and λ, h the geometrical parameters defined in the figure. Raising the sample quality to have less roughness or increasing the non-magnetic spacing can eliminate this effect. The use of a synthetic anti-ferromagnetic (SAF) free layer is another approach in literature to reduce it.[47] The decaying rates of the stray fields and Néel fields are different, and they are opposite in direction. Therefore by changing the free layer thickness we can make them counteract each other to null the offset field. Empirically, increasing the free layer thickness to 5nm can bring the offset field down to zero, although a thickness between 1 to 2 nm is more often used giving an offset between 5 to 10 oersted. This method is very sample-dependent since the surface roughness is hard to predict, resulting in different Néel fields.

3.4.3 Interlayer diffusion

It is reported in the literature that the Manganese diffusion in the MTJ annealing process could lead to the disappearance of the exchange bias, which reduces the pinning force for the reference layer and TMR value[48]. To prevent Manganese diffusion, we adopted Ruthenium as the adjacent diffusion absorber near the IrMn AFM pinning layer. As mentioned in the MTJ theoretical background, the Boron element in CoFeB diffuses away during the annealing process for this layer to follow the crystallization of the MgO layer. Heat treatment like thermal annealing can easily give rise to element migrations across layer interfaces such as boron and oxygen, but the diffusion could harm the films' magnetic properties. In literature, it is reported that Boron in the free layer CoFeB could diffuse in both directions, upwards to the capping layer or downwards into the MgO layer.[49] This diffusion could form Boron oxide at the interface between MgO and CoFeB to degrade the TMR ratio, go further into the oxygen vacancies in MgO to lower the barrier height, or even create pinholes to short-circuit the tunnel junction. This interfacial effect is severe when the thickness of the MgO layer is reduced for lower resistance, in our case around 1.5 nm. To prevent such degradation of MTJ, we managed to absorb the diffused Boron by using a capping layer of higher Boron affinity like Ta, and by inserting a Fe–Co layer between MgO and CoFeB for the same purpose.[50] The insertion of a CoFe intermediate layer cannot be too thick to block the crystalline structure continuity between MgO and CoFeB, while still thick enough to prevent Boron diffusion. On the top free layer, a very thin CoFeB layer of 0.4 nm needs to be inserted before the deposition of CoFe, to prevent CoFe from forming its crystalline structure. The most effective recipe modification we have found is to replace the initial core sandwich structure of MTJ by $Co_{40}Fe_{40}B_{20}/Co_{50}Fe_{50}(0.5)/MgO/Co_{40}Fe_{40}B_{20}(0.4)/Co_{50}Fe_{50}(0.5)/Co_{40}Fe_{40}B_{20}$, which helps to enhance the MR value of MTJs from 70% percent to above 100%.

3.4.4 Resistance-area parameter

MTJ has both inherent tunneling magneto-resistance (TMR) and tunneling magneto-capacitance (TMC) effect, and only the resistance part is utilized in MTJ to sense magnetic fields. The equivalent of MTJ in the circuit diagram is effectively seen as a capacitance connected in parallel with a resistance. The resistance-area (RA) product is a constant for MTJs with the same MgO layer thickness, regardless of other parameters like size or shape. For MTJ to be used in applications like microwave generation or microwave reflection imaging, the MgO layer thickness needs to be kept thin to give a smaller RA constant. Otherwise, because of its high resistance, the high-frequency current flows through MTJ in the parallel capacitance channel and ends up with no TMR effect. With the Boron diffusion prevented by the method in section 3.4.3, we can modify the RA product by MgO thickness, and the frequency response of MTJ below:

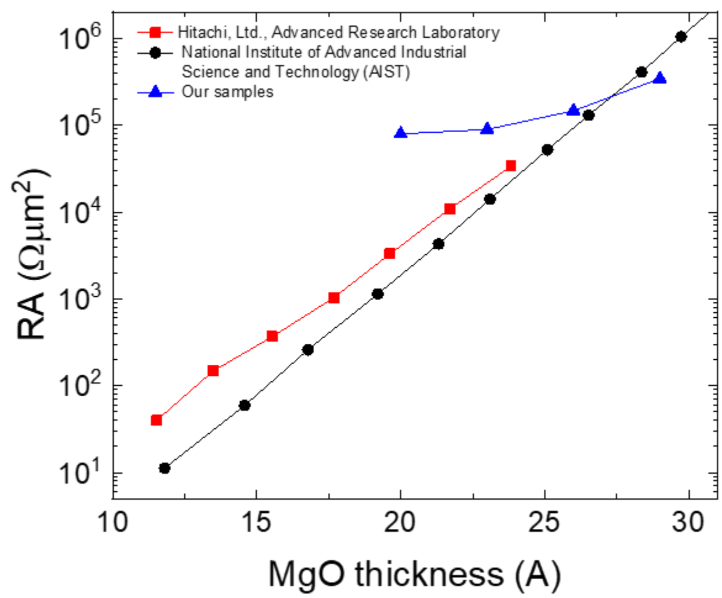

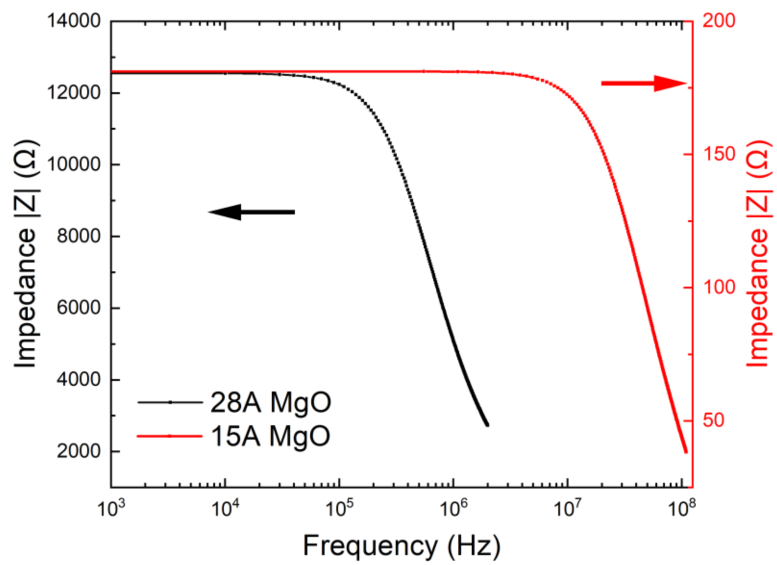

Figure 3. 6 The MTJ RA constant as a function of MgO barrier thickness is shown on the top figure; those data points cited are from reference [51]. At the bottom is the frequency-dependent impedance $|Z|$ measured from our MTJs of two different MgO thickness.

In the top figure of Fig 3.6, we can see our RA constant follows the result from other groups reported in the literature. However, at low MgO thickness, extra resistance is observed in conflict with literature results. This is probably because of the appearance of parasitic resistance introduced by the contact lead, when the total resistance is comparably small. In the bottom figure, assuming a resistance R and capacitance C, the impedance of MTJ is plotted, which can be expressed as magnitude $|Z| = [1/R^2 + (2\pi f C)^2]^{-1/2}$, phase $\theta = \arg(Z)$. It is considered as an effective electric element, where the magnetoresistance and capacitance of MTJ are connected in parallel. From the fitting we have for the case of 28 A MgO, $R = 12528.2\,\Omega,\ C = 2.85 \times 10^{-11}\,F$; for 15 A MgO, $R = 181.5\,\Omega,\ C = 3.05 \times 10^{-11}\,F$. The capacitance of MTJ can be considered to come from a plane-parallel capacitor, where the free and reference CoFeB layers are the plates, and the MgO barrier between them are the dielectric material. However, these effective models are not exactly valid, since MTJ is a quantum device. The charge carrier of it could be the exciton, and the tunneling process in a nanometer scale governed by quantum mechanics could have unexpected frequency dependence. MTJs with thinner MgO layer (Red curve) has shown increased cutoff frequency as expected, because of the smaller RC constant. This MTJ intended for a high-frequency application can thus work at 20MHz.

3.5 Noise physics and analysis

3.5.1 Manifestation of the noise signal

In all kinds of sensing devices such as MTJ mentioned above, the detection limit is set by its intrinsic noise. The noise is generally demonstrated by its power spectrum, as we will introduce in the first place. Any noise signal can be represented by a random variable $x(t)$ changing with time t, which follows a particular probability distribution $p(x)$. That is to say that $x(t)$ can have arbitrary values at any time, while its time-averaged values are determined by the probability distribution $p(x)$. For any physical quantity $f(x)$ dependent on $x(t)$, its expectation value can be expressed by:

$$< f(x) >= \lim_{T\to\infty} \int_{-T}^{T} f\big(x(t)\big)dt = \int f(x)p(x)dx$$

The auto-correlation function is defined as:

$$< x(t)x(t+\tau) >= \lim_{T\to\infty} \frac{1}{T}\int_{-T}^{T} x(t)x(t+\tau)dt$$

Assume the Fourier transform of $x(t)$ is $X(f) = \lim_{T\to\infty} \int_{-\frac{T}{2}}^{\frac{T}{2}} \exp(i2\pi ft)\, x(t)\, dt,$ and the power

spectrum density is $S(f) =< X(f)X^{*}(f) >$. By Wiener-Khinchin Theorem, we can deduce that $S(f)$ equals to the Fourier transform of $< x(t)x(t-\tau) >$ [52]. In a general characterization of the lowest detectable signal of a device at a certain frequency, the value read from the noise spectrum $S(f)$ represents the standard deviation of the random signal fluctuations, which prevents the device to give a more satisfactory measurement resolution. Considering common data acquisition devices with an equivalent noise bandwidth df dependent on their band pass filters, the quantity $S(f)df$ then gives the lowest detectable signal of a device. Signals smaller than that are just immersed in the fluctuation of noise.

3.5.2 Lorentzian and 1/f noise spectrum

Consider an illustrative model of the trapping of charged particles with a broad distribution of time constants. This microscopic random trapping and release process is observed as a flipping process between two states of different voltages $x = \pm 1$ as shown in Fig 3.7:

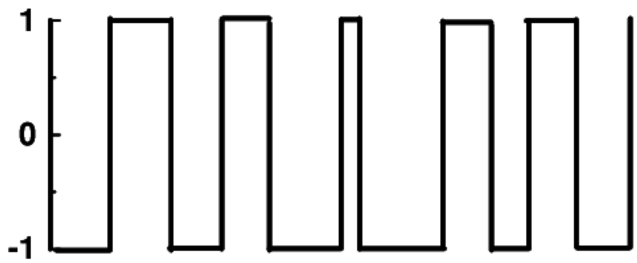

Figure 3. 7 A simplified time-domain flipping signals of random telegraph noise; the x-axis is time and the y-axis is the signal assuming only two values.

Assume the probability $p(m, T)$ of observing m flipping events in the time T follows a Poissonian distribution:

$$p(m, T) = \frac{(vT)^m}{m!} \exp(-vT)$$

The auto-correlation function is then given by:

$$< x(t)x(t+\tau) >= \exp(-2v\tau)$$

We can then deduce $S(f)$ by the Fourier transform from it using Wiener-Khinchin Theorem:

$$S(f) = \frac{4\tau_Z}{(1 + \omega^2\tau_Z^2)}$$

$\tau_Z = 1/2v$ is the trapping time constant. This is just a typical power spectrum of Lorentzian noise observable in many devices like spin valves, where unknown defects and impurities in the material serve as electrical traps to provide such noise.

In a physical device, the defects or impurities mentioned above are numerous and so do the corresponding electrical traps, each of which could have a different trapping time constant. In ferromagnetic materials, the domain wall hopping mechanism also contributes to a two-level hopping in the same form shown in Fig 3.4, which is converted into an electrical signal by the use of MTJ devices. In this case, the existence of magnetic domains of multiple shapes also provides the system with a series of different two-level flipping signals. In view of these, we can reasonably assume a distribution of a collection of τ_Z as $p(\tau_Z)$, and the power spectrum observed is expressed as:

$$S(f) = 4\int \frac{\tau_Z\, p(\tau_Z)}{(1 + \omega^2\tau_Z^2)}\, d\tau_Z$$

For a typical trap in an insulating oxide, the time constant τ_Z follows a distribution where the trapping time is distributed between τ_1, τ_2 by:

$$p(\tau_Z) = \frac{1}{\tau_Z \ln(\tau_2/\tau_1)}$$

As a result the power spectrum becomes:

$$S(f) = \frac{4}{\ln(\tau_2/\tau_1)} \frac{tan^{-1}(\omega\,\tau_2) - tan^{-1}(\omega\,\tau_1)}{\omega}$$

This is a familiar form of $1/f$ noise, comprised of a collection of Lorentzian noise, which is observed in various physical devices including MTJs. The fundamental physics for the 1/f noise is the telegraph signals obeying a Poissonian distribution. Research in literature has also been working on other possible distributions that random noise signals may follow, leading to new $1/f^{\delta}$ type of noise where δ may vary from 0.8 to 2 [53].

3.5.3 Noise mechanism in MTJs

The intrinsic noise in the MTJ junction determines its limit for low magnetic field sensing. It comprises several sources, such as the thermal, shot, and the most dominant magnetic noise, as we will discuss below[54].

The thermal noise also known as Johnson–Nyquist noise is the electronic noise generated by the thermal agitation of the charge carriers inside an electrical conductor at its equilibrium state, regardless of the applied voltage. The stochastic fluctuation of charges is well predicted by statistical mechanics, it is white noise in all frequencies, whose voltage power spectral density is given by:

$$S_v^{thermal} = 4k_B RT$$

which is only dependent on temperature T and resistance R.

Unlike thermal noise, shot noise is another type of noise coming from current fluctuations when macroscopic charge carriers start to flow. It originates from the discreteness of charge carriers like electrons, and the stochastic electron emissions process. When a finite number of charge carriers carry sufficiently small energy, one individual electron's emission or tunneling process can be considered uncorrelated with another one. Therefore the occurrence of such random events can be described by the Poisson distribution with its uncertainties. The corresponding fluctuations power spectral density is given by:

$$S_v^{shot} = 2eIR^2$$

where I is the current and e the electron charge. We see that unlike Johnson noise, shot noise is independent of temperature and resistance, only present when a current is flowing. Moreover, quantum mechanically, these two white noise mentioned above can be combined and described by:

$$S_v^{shot\&thermal} = 2eVRcoth(eV/2k_BT)$$

In the low voltage limit this reduces to $4k_BRT$, which describes equilibrium thermal noise. For the opposite limit, the system is less in equilibrium and Poissonian shot noise is obtained. For large numbers of electron events, the Poisson distribution approaches a normal distribution about its mean, and the events are no longer individually observed. On the other hand, In a tunneling system the ratio between the actual shot noise and the theoretical Poissonian value is defined as the Fano factor F[55]. It has been suggested that shot noise can be suppressed by correlations in the electron transmission, due to the Coulomb repulsion effect and Pauli Exclusion Principle, which leads to sub-Poissonian statistics and F < 1. Meanwhile, spin and charge blockade effects during tunneling lead to super-Poissonian behaviors and F > 1.

For low frequency or DC measurements, the flicker noise or also known as 1/f noise dominates over the thermal noise and shot noise previously discussed, due to its frequency-dependent characteristics. It thus becomes the most limiting factor for multiple kinds of sensors like MTJ, to reach lower detectable fields. In MTJ, the 1/f noise has both electronic and magnetic origins. It can be formulated by

$$S_v^{flicker} = \alpha V^2 / A f^{\gamma}$$

where V is the bias voltage on the junction, A the junction area, α the Hooge-like parameter, and $\gamma \sim 1$ an exponent. To understand its theoretical origin, it is closely related to random telegraph noise (RTN). RTN or so-called popcorn noise consists of sudden step-like transitions between discrete voltage levels, at random and unpredictable times. Given the dwell times of two voltage states are known, the power spectrum of such a two-level flipping process takes the shape of a Lorentzian function[56]. This spectrum is nearly flat near the origin, and after a transition region, it starts to drop quickly. On top of this, many similar two-level systems can exist with a distribution of dwell times of specific distribution functions. If the distribution function is taken as a simple uniform distribution or an Arrhenius distribution, a superposition of many independent two-level fluctuations between microscopic states altogether leads to the spectrum of the 1/f noise. In an MTJ system, the corresponding two-level systems can be categorized by an electronic part and a magnetic part. The electronic 1/f noise is due to the charge trapping of electrons inside tunnel barriers or between interfaces of multilayers in MTJ, and the magnetic 1/f noise is attributed to the thermally excited magnetization domain hopping between ripple states in magnetic layers.

Different sensors have different dominant noise types, which make them suitable for different situations. In practical experiments, the noise from electronic devices such as amplifiers also needs to be considered.

3.5.4 Fluctuation-dissipation theorem

In any sensing measurements, it is always desired that the signal fluctuation due to noise can be minimized to the limit. In addition, the sensor is supposed to be most sensitive to the external field to be detected. However, these two aspects of any type of sensor are theoretically related, as the Fluctuation-dissipation theorem will explain[57].

The dynamic process of any physics quantity influenced by the noise can be formulated by the Langevin equation:

$$m\ddot{x} + \gamma\dot{x} = F(t)$$

where $F(t)$ is a random noise force following specific distribution, and γ is the drag force to the quantity x that commonly exists in most systems. By Fourier analysis, the time average of $\dot{x}$ is given by:

$$< \dot{x} >= \frac{< F^2 >}{2\gamma m}$$

On the other hand, the equipartition theorem states that:

$$\frac{1}{2}m < \dot{x} >= \frac{1}{2}T$$

where T is the temperature. Two statements indicate that:

$$< F^2 >= 2\gamma T$$

We now turn to the definition of the susceptibility of a system. After Fourier transformation of each variable in the Langevin equation, the susceptibility χ_ω relates x and F in the frequency domain by:

$$x_\omega = F_\omega \chi_\omega$$

Deduced from the Langevin equation, the real and imaginary part of χ_ω can both be defined and given by:

$$\chi_\omega = \chi'_\omega + i\chi''_\omega = -\frac{m}{m^2\omega^2 + \gamma^2} + i\frac{\gamma/\omega}{m^2\omega^2 + \gamma^2}$$

The real part has its physical meaning of the response of a system to external forces or fields, while the physical meaning for the imaginary part is dissipation, which can be demonstrated by computing how much energy the system absorbed during the dynamic process[58], as the absorption power is:

$$\mathrm{P} = \frac{1}{2}\omega\chi''_\omega \mathrm{F}^2_\omega$$

Energy dissipation due to χ''_ω can be intuitively considered as a result of noise fluctuation, as we are about to demonstrate.

As shown in section 3.4.1, the power spectrum of noise $S(\omega)$ is the Fourier transform of the autocorrelation function $< x(0)x(\tau) >$, and can be further transformed by the relation $x_\omega = F_\omega \chi_\omega$ and Parseval's theory to be:

$$S(\omega) = \int dt \ < x(0)x(\tau) > \exp(i\omega t) = \chi_{-\omega}\chi_\omega < F^2 >= \chi_{-\omega}\chi_\omega 2\gamma T = \frac{2T}{\omega}\chi''_\omega$$

The noise spectrum of a system is shown here to be directly related to the imaginary part of its susceptibility.

The final step is to recall the well-known Kramers-Kronig relation which relates χ''_ω and χ'_ω and also $S(\omega)$ by:

$$\chi'_0 = \frac{2}{\pi}\int_0^\infty \frac{\chi''_\omega}{\omega} d\omega = \frac{1}{\pi T}\int_0^\infty S(\omega) d\omega$$

χ'_0 on the left side is just the DC sensitivity of the system. Considering the finite bandwidth of typical physical measurements, the sensitivity is approximately linear to the noise spectrum, which is the result we intend to demonstrate. Such a result from Fluctuation-dissipation is still an approximated result, where the use of equipartition theorem relies on the assumption of thermal equilibrium[59]. It has been stated that for a system of high sensitivity, the noise should rise to a high level correspondingly.

3.5.5 Random telegraph noise

As introduced in section 3.5.2, 1/f and Lorentzian noise are two forms of spectrum mainly found in nature. Random telegraph noise (RTN) is one of the former type, where the two-level flipping signal comes from the fluctuation in the charge carrier number, i.e., electrons or holes. Here we specifically focus on RTN with a Generation-recombination (GR) process origin. The electrons can be trapped by the localized states of impurity or defect, called a recombination process; the inverse process where the trapped electron transit from a local state to a delocalized one is called the generation. Electrons as the charge carrier frequently flip between the localized states of sample defects and the delocalized states in the conduction band, leading to such GR noise[60].

Assume in the random telegraph signal of GR process, the relaxation time in the trapped state and the conduction band state for the electron is τ_1 and τ_2 respectively, which is just the mean time electron spent in a state. Then the probability that that stay in the trapped stated between time 0 to t, and make a transition at t is:

$$p_1(t) = \frac{1}{\tau_1}\exp(-\frac{t}{\tau_1})$$

For the time in the conductive state, it is similar. The corresponding Lorentzian power spectrum can be deduced to be[61]:

$$S(f) = \frac{4I^2}{(\tau_1 + \tau_2)[(1/\tau_1 + 1/\tau_2)^2 + (2\pi f)^2]}$$

where I is the difference in the signal amplitude between two states. Such Lorentzian has a roll-off frequency at $1/\tau_{eff}$, where the effective transition rate $1/\tau_{eff} = 1/\tau_1 + 1/\tau_2$. The relaxation time can be related to the energy of the state by[62]:

$$\tau_1 = \tau_0 \exp\left(\frac{E_1}{\gamma k_B \mathrm{T}}\right) \Rightarrow \ln(\tau_1) \sim \frac{E_1}{\gamma k_B}\left(\frac{1}{T}\right)$$

τ_0 is an attempt frequency and for the electron migration process it is usually in nanoseconds. γ is an empirical value between 1 to 5 and E_1 is the energy of a state. The relation between the two energy levels can be schematically seen in Fig 3.8. Despite the energy difference in two states, to flip from one state to another, the electron needs to overcome a particular extra energy barrier. In this figure for state 1, E_1 can be defined as the energy difference Δ between level 1 and the barrier height. In experiments such energy can be modified by electrical gating.

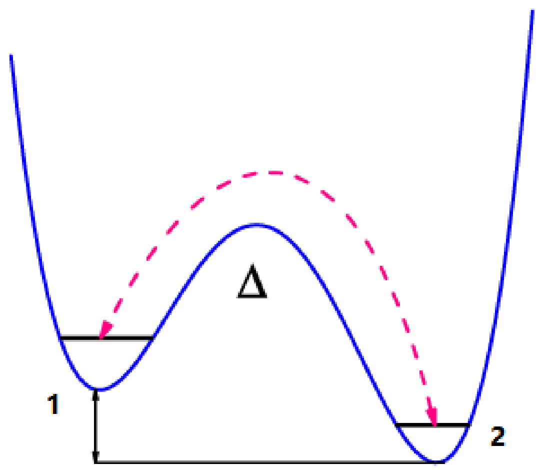

Figure 3. 8 Energy levels of two states separated by an energy barrier. The system constantly switches between two states across the barrier.

3.6 Magnetic flux concentration

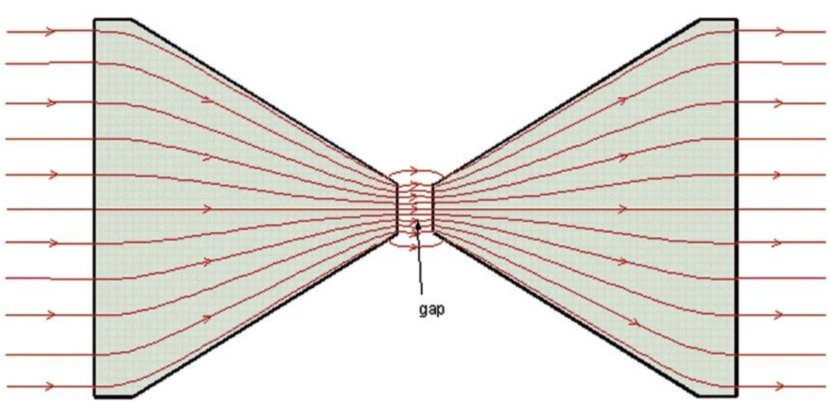

Figure 3. 9 The effect of magnetic concentration. The external magnetic flux lines (red arrows) are bent by the soft MFC and conducted into the central gap, where our MTJ sensor is located.

Magnetic flux concentrator has been applied in many devices for magnetic flux control, as a passive component, it can usually improve energy efficiency without increasing the input power or generating heat[63]. It is frequently combined with micro-electro-mechanical systems (MEMS) devices for effective frequency modulation or noise reduction[64,65]. Integrated with MTJ, it serves as a convenient field amplifier.

In the calculation of magnetostatic fields around magnetic bodies, by calculating the effective current density based on Ampere's law, the magnetic flux distribution is shown in Fig 3.9; a soft magnetic material (large permeability, low saturation field) with proper geometrical shape can guide and converge spatially uniform magnetic flux lines into a narrow region. The magnetic field is intensified in the narrow central gap, and such concentration effect is achieved with a soft material working as a magnetic flux concentrator (MFC). The amplification is proportional to the area ratio between the exit and the entry of the magnetic flux on the concentrator, resulting from the conservation of magnetic flux during the concentrating process within the MFC. The external magnetic field is uniform in the device region, which covers the MFC's total size. A larger concentrator can converge more magnetic flux in the ambiance, thus having a larger amplification effect. Moreover, increasing the magnetic permeability of concentrator material also enhances the concentration efficiency.

For the best performance of MFC, it is essential to make the material extremely soft magnetically. In the magnetron sputtering process, this means to deposit the material into a complete amorphous state, so that no crystalline structure or magnetic domain is formed. The sample can thus be rid of any magnetic anisotropy or coercive force, and a very small external magnetic field can align all its magnetic moments. Magnetron sputtering leading to a small saturation field in the material could be accomplished using high sputtering power and low sputtering gas pressure. It provides the target particles with very high kinetic energy to aggregate on the substrate chaotically to be an amorphous film.

3.7 Superparamagnetic MTJ for non-hysteretic magnetic response

3.7.1 Superparamagnetism

As a form of magnetism in small enough ferromagnetic nanoparticles or clusters, superparamagnetism appears where the magnetization of a sample can be flipping randomly under the influence of thermal fluctuation. When the measurement time is set to be much longer than this flipping time, the measured magnetization is zero as an averaged value of all flipping events. Similar to paramagnets, the magnetization of such a superparamagnetic state can also be aligned by external magnetic fields, but with a much higher magnetic susceptibility[66].

In more detail, we can express the energy of a single domain magnetic cluster briefly as:

$$E = KVsin^2(\phi - \theta) - \mu_0 M_S VHcos\phi$$

with uniaxial anisotropy energy as the first term and Zeeman energies in a magnetic field as the second. ϕ represents the angle between the saturate magnetization M_S and an external field H; θ between the easy axial and the magnetic field. This energy scales with the volume V of the single magnetic cluster, and for small enough clusters it can be overcome by thermal fluctuation energy. Therefore, when such magnetic energy barrier $\Delta E \sim KV$ is close to thermal energy $k_B T$, the magnetization would randomly flip between two directions of the magnetic easy axis, with a superparamagnetic relaxation time:

$$\tau = \tau_0 \exp(\frac{\Delta E}{k_B T})$$

where τ_0 is usually 10^{-9} s and is dependent on the magnetic parameters of the sample. Only when the measurement time is smaller than the relaxation time can we observe each magnetization state during random flipping. In more general cases, the measurement time is way larger than τ, and what we observe is an averaged magnetization between all different magnetizations, which is zero in a no biasing field situation. Under an external magnetic field that aligns the magnetic moment, the measurement longer than τ reads the net magnetization as an average in thermal equilibrium. Such equilibrium can be realized by raising the temperature, where a blocking temperature T_B leading to superparamagnetism can be defined.

3.7.2 Superparamagnetic free layer

For MTJ, raising the temperature to approach superparamagnetism is not favored in that the sensor is more preferred to work at room temperature. High temperature also leads to unwanted larger fluctuation and noise levels. Thus the magnetic energy barrier ΔE needs to bring down to a proper value for superparamagnetic behaviors, which can be done by reducing the cluster volume. It's reported in the literature that in MTJ for a free layer thin enough, a transformation from a continuous layer to tiny magnetic clusters or islands will take place during post-annealing, originated from the crystallization and diffusion process at the typical MgO/CoFeB interfaces in an MTJ.[67] Such transformation is dependent both on the free layer thickness and annealing temperature, and as a result, the clusters formed have a lognormal size distribution. These clusters have small sizes around tens of nanometers, and with such a small volume the energy barrier for magnetization flipping is low enough to be overcome by thermal fluctuation. As a result, MTJ with free layers in the shape of nanometer-sized clusters appears to be superparamagnetic, with adjustable blocking temperature near room temperature.

The distribution of the cluster size is usually assumed as:

$$f(V) = \frac{1}{\sqrt{2\pi}\sigma V}\exp(-\frac{ln^2(V/V_m)}{2\sigma^2})$$

where V_m is the average volume V and σ the deviation. V_m can be reduced by increasing the MTJ post-annealing temperature, as well as the blocking temperature. For practical applications, it is more imperative to reduce σ, so that all the magnetic clusters have uniform sizes. Uniform clusters can give clear two-level flipping signals in their superparamagnetic fluctuations, to be used in applications like random number generators.

3.7.3 Hysteresis-free linearization

Magnetic tunnel junction (MTJ) as a type of magneto-resistance device has been intensively applied in field sensors. For magnetic sensors based on MTJ, the elimination of hysteresis has been an imperative task. The bias magnetic fields, shape anisotropy, superparamagnetism, vortex magnetization, or interfacial perpendicular anisotropy (PMA) have been utilized to linearize magnetic response.[29,34,35,68,69]

Since the usual measurement time of the MTJ sensor is above the superparamagnetic relaxation time, its superparamagnetic free layer appears to have an averaged magnetization in thermal fluctuations, which is single-valued at each external field. This magnetization value is only dependent on temperature and external bias fields, thus free of any hysteresis. Sensors can benefit from it to be perfectly linear.

On the other hand, the linearity of sensors is appealing because it prevents sensitivity loss from hysteresis, which is critical for low field measurements.[27] When the magnetic fields are below the coercivity field due to sensor hysteresis, the sensor sensitivity will shrink severely. It's probably due to the microscopic magnetic domains that appear pinned in response to extremely small external fields. As a consequence of this, the sensitivity of MTJ is usually overestimated in literature, which is roughly calculated from the slope of the transfer curve regardless of the sensor hysteresis. On the other hand, by the application of superparamagnetism to make the sensor completely linear, the hysteresis is eliminated and so does such sensitivity loss. It is better to measure sensitivity experimentally by real field testing[70]. By applying a microtesla testing magnetic field we observed that such sensitivity shrinks by 2 to 5 times in coercive MTJs, while in linear MTJs it does not. Therefore, linearization not only provides sensors with the merit of being single-valued, but also enable the sensor to detect lower magnetic fields than other coercive sensors, even those with seemingly higher sensitivity.

3.8 Vortex magnetic states

3.8.1 Energetics of vortex topology

Vortex magnetization has been found in micrometer scale disks as the ground state. It has drawn increasing interest to be nano oscillators, with its fast spin dynamics and broad spin-wave spectrum[71,72]. In our study, we will take advantage of its unique spin textures to make a magnetic sensor. In a ferromagnetic system, the exchange energy, the magneto-static energy, the magneto-crystalline and so on all contribute to the total magnetic energy and dictate the magnetization reversal process of ferromagnets. For single-crystalline dots, the magnetocrystalline anisotropy is the most important factor. For our MTJ ferromagnetic free layers which are polycrystalline, there is no crystalline order and their magnetic behaviors are mainly determined by the geometry and shape. Speaking of energy, it is in principle determined by the competition between the magneto-static energy that is also called demagnetization energy, the exchange energy, and the Zeeman energy when external fields are present. When the thickness t of the free layer exceeds the exchange length $R_0 = \sqrt{C/M_s}$, where C is the exchange stiffness and M_s is the saturation magnetization, the vortex magnetization becomes energetically favored for the elimination of demagnetization energy.

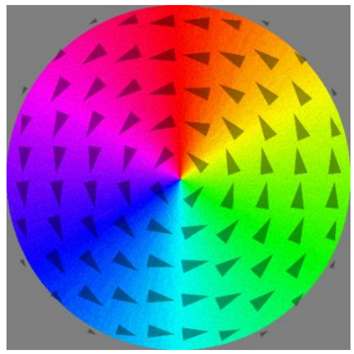

Figure 3. 10 The schematic of the vortex magnetization in a ferromagnetic disk (top view); the arrow and color indicate the in-plane magnetization.

Presented in Fig 3.10, The magnetization distribution of a curling vortex in a flat disk of radius R, with a vortex core where the magnetic moment aligns in the out-of-plane z-direction, can be mathematically expressed in polar coordinates as[73]:

$$m_\rho = 0, m_\theta = \begin{cases} sin\theta = \dfrac{2b\rho}{b^2+\rho^2} & \rho \leq b \\ 1 & \rho > b \end{cases}, m_Z = \begin{cases} \pm cos\theta & \rho \leq b \\ 0 & \rho > b \end{cases}$$

where b is defined as the radius of the vortex core. Under an external magnetic field, the vortex core moves from the disk center toward the perimeter to increase the magnetization component along the field. We define the ratio between the core displacement l and the disk radius as the relative displacement $s = l/R$, and the disk aspect ratio $\beta = t/R$. The exchange energy density can be written and expanded as:

$$w_{ex}(s) = w_{ex}(0) + \frac{1}{2}\left(\frac{R_0}{R}\right)^2 \ln(1 - s^2) \approx w_{ex}(0) - \frac{1}{2}(\frac{R_0}{R})^2 s^2$$

Under external magnetic field H, we define $h = H/M_s$. For small vortex displacement s, the Zeeman energy term can be approximated as:

$$w_{ex}(s) \approx -hs$$

The magneto-static energy is generated by surface magnetic charges $\sigma = \boldsymbol{M} \cdot \boldsymbol{n}$, which can be utterly minimized by forming a vortex magnetization distribution. It can be expressed and approximated for small vortex displacement s as:

$$w_m(s) = \frac{2}{\pi} s^2 \sum_{\mu} F_\mu(\beta) {I_\mu}^2(s) \approx w_m(0) + 2\pi F_1(\beta) s^2$$

where $F_\mu(\beta) = \int_0^\infty \frac{dt}{t}\left[1 - \frac{1-\exp(-\beta t)}{\beta t}\right] J_\mu^2(t), I_\mu(s) = 2\int_0^\pi d\varphi \frac{\sin(\varphi)\sin(\mu\varphi)}{\sqrt{1-2s\cos(\varphi)+s^2}}$,

and J_μ is the Bessel function of μth order. The total energy as a sum of these three terms is:

$$w(s) \approx w(0) + as^2 - hs$$

where $a = 2\pi F_1(\beta) - \frac{1}{2}(\frac{R_0}{R})^2$.

The vortex core position s at each external magnetic field can be found by minimizing $w(s)$ with respect to s, to give a simple equation as:

$$s = \frac{1}{2a} h$$

The vortex annihilation field h_{an} can be found by the condition $s = l/R = 1$ where the vortex already moves to the edge of the disk:

$$h_{an} = 2a$$

The vortex nucleation field h_n can be found as the field below which an originally collinear spin structure becomes unfavored energetically:

$$h_n = 4\pi[F_1(\beta) - F_2(\beta) - \frac{1}{\pi}(\frac{R_0}{R})^2]$$

By analyzing the total magnetic energy, the critical fields are predicted which further reveal the magnetization evolution and phase can transition for ferromagnetic disks of various parameters. In addition, the motion of the vortex core can also be solved from Landau–Lifshitz–Gilbert equation and Thiele's equation, where the vortex center is shown to behave like an object with defined mass tensor M and two-dimensional coordinate $\boldsymbol{X}$ [74,75]:

$$M\ddot{\boldsymbol{X}} - \boldsymbol{G} \times \dot{\boldsymbol{X}} + \partial_{\boldsymbol{X}} W(\boldsymbol{X}) = 0$$

$W(\boldsymbol{X})$ is the magnetic energy mentioned above when the vortex has displacement from the equilibrium position, and $\boldsymbol{G}$ the gyrovector with a gyromagnetic ratio related to the topological charges of the vortex. The vortex core position is further related to magnetoresistance, and we will demonstrate this with simulated images in chapter 5.

3.8.2 Field-induced motion of vortex magnetization and linear magnetic response

Besides the single vortex theoretically described above in 3.8.1, other spin textures also exist such as anti-vortex, double vortices and even more[76]. Different topological spin textures are characterized by three topological charges: the vorticity q, the polarity p and the chirality c[77]. Generally speaking, the vorticity indicates the manner magnetic moments curl in the plane; the polarity defines the relative orientation of the vortex core magnetization; the chirality tells the rotation of the spins around the vortex. As the magnetization evolves under external magnetic fields continuously, the topological charges preserve its value, thus the spin texture is under topological protection. It can only be broken by extreme conditions such as large fields driving the vortex core to the edge of ferromagnets. As a result, one type of vortex topology cannot transform into other topologies or uniform magnetization in small ambient fluctuations, which provides great thermal stability.

However, multiple non-trivial spin textures could exist with the same topological charges, leading to hysteresis in ferromagnets with vortex topologies. For double vortices, two non-degenerate spin textures could exist as indicated in Fig 3.11. These two mirror spin textures are both energetically stable, and their vortices move in opposite directions under external magnetic fields. Their average magnetizations are different even at the same external field, so their tunneling magnetoresistance will show differently in MTJs. In view of this, the magnetic hysteresis appearing in the transfer curve can be reasonably attributed to the non-degeneracy of possible spin textures. On the other hand, a single vortex is symmetrical with all configurations substantially degenerate, which prohibits the existence of hysteresis.

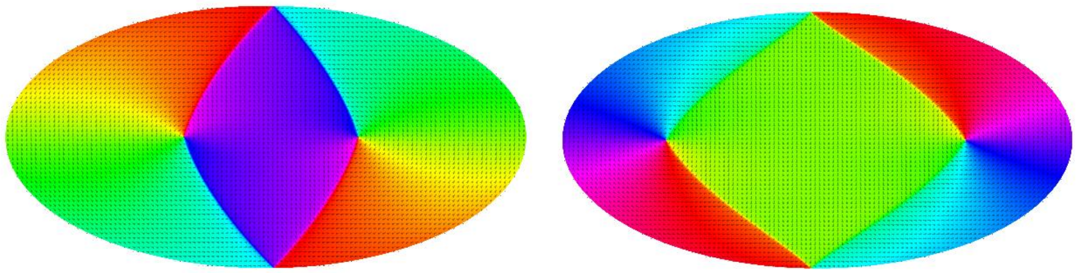

Figure 3. 11 The non-degenerate spin textures of double vortices magnetization in an oval thin-film disk; the color changing from green to blue corresponds to the spin direction rotating from upward to downward clockwise.

As mentioned in section 3.7.3, including the use of a superparamagnetic free layer, many strategies have been adopted to achieve hysteresis-free response in high sensitivity magneto-resistive sensors [78-82]. Linearization strategies like hard axis measurement, secondary orthogonal annealing, and the use of perpendicular magnetic anisotropy all focused on common ferromagnetic systems of collinear magnetizations. In addition to this type of method, superparamagnetic sensors explored a system beyond ferromagnetic ones. Moreover, here we have introduced single vortex magnetization beyond collinear systems as well, which also provides a linear magnetic response. The linearity in single vortex magnetization lies in its topologically protected magnetization, where there are no degenerate textures and the topological charges conserve their value all the time. In this way, at each magnetic field the magnetization pattern is unique without dependence on the measurement history. This leads to reversible behaviors in its magnetization evolution under external magnetic fields, and an MTJ with the free layer in such a vortex state can show a corresponding linear response.

3.9 Perpendicular magnetic anisotropy (PMA)

3.9.1 Tuning magnetic anisotropy

The method of generating controllable PMA in MTJ is widely studied, which turns out to coexist well with a good magnetoresistance ratio (TMR).[83] A controllable PMA not only can reduce hysteresis, but also provide a way to improve the sensing performance. Meanwhile, perpendicular MTJ (pMTJ) is an important device in the microelectronics industry, mostly contributing to reading head and magnetic memory. One important property is the thermal stability Δ of pMTJ, which mainly comes from the magnetic coercivity due to PMA. pMTJ with a large coercive field observed in the transfer curve is less likely to accidentally switch its magnetization due to thermal fluctuations. On the other hand, the magnetization state of pMTJ needs to be switched by a spin-polarized current I_c in STT-MRAM. For stronger PMA, a larger I_c is need to start the spin precession in the MTJ free layer, which means more energy and time consumption in the data writing operations. Therefore, a trade-off exists between the long-term stability and the writing speed in such logic devices, where methods are desired to manipulate the PMA strength and thereby the Δ / I_c value[84]. As Voltage controlled magnetic anisotropy (VCMA) turns out to be an effective way to change the PMA strength K_i, K_i also exhibits a strong temperature dependence[31,85]. The task of PMA tuning with high application value can also be studied by other factors in the layer stack, such as the influence of the capping layer, the interlayer exchange coupling, or composite layer structures [86-88].

In a thin-film layer like the free layer in MTJ, the effective anisotropy constant is generally expressed by:

$$K_{eff} = \frac{K_i(T, V)}{t} - K_S$$

while K_i is tunable by temperature T, and bias voltage V, the layer thickness t, and the in-plane anisotropy K_S also provide convenient ways to control the overall magnetic response. For magnetic field sensing, these factors including PMA can all be designed to realize an optimal state, where the magnetization is most responsive to the external field and noise fluctuation is prohibited by an appropriate amount of magnetic anisotropy[89].

3.9.2 Interlayer PMA

As perpendicular magnetic anisotropy (PMA) has been induced in the MTJ free layer, pMTJ has been widely studied for its high access speed, complementary metal-oxide semiconductor(CMOS) compatibility, and potential non-volatile data storage in magnetic random access memory (MRAM)[90,91]. The parallel or anti-parallel magnetization state in pMTJ is used to represent the logic “1” or “0” in a bit cell. To manipulate the magnetization in pMTJ in a field-free manner, spin-transfer torque magnetic random access memory (STT-MRAM) is also drawing much attention, as an effective way to drive the magnetization by an electrical current in the adjacent layer, which inflicts a spin-transfer torque to the perpendicularly magnetized free layer of MTJ by spin Hall effect [92-95]. In addition to the use of STT, by modifying the PMA strength in MTJ with a method like VCMA, magnetization switching can also be achieved conveniently with less amount of operating current and thus less energy consumption[96,97].

With all its important applications, PMA is theoretically understood to originate from the interface between the MgO and CoFeB layer with perpendicular (001) crystalline structure, and attributed to electron orbital hybridization. More specifically, it is the overlap between the p orbitals of Oxygen atoms and d orbitals of the transition metals like Co, by the interaction of spin-orbit coupling. In other cases like Co/Pt interface, it is the hybridization between the 3d orbitals of transition metal Co and 5d orbitals of heavy metal Pt[98]. The physical origin of the PMA effect induced by orbital hybridization is explained by tight-binding theory, whose details are further given by first-principle calculations or ab initio simulation[99]. For those spin-polarized band near the Fermi surface, the hybridization due to spin-orbit coupling interaction (SOI) will lift the degeneracy in the bands with different orbital characters like d_{xy}, d_{yz}. Due to energy splitting in bands with different spatial orientations, a certain band with increased energy can appear above the Fermi surface to be unfilled. Therefore, the wave function character of such electron band loses its symmetry and obtains a spatial preference. Since the spin is influenced by the SOI energy, such spatial preference in the orbital wave function appears correspondingly in the spin orientation. As a result, electron spins coupled to the orbital wave function in the newly hybridized band can have the corresponding spatial preference. With spin up or down states in the out-of-plane direction of the lowest energy, such preference is the origin of interfacial PMA. Whether up or down state becomes the ground state is dependent on the history of external field scan, which is typically just denoted as majority or minority states. For instance in Fe/MgO interface, with SOI turned on, the degeneracy will be lifted in the original electronic bands d_{z2}, d_{xy}, d_{yz}, d_{x2-y2}, d_{xy} of 3d orbital character in Fe and the band with p_z orbital character in O. The resultant hybridized band with d_{z2}, d_{xz}, d_{yz} and p_z character are low in energy to be filled. In these characteristic orbitals, the spin is more preferred to be aligned in the out-of-plane "z" direction due to SOI. The interface thus provides large PMA due to the hybridization between Fe and O orbitals. The hybridized bands even exhibit higher spin polarization than the original ones.

It is also noteworthy that spin filtering phenomenon as the origin of high magnetoresistance ratio of MgO-based MTJ can be found in the calculation for CoFeB/MgO interface in the meantime, indicating the coexistence of TMR and PMA at the interface. The PMA value predicted by these orbital hybridization models is for ideal interfaces, as large as 1.3 erg/cm^2 for a CoFeB/MgO interface. However, just like the overestimated TMR value, experimentally PMA can also be severely reduced from theory due to sample imperfections, most likely because of over or under oxidized interfaces.

Chapter 4 Magnetic Flux Concentration (MFC) for Ultrasensitive Magnetic Sensing

4.1 Introduction

In this chapter, the magnetic flux concentrators (MFC) will be combined with our MTJ sensors for improved performance. As MFC is theoretically introduced in section 3.6, different MFC types are studied here by COMSOL simulation, guiding us to determine the best MFC design. The fabrication conditions of MFC are studied by iterations of samples to find the best fabrication condition. After that, we will introduce how MFC can be conveniently integrated onto a microscopic MTJ to give a high amplification factor. A complete magnetic field sensing device is developed with our MTJ and MFC, integrated on a printed circuit board with computer communication. The new device gives an unprecedented field detectability into the region of pico-tesla magnetic fields.

4.2 COMSOL simulation

To find the most effective geometrical shape of MFC giving the highest amplification factor, the optimal design of MFC is studied by software simulation. The software we use is COMSOL Multiphysics, which can calculate the magnetic field distribution based on magnetostatic equations by the finite element method. To proceed with the simulation, the input parameters of COMSOL include the magnetic properties of each material used in the model, the simulation meshing size, and the initial conditions. Fig 4.1 below are the simulated figures for a pair of trapezoid MFCs:

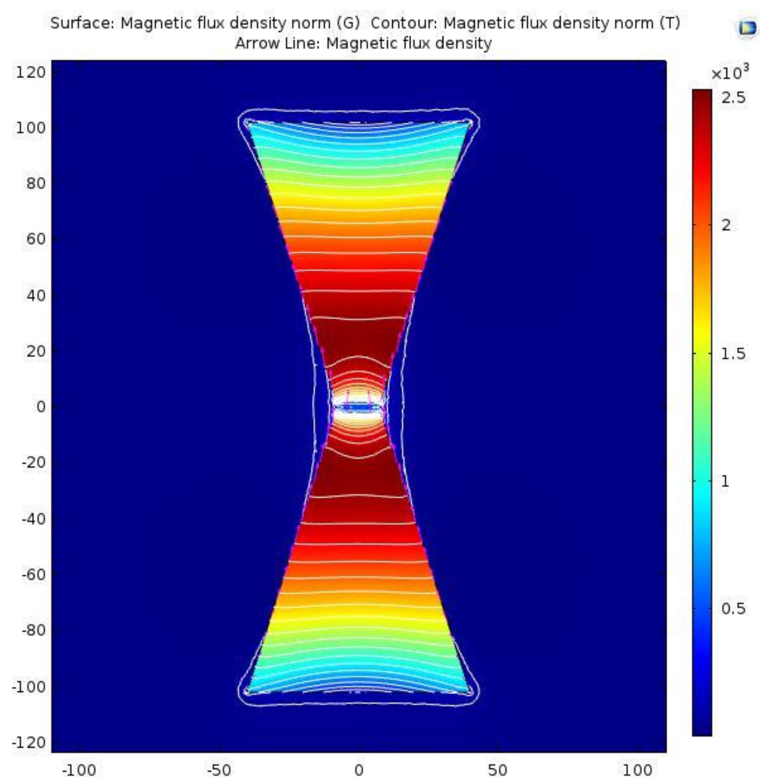

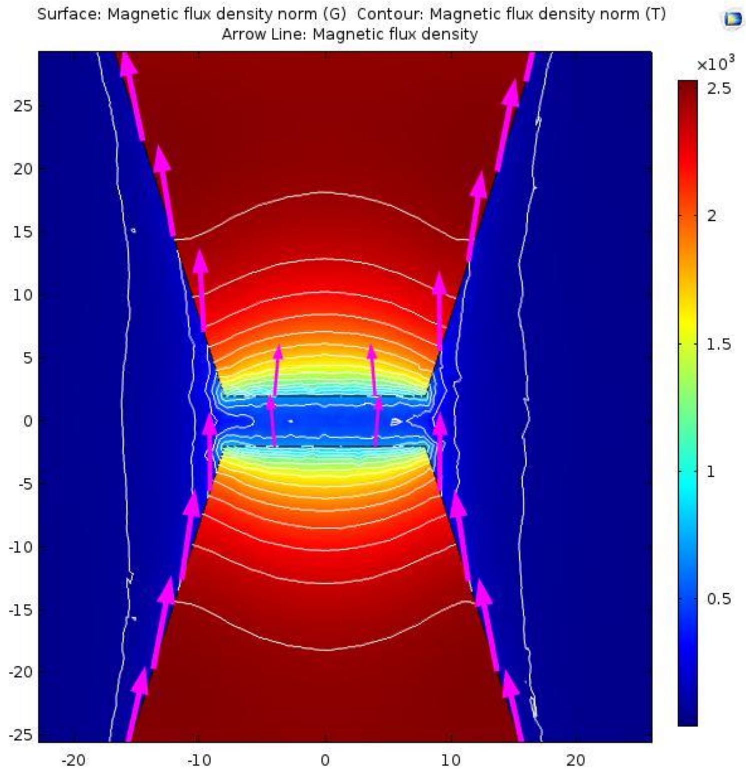

Figure 4. 1 Typical simulation results of COMSOL Multiphysics. The colors indicate the intensity of magnetization, while the arrows indicate the stray magnetic fields.

As simulations reveal, the most determinant factors for the concentration efficiency are the magnetic permeability, the geometrical shapes and the gap between two MFCs. The amplification factor is defined as the ratio between the field strength in the gap and outside the concentrators. Different shapes of MFC have been investigated, and the shape of trapezoid turns out to be one of the shapes giving the highest amplification factors. As shown in Fig 4.1, with the relative permeability of MFC set as 3282, the length of one MFC trapezoid 100 μm, the tip width 18 μm, the gap distance 4 μm, and the thickness of flux concentrator 2 μm, the magnetic field in the MFC gap is magnified by a factor of 23.25. The simulated result cannot be directly compared with the experiment, since the condition of

MFC is oversimplified. The permeability 3282 as a later experimental value measured from large bulk CoZrNb samples we will introduce later, which can be different from a patterned MFC. But the relation between the amplification factor and each MFC parameter is valid. Simulations show that the amplification factor is linearly proportional to the length, the tip width and the thickness of the concentrator, and inversely proportional to the gap separation distance. The magnetic field is uniform in the space between the tips of two MFCs. It is also found that the highest amplification can be achieved when the gap distance equals the MFC thickness.

4.3 MFC-MTJ integration

4.3.1 MFC material: preparation and optimization

Magnetic permeability is the most important property of a flux concentrator, to allow small external magnetic fields to induce large magnetization in the material. Soft magnetic materials are of high permeability, and they can converge more flux lines as MFCs[100]. These materials are usually amorphous alloys like Permalloy ($Ni_{80}Fe_{20}$), and for our MFC we used $Co_{88}Zr_4Nb_8$ (CZN), whose permeability is as high as 3~4 thousand with nearly zero coercivity below 1 Oe, measured by the vibrating-sample magnetometer (VSM). The best fabrication condition of CZN is precisely tuned to be: a base vacuum pressure 1.8×10-7 Torr, Ar gas sputtering pressure 5.0×10-4 Torr, DC sputtering power 100W, and CZN film thickness 1200 nm. The purity of the material, a good vacuum condition, proper sputtering pressure, and power are vital to make this material magnetically soft, with a hysteresis loop given in Fig 4.2[101].

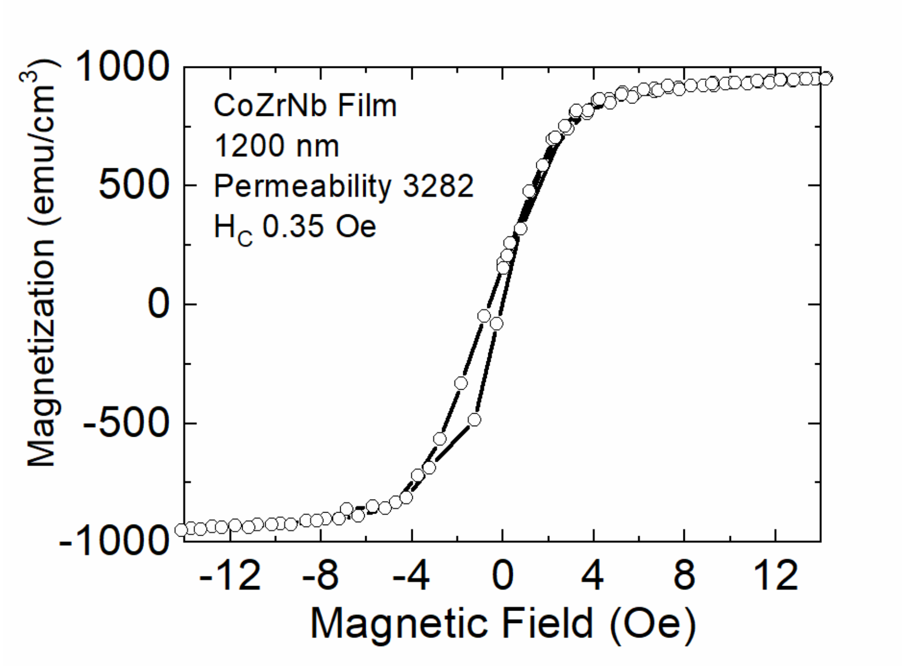

Figure 4. 2 The magnetic hysteresis loop of CZN bulk thin film in the shape of a centimeter-sized square, with 1200 nm thickness.

To make CZN magnetically soft, it needs to become amorphous instead of forming any crystalline structure where anisotropy originates. As a result, the sputtering power needs to be as high as one to two hundred watts, to ensure the particles accumulate on the substrate in a disordered manner. Another possible technique is to cool down the sample substrate during sputtering because this could freeze the sample in its non-equilibrium amorphous state.

4.3.2 Patterning and configuration

With this soft material used for flux concentration, we designed an MTJ sensor integrated with a pair of trapezoid CZN MFCs. All components are patterned using photolithography onto the silicon substrate, and the single MFC layer is much thicker than MTJ multilayers. Four oval-shaped MTJs are connected in series, placed in the middle 30 μm wide gap between two MFCs. Two gold contact pads are on both sides of this sensing unit, for external connection to electronic devices. In the COMSOL simulation performed based on the configuration of this sensor, the magnetic flux is mostly conducted into the gap and is uniform among all four MTJs. The gap is set as small as possible for the least magnetic flux leakage, up to the special resolution limit of our photolithography. The thickness of MFC is 1200 nm which requires an hour to sputter. Bigger or thicker concentrators can provide even larger amplification.

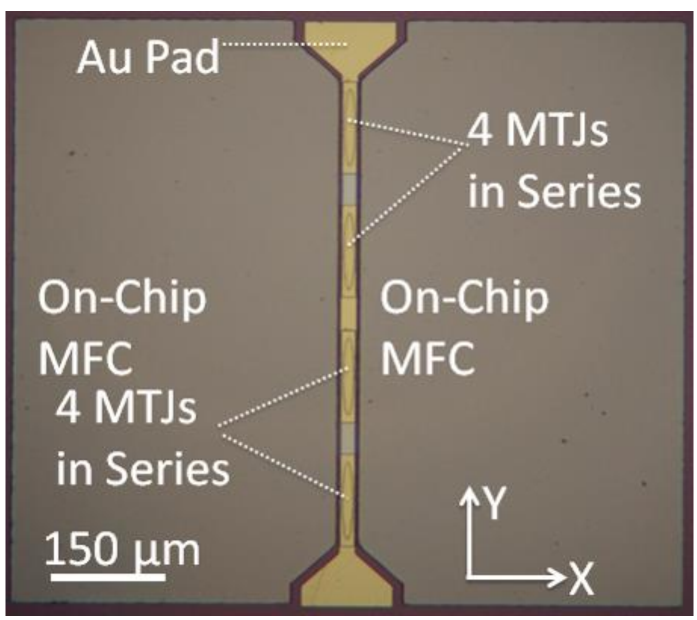

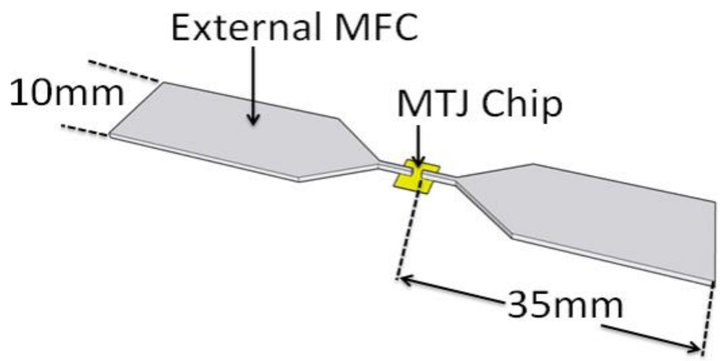

Figure 4. 3 The microscopic view of the on-chip concentrator pair integrated with MTJ sensors (top), and the external MFCs as a second-stage concentration (bottom).

On the top figure of Fig 4.3, a pair of trapezoid CZN MFCs is called "on-chip" concentrators for their minimized sizes, whose total area is only 1x1 mm^2. After this first stage of magnetic field concentration, another pair of second-stage concentrators of much larger size is placed to further concentrate the field, on the bottom figure of Figure 4.3. These macroscopic MFCs are much bigger, cut from a bulk metallic sheet of 0.5 mm thick. They are made of Conetic ®alloy ($Ni_{77}Fe_{14}Cu_5Mo_4$), which is directly bought from the manufacturer and carries a lower permeability of 18.8. As a measured result, the amplification factor for the first-stage "on-chip" MFC is 16.8, and for the second-stage macroscopic MFC it's 30.8. In total they give an amplification of 517 times for external magnetic fields. An overall transfer curve for MTJs with single-staged or double-staged MFCs is given in Fig 4.4, with boosted sensitivities.[101]

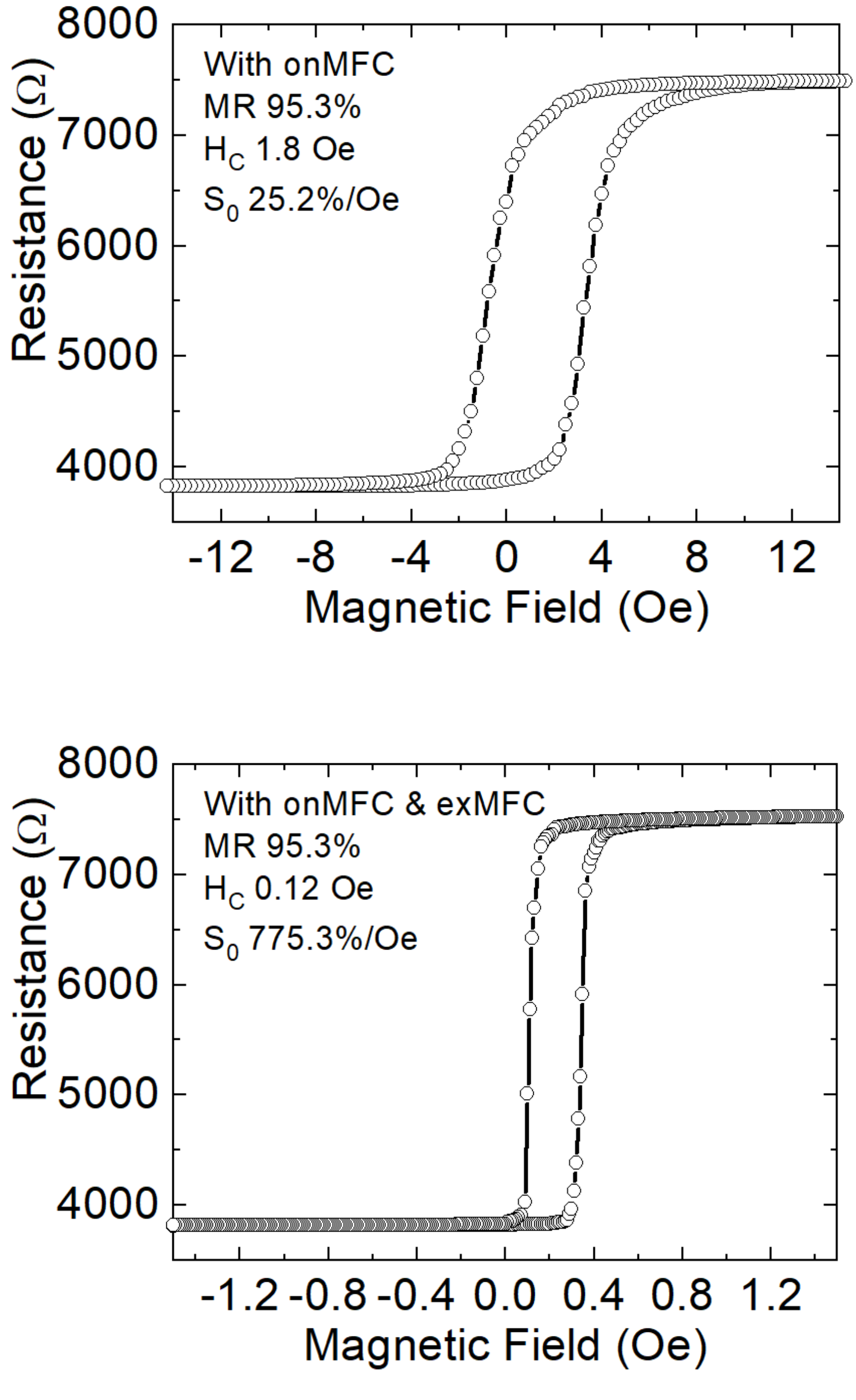

Figure 4. 4 The transfer curve of MTJs integrated with single-staged or double-staged MFCs.

4.4 Pico-tesla-scale field sensing

4.4.1 Signal conditioning and calibration

A magnetic sensor prototype is developed, with all necessary electronics designed on a printed-circuit-board (PCB), where the sensors will mount on. As shown in Fig 4.5, a 1.5 V bias voltage empowers the MTJ, and the MTJ signal will be amplified on the PCB and collected by a data acquisition device. A function generator (Agilent 33220A) is connected to a pair of standard coils near the sensor and also a current limiting resistor R_2, to generate an AC testing field. One additional coil is used to apply a DC biasing field, which makes the sensor operate at a high sensitivity and is not shown in the diagram. The voltage signal from MTJ passes to an amplifier, and then to a lock-in amplifier with negligible FET type input voltage noise of 5 nV/√Hz. The low-pass filter of the lock-in amplifier is set beforehand to output a filtered signal with a time constant of 5s and a slope of 24dB/octave, corresponding to an equivalent noise bandwidth of 0.024 Hz. During the measurement, an AC testing magnetic field is applied at various amplitudes, and an oscilloscope is used to record stabilized outputs from a lock-in amplifier for 100s. The mean value of the recorded output denotes the sensor's voltage signal in response to the testing field. Its fluctuation in time is equivalent to the noise level of the sensor, which represents the standard deviation in the signal.

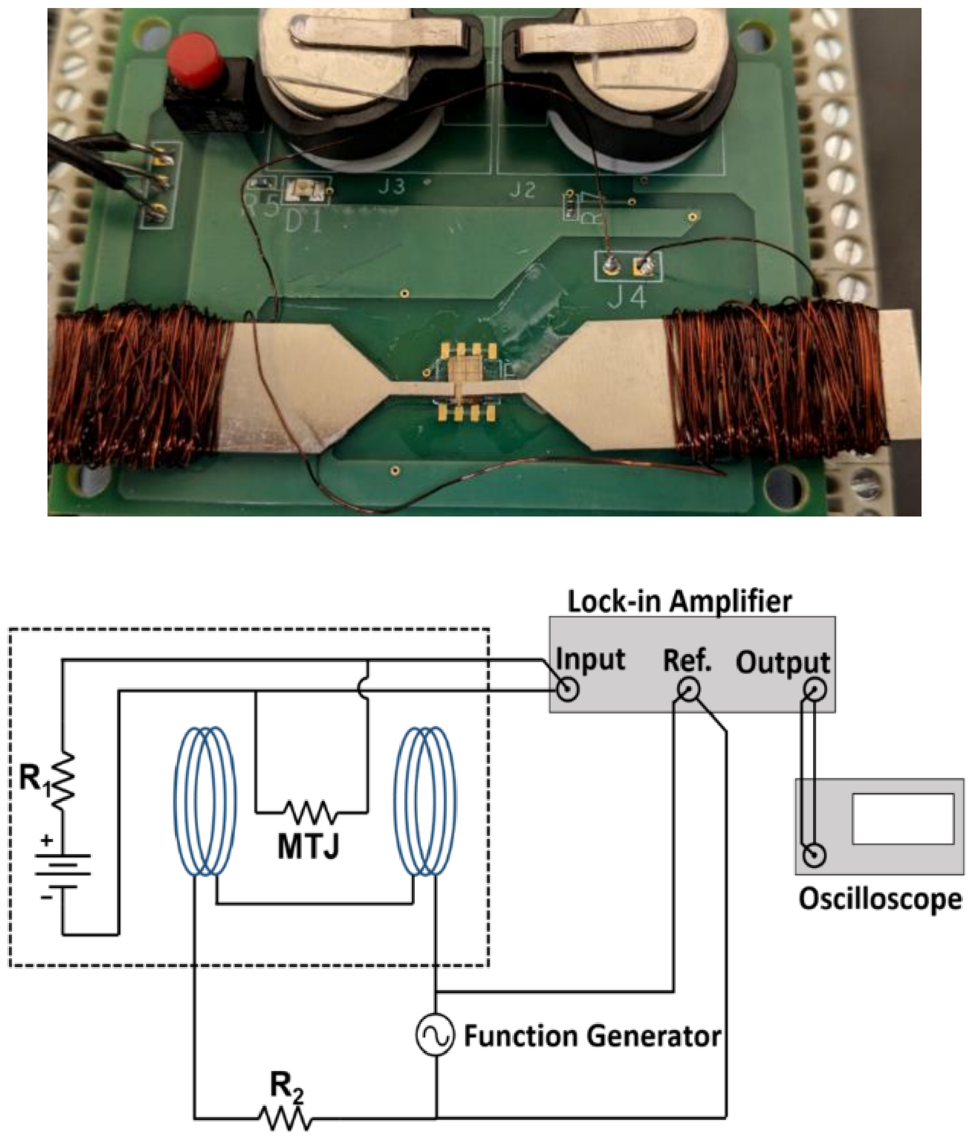

Figure 4. 5 The MTJ- MFC sensing prototype with batteries, amplifiers and data acquisition electronics is shown in the top figure. At the bottom is the experimental device used to test the prototype, where the testing fields are generated by a function generator. The MTJ signal is observed after lock-in amplification in an oscilloscope.

4.4.2 Sensor characterization

Measurements are done with this magnetic sensor prototype, where the magnetic fields generated by the pair of coils introduced in Fig 4.5 are measured. The magnetic field amplitude is controlled by the voltage supplied by the oscilloscope. The frequency remains constant for the top result, and is varied in the bottom. As the top diagram in Fig. 4.6 shows, at 10 kHz, the voltage signal decreases as the amplitude of the AC testing field gets smaller. The res line for the signal-to-noise ratio (SNR) at each point is also given, which includes the signal fluctuation information. In this measurement, the AC testing field is reduced gradually from 120 to 5 pT (pico-tesla). In the meantime, the SNR value drops to approximately 1, which we consider as a standard that the signal is invisible in the noise fluctuation. Under these criteria, we have realized an ultra-low detectable magnetic field of 5 pT at this frequency.

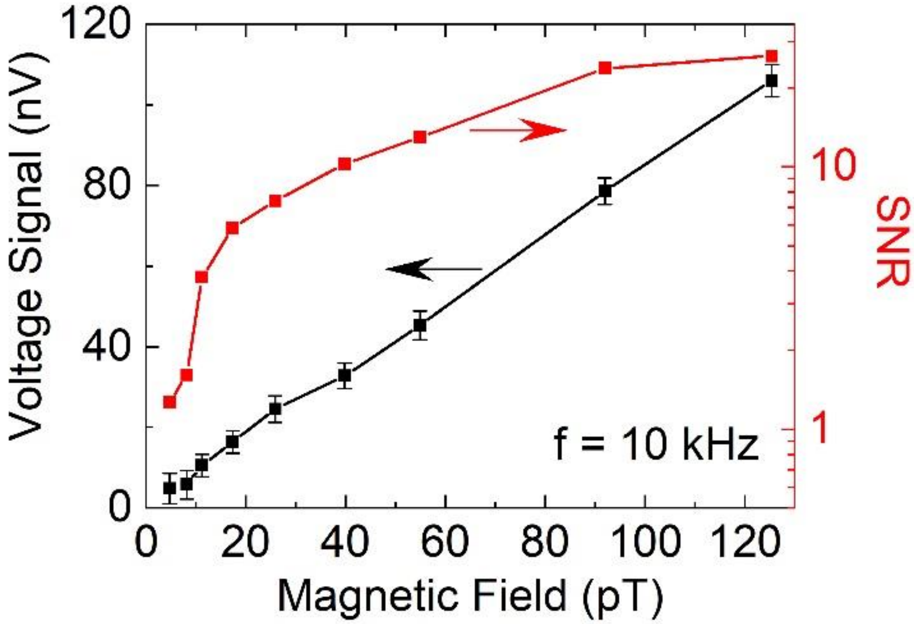

Voltage Signal (nV)
SNR
f = 10 kHz
Magnetic Field (pT)

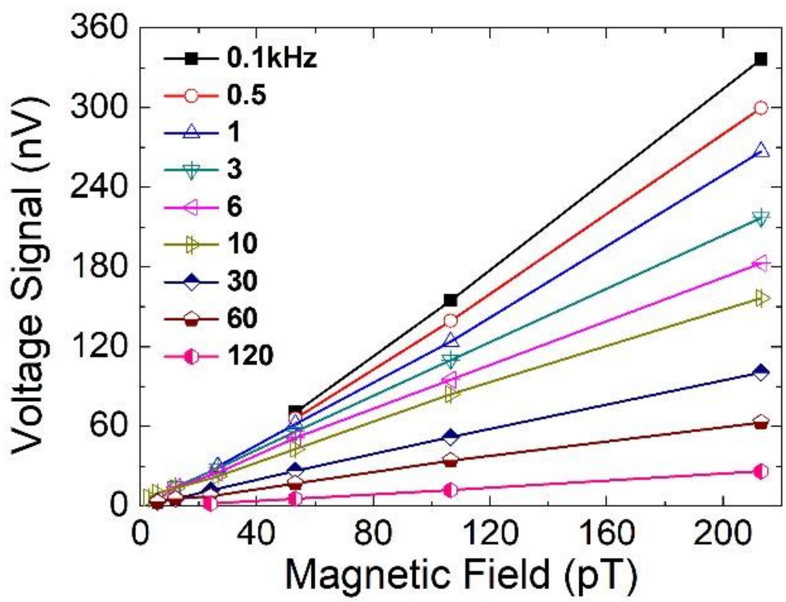

0.1kHz
0.5
1
3
6
10
30
60
120
Voltage Signal (nV)
Magnetic Field (pT)

Figure 4. 6 The voltage signal and SNR measured by the lock-in amplifier as a function of the amplitude of the testing AC magnetic field at 10 kHz, and measured at different frequencies.

In literature [27,100,102,103], it is always ignored that sensor response has its frequency dependence, and the sensitivity is directly given by the transfer curve. However, here we find that the sensor sensitivity, to be determined from the line slope, has a close relation to the magnetic field frequencies. As shown in Fig. 4.6 (bottom), the slope of the line is gradually decreasing as frequency rises, indicating a clear drop in the sensitivities. This could be due to the eddy currents induced by high-frequency magnetic fields in the MFC, which generates magnetic fields to counteract the magnetic flux concentrated from outside.

On the other hand, by directly measuring the standard deviation of the voltage signals in the oscilloscope in Fig 4.5, we characterize the noise fluctuation at different frequencies from the result after frequency lock-in. Mathematically, its noise power spectral density is given by dividing the standard deviation of the signal by the square root of the equivalent noise bandwidth of the lock-in amplifier, and is plotted in the top of Fig 4.7. In the low-frequency domain below 10 kHz, the noise of MTJ is dominated by 1/f noise, which is in accord with the discussion in section 3.4.3. Above 10 kHz, the 1/f noise is mostly contributed by the frequency-independent white noise, originated from Johnson and shot noise. The total voltage noise at all frequencies can be together described by the formula:

$$S_V(V^2/Hz) = 2eVRcoth\left(\frac{eV}{2k_BT}\right) + \frac{\alpha V^2}{Af^\gamma} \tag{4.1}$$

V is the bias voltage on MTJ, *R* is the MTJ resistance, and *A* is the junction area. The first term is a combination of the Johnson and shot noise, and the second term is the *1/f* noise characterized by Hooge-like parameter α and exponent $\gamma \approx 1$.

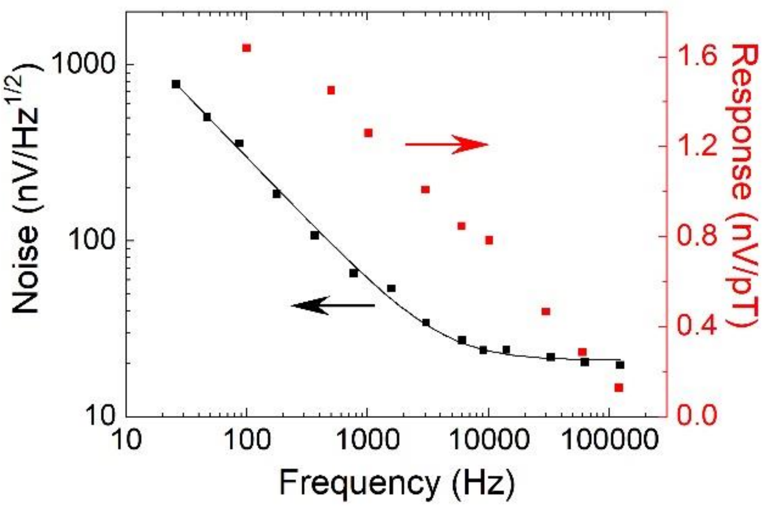

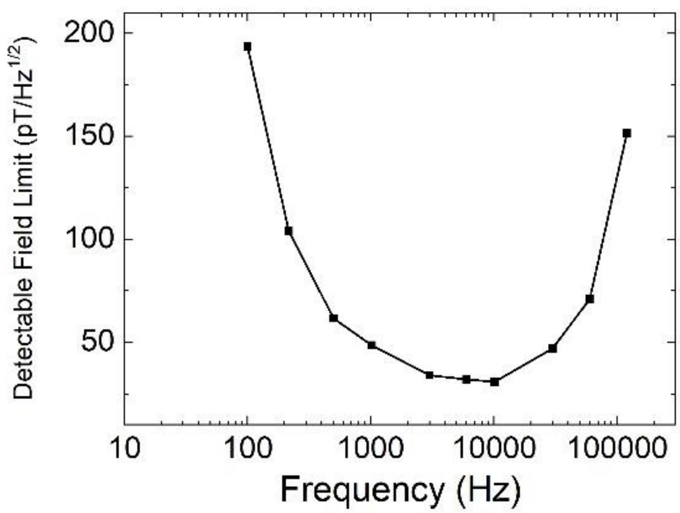

Figure 4. 7 In the top figure, the noise spectrum for an MTJ sensor with double-staged MFCs, with the black solid line as theoretical noise fitting; the sensitivity is shown on the right axis. The detectable field limits are calculated from them and shown at the bottom.

The lowest detectable magnetic field is found from the ratio between noise (black points) and response (red points), calculated at the end of Fig 4.7. The change of noise and response as a function of frequency are not simultaneous, and at different frequencies, the trends are also different. At low frequencies, due to the dominant 1/f noise interference, the sensor has a poor DC signal detectability. The field detectability is $200\ \mathrm{pT}/\sqrt{\mathrm{Hz}}$ for measuring the static magnetic field. It's best to use the sensor at higher frequencies of a few kHz, where the sensor remains sensitive and the 1/f noise is no longer observed. Optimal performance is achieved at 10 kHz, with a low field detectability of $30\mathrm{pT}/\sqrt{\mathrm{Hz}}$, enabling pico-tesla field sensing.

There is still room for further improvement in the noise performance of MTJ, and more importantly in the MFC. The *1/f* noise of the MTJ sensors could be reduced further by atomic layer engineering. The gap distance and shapes of MFC have great room for improvement, as people have made the gap near 0.5 mm[104]. Cutting a small notch at the tip of

MFC is also turned out to be a very effective modification of its shape, leading to much concentrated magnetic flux in the vertical direction [27]. By revising the sputtering condition, the dual MFC materials can be made more magnetic permeable. With all these continuing optimization methods, an ultimate goal is expected to reach sub-pico-tesla level.

Chapter 5 Hysteresis Elimination Using Superparamagnetism and Vortex Magnetic States

5.1 Introduction

Hysteresis is an inevitable issue in sensing technology, which precludes the sensor from a desired linear response. In this chapter, we will focus on two solutions in our MTJs. The theoretical introduction of this chapter is in sections 3.7 and 3.8. We have first modified MTJs by making its free layer superparamagnetic. A temperature-dependent transition from ferromagnetic to superparamagnetic states is observed in them due to the nanometer-sized magnetic clusters formed in the free layer. With the sensor performance characterized for each state, we found a non-hysteretic response with the best sensing performance. Another method is to create a magnetization with vortex magnetization in the MTJ free layer. We will first study its geometrical dependence by micro-magnetic simulations. Afterward, we experimentally fabricated vortex MTJs with behaviors in consistence with simulation. From the detailed characterization of this vortex MTJ, it turns out to be a better non-hysteretic sensor with an unprecedentedly high dynamic reserve. Different scaling relations between sensitivity and noise will be revealed for different MTJs, leading to several conclusions for a general magnetic sensor.

5.2 Superparamagnetic MTJ

5.2.1 Superparamagnetic clusters

As mentioned earlier in section 3.7.2, the ferromagnetic free layer CoFeB in MTJ can become superparamagnetic after the continuous thin-film structure breaks into nanoscale clusters during the post-annealing process. Generally speaking, the higher the annealing temperature leads to clusters of smaller volume. A single superparamagnetic cluster has a magnetoresistance transfer curve following the Langevin equation as:

$$R(H) = C_1 L\left(\frac{\mathrm{m}H}{k_B T}\right) + C_2$$

T is the temperature, m the magnetic moment of one cluster, and C_1 and C_2 are fitting constants. According to actual circumstances, an offset field intrinsic to MTJ might be added to the equation. We can assume that the magnetic moment of one cluster is proportional to its size, and both the magnetic moment and the nanocluster size follows a lognormal distribution. The detailed parameters of the distribution can be obtained by fitting the equation to an experimental MTJ transfer curve, which is from an experimental transfer curve data points measured at 400K in the top figure of Fig 5.1.

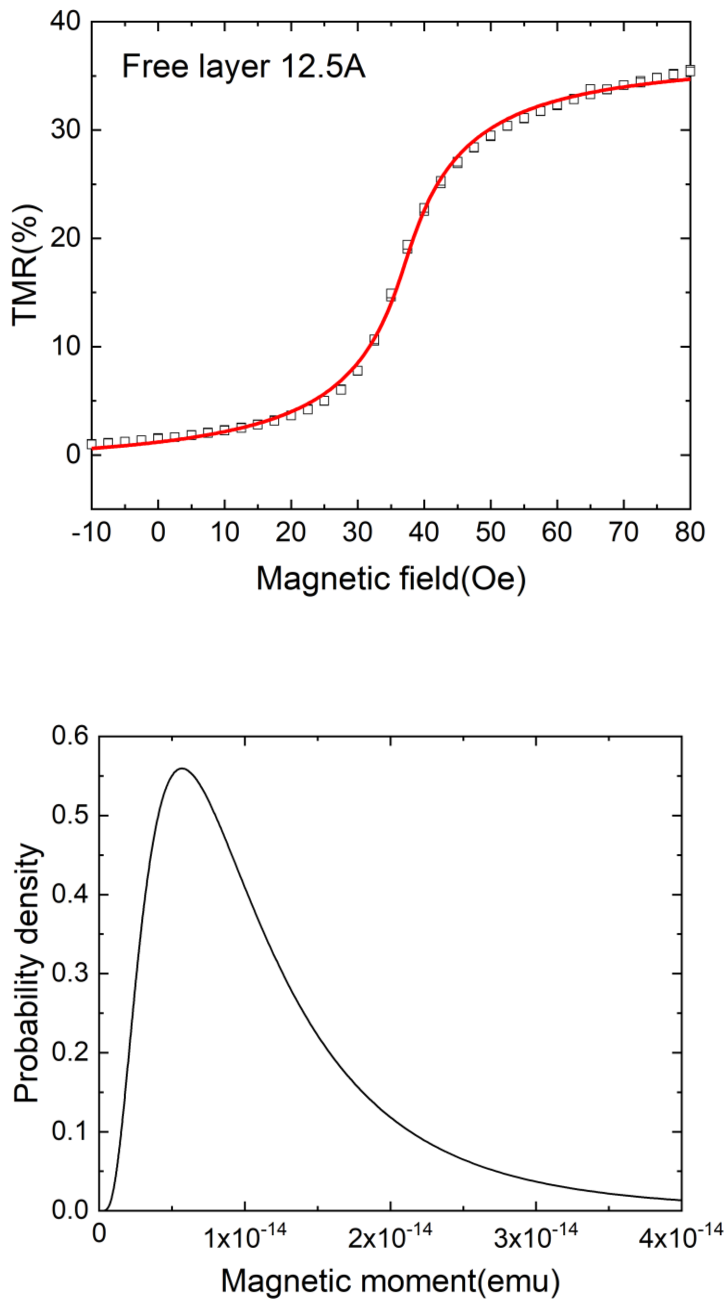

Figure 5. 1 The fitting of an experimental magnetic transfer curve by Langevin equation (top), and the superparamagnetic cluster volume distribution theoretically deduced from this fitting (bottom).

The lognormal distribution obtained by the fitting indicates an average magnetic moment 2.4×10^{-15} emu in the Langevin equation. This distribution also means that what we observe from MTJ is a rather collective behavior of clusters with multiple sizes, and at a certain temperature, only a portion of the clusters are in the superparamagnetic state. Furthermore, the volume of the nanoclusters is computed under the assumption that each nanoparticle is cylindrical with a height of 12.5 A. From the saturation magnetization of CoFeB (1240 emu/cm3), we can estimate the average volume of nanoclusters to be 2.0×10^{-18} cm3, with an effective diameter of 45 nm. These data have clarified necessary details about the superparamagnetic clusters we have in the MTJ free layer, whose sensing properties are going to be tested.

5.2.2 Inducing superparamagnetism using ultrathin films

In our magnetron sputtering chamber used to fabricate MTJ layer stacks, whose working principle is introduced in section 3.2, the layer thickness is different for positions with different radial distances from the center of the substrate, as schematically presented in one of our publications.[105] This is most likely due to the limited uniformity of the Argon plasma generated during sputtering, as the deposition rate decreases for positions away from the plasma center. As a result, the 2 inches diameter silicon substrate we use is rather too big to be fully covered by the plasma, which leads to a non-uniform deposition rate along with the radial distance. To precisely control the free layer thickness for superparamagnetism to appear, such thickness variation must be taken into account.

As shown in Fig 5.2, when the free layer CoFeB in our MTJ gets too thick as 15 angstroms, the superparamagnetic clusters are not formed and a typical ferromagnetic response with around 8 Oe hysteresis is observed. By decreasing the free layer thickness we can see a gradual transition between ferromagnetic to hysteresis-free superparamagnetic responses, which only happens in a narrow thickness change step of 0.5 angstroms. Such a thickness precision usually comes from a sputtering time control of few seconds, so the time cost from all mechanical processes such as the shutter switching, plasma ignition, and so on must be taken into account during a single sputtering operation. When the thickness of CoFeB gets too low, the coherent tunneling for MTJ magnetoresistance disappears leading to a zero TMR ratio. This is because for only a few CoFeB atomic layers at that low thickness, a valid (001) crystalline structure can no longer be assumed, which is essential for coherent tunneling and high MR.

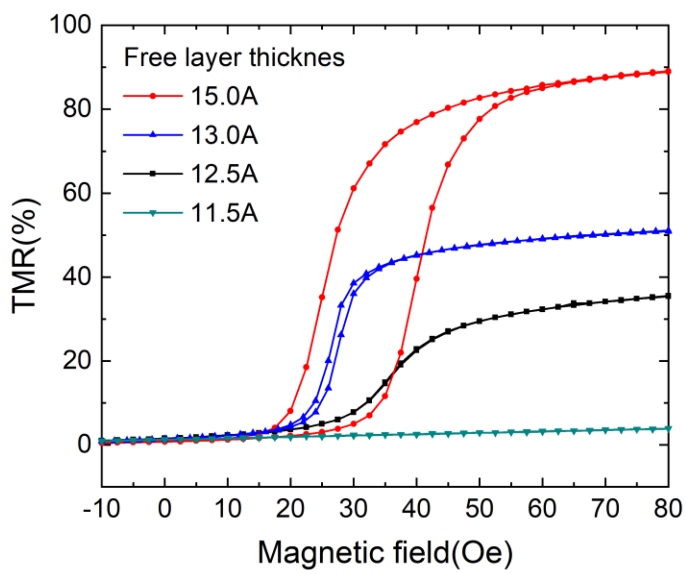

Figure 5. 2 Superparamagnetic MTJ transfer curves in relation with their free layer thickness.

Therefore, the thickness control of the free layer is well designed to be precise within 0.5 angstroms. With this resolution, the superparamagnetic free layer is realized at around 12.5A thickness, while it still holds a decent magnetoresistance ratio.

5.2.3 Field sensitivity and detectability

A detailed transition seen in a collection of transfer curves from ferromagnetic to superparamagnetic MTJ is presented in Fig 5.3.

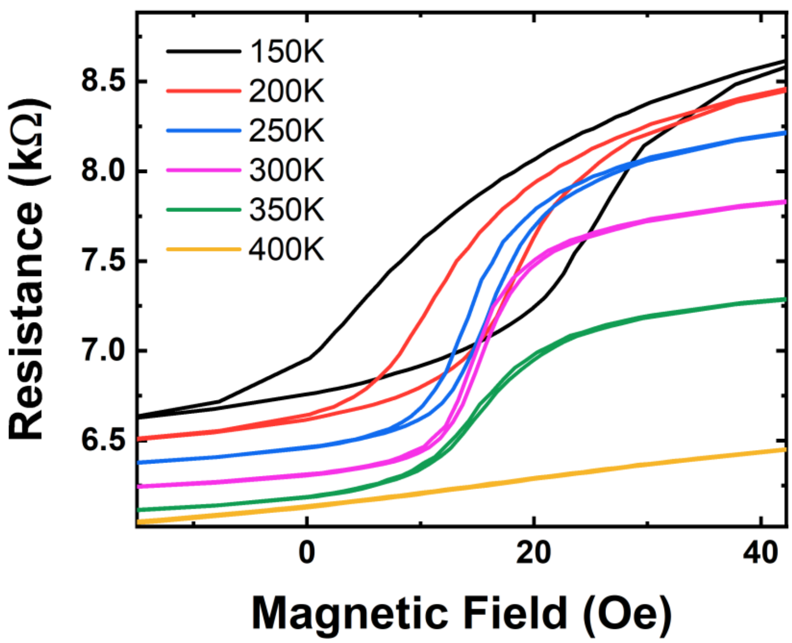

Figure 5. 3 Transfer curves of a superparamagnetic MTJ, measured at different temperatures.

From this figure, we can roughly estimate the superparamagnetic blocking temperature to be around 300K. At temperatures below that, the thermal fluctuation is unable to overcome the magnetic energy, and the sample exhibits a ferromagnetic hysteresis of CoFeB for nearly 20 Oe. Above the superparamagnetic transition, as temperature further increases, the effective magnetization decreases. The loss in the spin polarization leads to a smaller sensitivity and MR. Judging from these transfer curves, it's mostly interesting to study the temperature range from 250K to 350K, where the phase change happens and the MTJ is still responsive to external fields.

The sample is further characterized by our noise measurement system integrated with PPMS. With the sensitivity calculated from the slope of the transfer curve and the noise measured in PPMS, the field detectability can be obtained from the ratio between sensitivity and noise, defined as $S_T\ (T^2/Hz) = \frac{S_V}{V^2S^2}$. S_V is the voltage noise, V the bias voltage, and S the sensitivity. S_T is presented in Fig 5.4[34]:

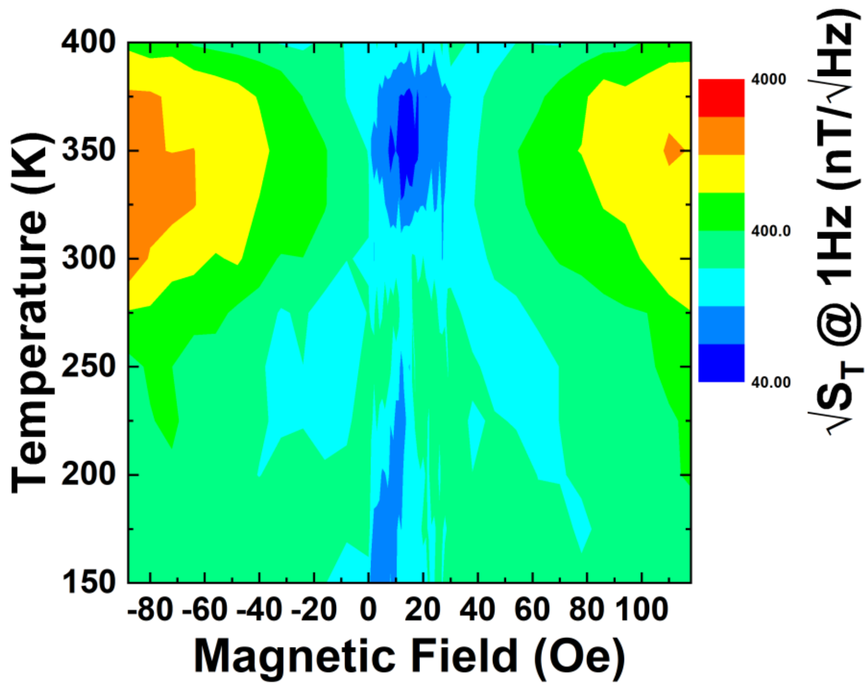

Figure 5. 4 The field detectability map of superparamagnetic MTJ sensors at different measuring temperatures and fields.

We can explain the field detectability distribution in Fig 5.4 in more detail. In the sensitive region away from the saturation, MTJ maintains high sensitivities after it enters the temperature range of superparamagnetic states. It is sensitive until the temperature gets too high for the clusters to exhibit effective magnetization, where the magnetic susceptibility declines. The highest sensitivity calculated from the transfer curve has reached 3%/Oe. The noise preventing this sensor for low field detection is the 1/f magnetic noise at the sensitive field region. Near the superparamagnetic transition, the 1/f noise is lower at high temperatures than that at low temperatures, which implies that the MTJ in the superparamagnetic state has less 1/f noise component. For temperatures higher than 400 K, the electronic 1/f noise becomes larger than the magnetic 1/f noise, giving rise to an additional bias field-independent 1/f noise. Unlike voltage noise and sensitivity, the field detectability as the ratio between them shows a complex temperature dependence. The best field detectability 40 nT/√Hz at 1 Hz is obtained at 350 K, neither corresponding to the peak value of sensitivity at 300 K, nor at 400 K for the smallest noise. It is realized after MTJ has an increased sensitivity by becoming superparamagnetic, but before the noise rises too much due to temperature.

5.2.4 Ferromagnetic to superparamagnetic state transition

The relation between sensitivity and noise is usually directly related to the lowest field detectability, with certain characteristic scaling law. By the application of superparamagnetic phase transition, the MTJ sensitivity has increased by a lot from its ferromagnetic state. In the superparamagnetic state, the magnetic moment is no longer pinned due to the ferromagnetic exchange interaction from adjacent domains. The elimination of ferromagnetic hysteresis enables the moment to rotate freely, more responsively to external magnetic fields. By summarize more results in experiments, we also observed a change in the characteristic scaling law, when the sample undergoes the superparamagnetic phase transition.

At low temperatures, the noise of ferromagnetic MTJs scales quadratic with sensitivity; at higher temperatures, the noise in superparamagnetic MTJs scales linearly with sensitivity, which is superior. Based on the difference in the scaling law between sensitivity and noise, and the knowledge in section 3.2.4, it is likely that after superparamagnetic phase transition, the system has reached thermal equilibrium. In thermal equilibrium systems, the fluctuation-dissipation theorem guarantees a linear scaling law between noise and sensitivity as observed. On the other hand, in a ferromagnetic state, thermal equilibrium is not a valid assumption and a quadratic relation has been observed. Quadratic relation results in poor field detectability since in such relation the field detectability does not improve no matter how sensitivity increases. For the superior linear scaling relation, superparamagnetic transition as a method to reach thermal equilibrium is necessary for general sensing applications.

The transition temperature can be tuned by free layer thickness and annealing temperature, and such tuning of superparamagnetic blocking temperature can facilitate the sensor to operate at room temperature. However, the temperature dependence of the superparamagnetic sensor is another biggest problem, since it is detrimental to the thermal stability of a sensor. For further improvements, the magnetic clusters should be made more uniform with similar sizes. Without the unwanted volume distribution, it can provide us more analyzable and simpler sensing responses instead of complex collective behavior.

5.3 Micromagnetic simulation

5.3.1 Simulation of magnetic vortex state

As the superparamagnetic state turns out to be a well-linearized state in the MTJ free layer, we wonder if there exist other magnetization states that can also achieve such linearization. Vortex magnetization seems to be another potential choice, as introduced by the end of section 3.8.2. Since vortex magnetization has a strong dependence on the geometrical shape of samples as discussed in section 3.8.1, micro-magnetic simulations can be first be used to predict the existence of vortex in the free layer before our actual sample fabrication. The software used for micro-magnetic simulations is MuMax3, which can determine the magnetization pattern by magnetic energy minimization. It can also study the dynamic evolution of magnetization in the time domain under Landau-Lifshitz torque[106].

According to the literature, the vortex spin structure was observed in disks with a thickness of tens of nanometers experimentally. For example, magnetic force microscopy (MFM) was employed to observe a vortex evolution in Permalloy disks of micrometer lateral sizes[107]. Considering these dimensions, we have first performed simulations based on Co-Netic disks of multiple similar geometrical conditions, with lateral dimensions X×Y from 1×1 to 8×8 μm^2, and layer thickness from 400 to 1200 angstrom. As shown in Fig 5.5, the average magnetization in Y direction is plotted in relation to magnetic fields applied in Y direction. The simulation parameters for Co-Netic are the annealing-induced uniaxial anisotropy in the Y direction Ku_1 = 1500 (J/m3), saturation magnetization $M_{sat} = 8.3\times10^5$ (A/m), exchange stiffness $A_{ex} = 10.7\times10^{-12}$ (J/m), and a Landau-Lifshitz damping coefficient 6.4×10^{-3}.

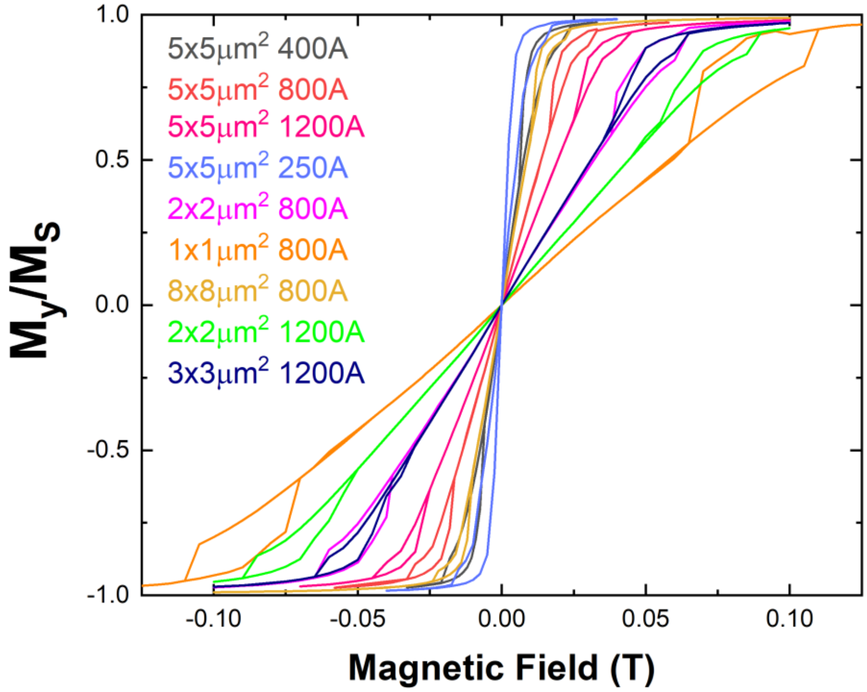

Figure 5. 5 Simulated magnetic transfer curves of Co-Netic disks with vortex magnetization.

These hysteresis loops of reduced magnetization have shown a typical shape due to vortex core displacement, with a linear range and clear nucleation and annihilation points. We can see the vortex topologies in the simulated magnetization textures at each magnetic field, which will be shown later. In the center part of the transfer curve, a linear range with zero coercivity exists and corresponds to the magnetization evolution due to vortex core displacement, which should follow the dynamic equation given in section 3.8.1. The nucleation and annihilation of the vortex correspond to the start and end of such linear range, which lies in different external fields. The nucleation process requires the Zeeman energy due to external fields to become smaller than the demagnetization energy, while the annihilation field needs to be strong enough to push the vortex core to the edge of the samples, where the vortex texture opens up and loses its topological protection. These two processes at their critical fields are accompanied by an abrupt change of resistance because the magnetization pattern dramatically changes instantaneously.

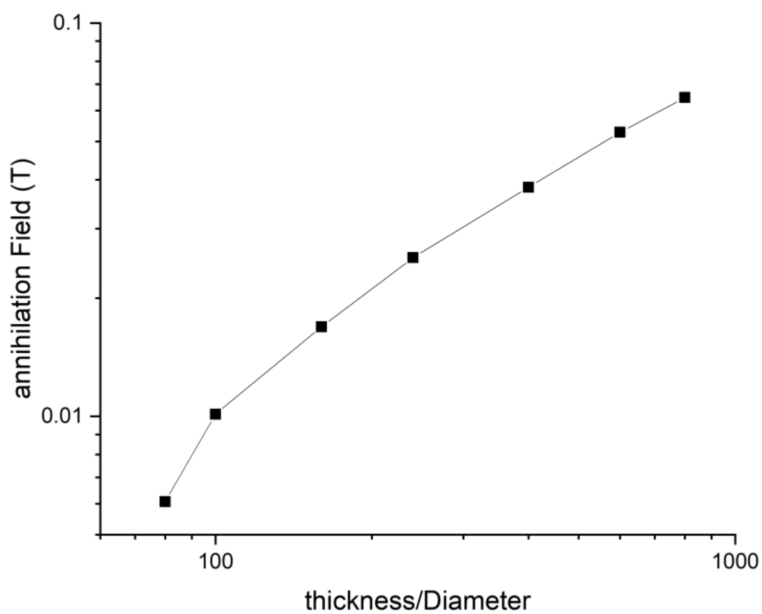

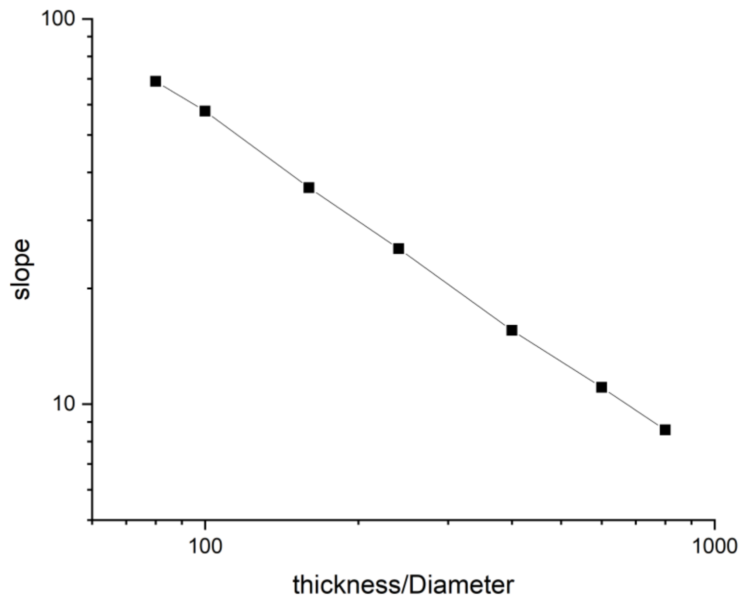

Figure 5. 6 The relation obtained from the transfer curves in Fig 5.5, between line slope, annihilation field and the disk aspect ratio.

Fig 5.6 summarized how the slope of the transfer curve and the annihilation field change with the disk aspect ratio $\beta = t/R$. The nucleation field behaves similarly to the annihilation field. By increasing the disk aspect ratio, the overall transfer curve becomes flat with lower slopes but higher annihilation and nucleation fields. This appears to be a tunable parameter to modify the tradeoff between the sensitivity and dynamic range. It is noteworthy that by simulation we found the vortex nucleation and annihilation fields are around 0.075T and 0.12T, for a "1×1 μm^2, 800A" Co-Netic disk. However, by the theoretical model introduced in section 3.8.1, we can calculate the nucleation and annihilation fields to be 0.11T and 0.69T instead in this case. The real nucleation and annihilation fields differ essentially from simplified theoretical predictions, most probably due to defects or pinning centers in actual structures.

The simulated magnetization can be directly related to the transfer curves that we will obtain in real sample measurements because in MTJ the magnetization dictates its magnetoresistance. From simulated magnetization maps, we obtained the reduced magnetization M_y/M_S along the y direction under external magnetic fields H_y, which is related to the experimental MTJ magnetoconductance by[108]:

$$G = [(G_P + G_{AP}) + (G_P - G_{AP})M_y/M_S]/2$$

where G_P (G_{AP}) is the measured conductance when free-layer magnetization is parallel or antiparallel with respect to the MTJ reference layer.

5.3.2 Experimental realization of vortex MTJ

Given several typical vortex textures we found in simulations, we fabricated MTJs with the CoFeB free layer of corresponding geometrical shapes. The layer stack of MTJ is sequenced as: Si/SiO_2/Ta(50)/Ru(300)/Ta(50)/Ru(20)/IrMn(180)/$Co_{50}Fe_{50}$(30)/Ru(8.5) /$Co_{40}Fe_{40}B_{20}$(30)/$Co_{50}Fe_{50}$(5)/MgO(29)/$Co_{40}Fe_{40}B_{20}$(4)/$Co_{50}Fe_{30}$(5)/$Co_{40}Fe_{40}B_{20}$(600)/Ta(50)/Ru(100), where the numbers in parentheses represent the thickness of each layer in angstrom. We have performed more micromagnetic simulations for CoFeB disks of various shapes, and then experimentally fabricated a few MTJs with free layers in identical shapes. The transfer curves from both simulation and experiment are shown in Fig 5.7.

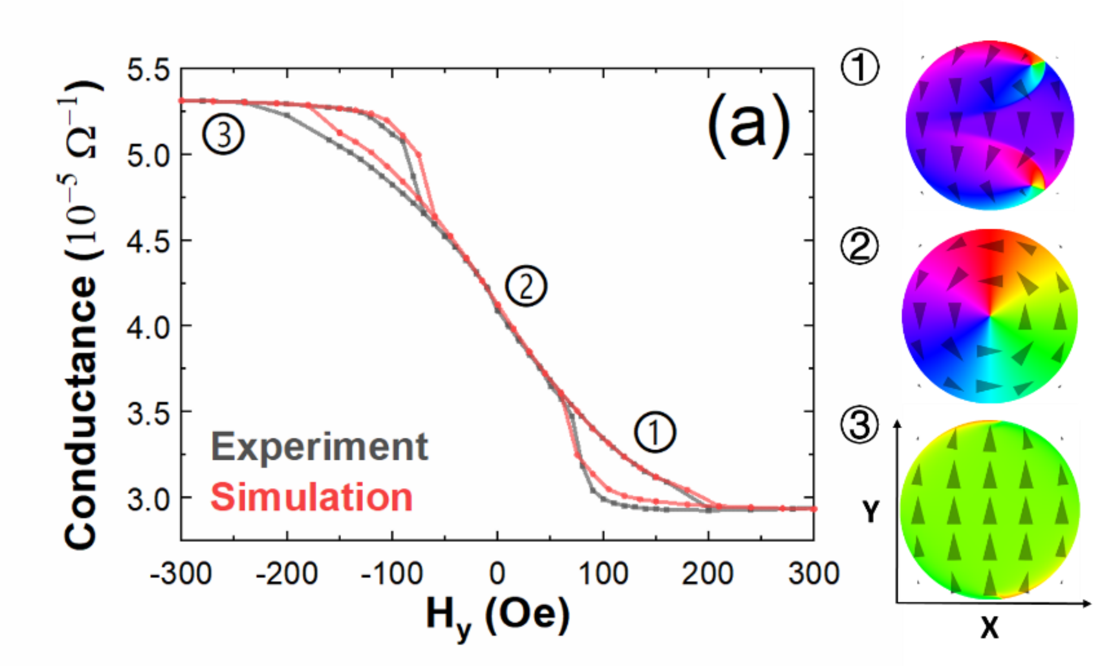

Conductance ($10^{-5}\ \Omega^{-1}$)
5.5
5.0
4.5
4.0
3.5
3.0
-300
-200
-100
0
100
200
300
H_y (Oe)
(a)
③
②
①
Experiment
Simulation
Y
X

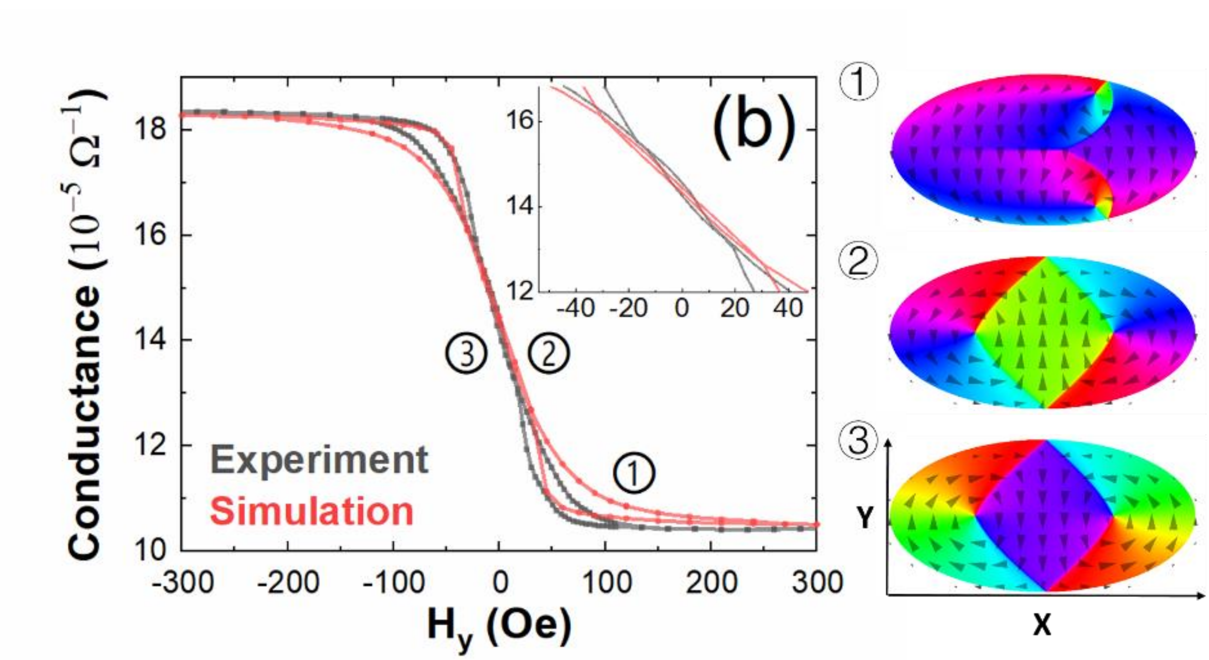

Conductance ($10^{-5}\ \Omega^{-1}$)
18
16
14
12
10
-300
-200
-100
0
100
200
300
H_y (Oe)
(b)
16
14
12
-40
-20
0
20
40
③
②
①
Experiment
Simulation
Y
X

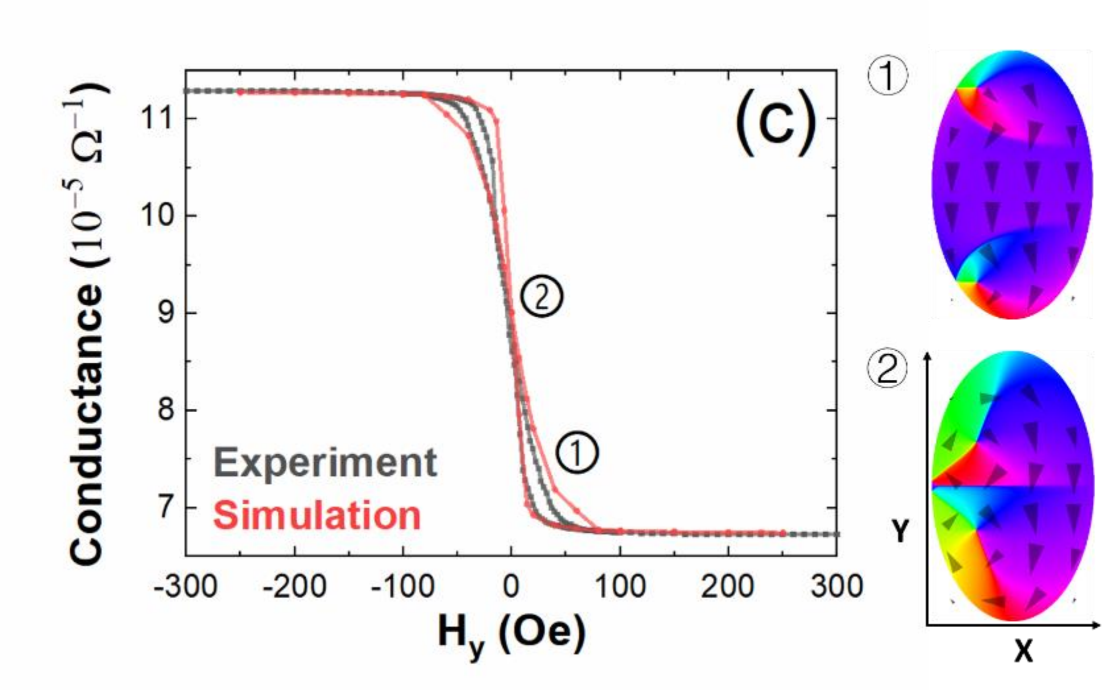

Figure 5. 7 Experimental and simulated transfer curve for a single vortex, double vortices, and anti-vortex states. On the right of each diagram are the magnetization patterns corresponding to the labeled positions.

The consistency between the simulation and experimental transfer curves convinces us that the simulated vortex textures are achieved in the MTJ free layer. On the right side of the diagram, three spin textures show the simulated magnetization at different positions of the transfer curve. These transfer curves are obtained respectively for three vortex textures found for different free layer geometries, and we can define them as a single vortex, double vortices, and anti-vortex state. Their critical fields and magnetic textures are different from each other, even though they undergo a similar process along the transfer curve.

In Fig. 5.7 (a), the free layer has a geometry of X = 5 µm, Y = 5 µm, and layer thickness $t = 500A$. With this aspect ratio X /Y to be around 1, the single vortex state is obtained for being energetically favorable. Initially, under a saturation magnetic field, the single vortex is not formed, and the spin texture is a uniform magnetization in the Y direction due to fields above 200 Oe. As the external magnetic field decrease below 200 Oe, a buckling state is first formed, as a preliminary state before vortex nucleation at position 1, labeled on the transfer curve. When the field drops below 75 Oe, the buckling state is passed and a single vortex is formed, with its magnetic flux in an enclosed pattern. The core position of the vortex will be shifted by the external fields in the X direction. Such vortex core displacement is reversible and provides a linear response in the transfer curve at position 2. As the field reaches above -200 Oe, the vortex core opens up since it has already touched the sample edge. In the end, it aligns to the large external magnetic field with a uniform magnetization at position 3. During this process, every time a configurational transition happens where the spin texture changes dramatically, an abrupt change can be seen in the MTJ susceptibility. In the vortex core displacement field range, the vortex is topologically protected. The vortex core evolves under a large range of external magnetic fields in a reversible manner, which is thus free of hysteresis.

The nucleation, displacement and annihilation process also applies to the double spin texture, as shown in Fig 5.7(b). It is formed for X = 14 μm, Y = 7 μm, and layer thickness $t = 500A$. With an aspect ratio X /Y > 1, two vortices could co-exist in an oval-shaped MTJ. In the oval free layer, in the central region, the magnetization aligns with the external magnetic field to minimize the Zeeman energy, while vortex spin texture is formed symmetrically on both ends near the sample edge, where strong demagnetizing fields exist. Two vortices core move in opposite directions under external fields, so that more spins in the central region align parallel to the fields. On the other hand, the chirality of two vortices is the opposite, thus the overall vorticity can be changed if we interchange the positions of two vortices.

Therefore, such a magnetization topology has two possible configurations as discussed previously in section 3.8.2, as indicated by spin texture maps 2 and 3. As a result, a hysteresis of 2 Oe is observed due to the existence of two possible spin configurations with different vorticity.

When the aspect ratio X /Y < 1, an ant-vortex will be formed. Fig 5.7(c) shows such a result with X = 6 μm, Y = 10 μm, layer thickness $t = 500A$. Two vortices and an anti-vortex are contained in such an anti-vortex state. The difference is that the two vortices have the same chirality. Therefore unlike the double vortices state, the interchange of their positions doesn't change the topological charges. This is preferable since no hysteresis will be generated, but this anti-vortex state is formed only at a very narrow field range. For most of the field range, the magnetization is stuck in the buckling state, leading to a small dynamic range of only 20 Oe.

After a complete analysis of the transfer curves of these three vortex topologies, the single vortex state and the anti-vortex state are found to be hysteresis free during its vortex core displacement. Meanwhile, the anti-vortex state has a narrow dynamic range which is unfavorable. Therefore, we are going to explore the vortex MTJs sensor with only a single vortex core inside, to make a desired linear sensor.

Fig 5.8 gives a summarized vortex phase diagram, in the two-dimensional space of the sample geometrical shape. For an oval MTJ free layer with lateral size X × Y and thickness of 400A, three vortex states have their distinctive regions. The single vortex state in the white region is what we desired, and such a phase diagram completes its fabrication recipe.

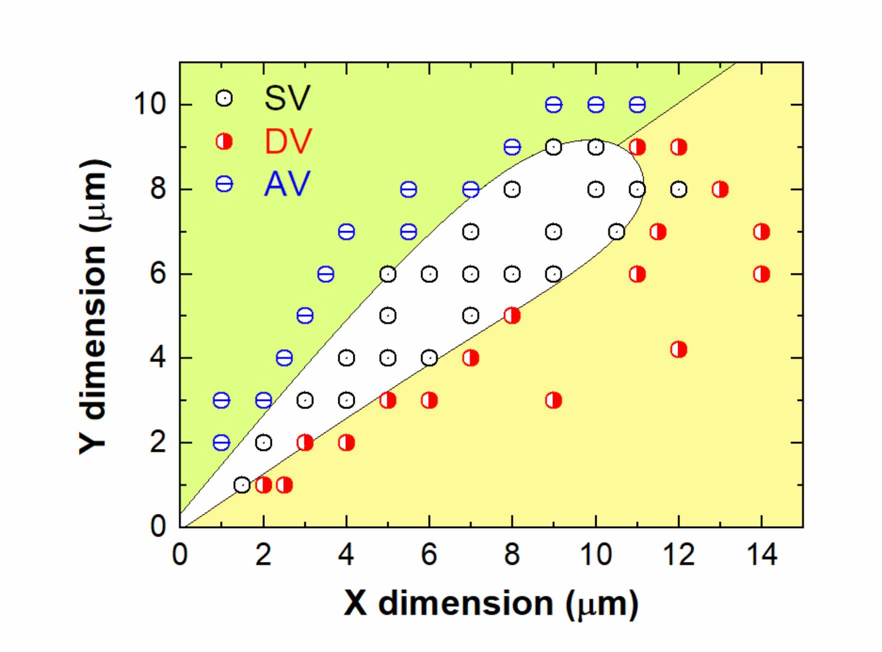

Figure 5. 8 The generation of three kinds of vortex states in MTJs is related to different X-Y lateral dimensions; the magnetic field during annealing and measurement is applied along the Y-direction. SV is short for single vortex, DV for double vortices, and AV for anti-vortex.

5.4 Vortex MTJ array sensor

5.4.1 Noise reduction in array sensors

For magnetic field detection using MTJ, the most imperative task is to deal with the 1/f noise, which sets the limit for the lowest detectable field. As introduced in section 3.2.3, it can be expressed by $S_v^{flicker} = \alpha V^2/Af^{\gamma}$ where A is the tunneling junction area. Instead of using a single MTJ, by connecting MTJs in series or parallel, we can increase the effective junction area, and thus the low-frequency 1/f noise is reduced. If the total number of sensors connected in series or parallel is N, the noise should scale as $1/\sqrt{N}$ theoretically[109]. To maintain a small spatial resolution, we keep the overall area of one sensing unit is 0.5×0.5 mm^2, within which MTJ circular elements with a diameter of 5 μm are patterned into a compact array. The free-layer thickness is increased to t = 600A so that we can surely obtain a single vortex magnetization. Each sensing unit has $48 \times 32 = 1536$ MTJ elements, where 48 MTJs is connected in series as one row, and there are 32 such rows connected in parallel. Figure 5.9 is taken under a microscope for the total array, where circular MTJ elements can be roughly seen in the magnified view. On both sides are four contact pads used for wire bonding connection to external circuitry.

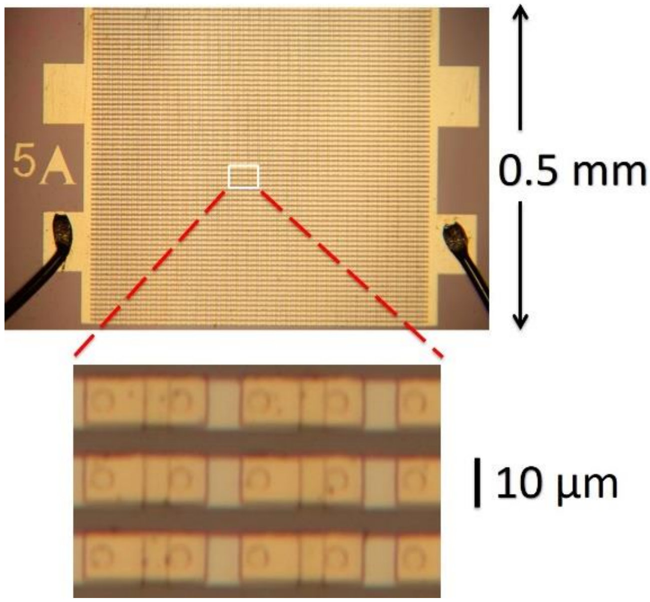

Figure 5. 9 The micrograph of the MTJ array sensor, with an enlarged view of many circular MTJ elements.

Another merit of the vortex state is its nature of magnetic flux enclosure. The magnetic coupling between adjacent MTJ elements is ultimately suppressed since each element possesses no stray field. We choose a very dense nearest-neighbor separation of 15 μm, to fully take advantage of it.

5.4.2 Sensor characterization

The single vortex MTJ array demonstrated above is measured by the noise measurement system and PPMS introduced in chapter 2.3. Temperature-dependent transport and noise measurements are shown in Fig 5.10, where four diagrams respectively for the transfer curves, sensitivities, noise and detectability are given together to better show their comparison. The sensor is thoroughly characterized this way, and is going to be used in the application of magnetic gradiometers in chapter 7.

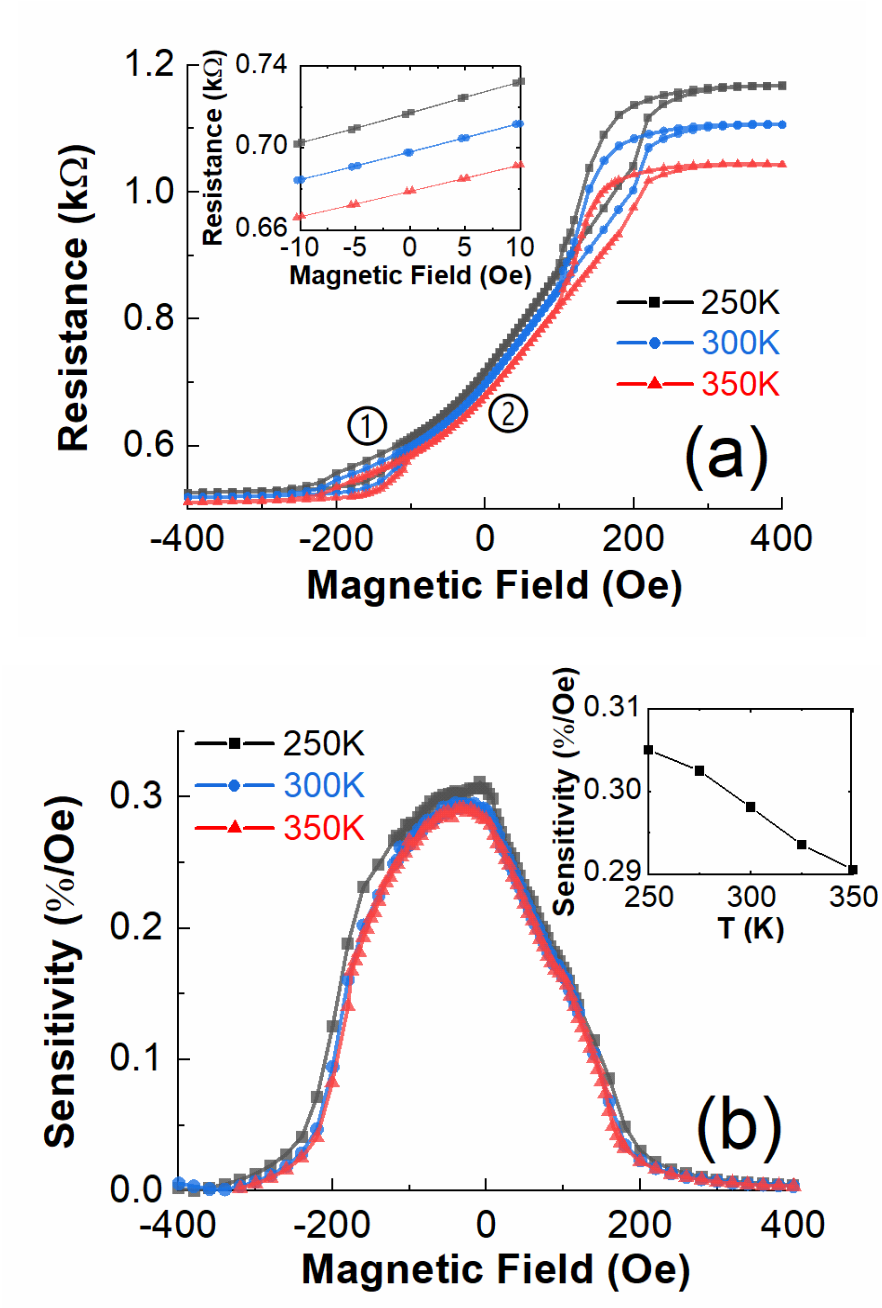

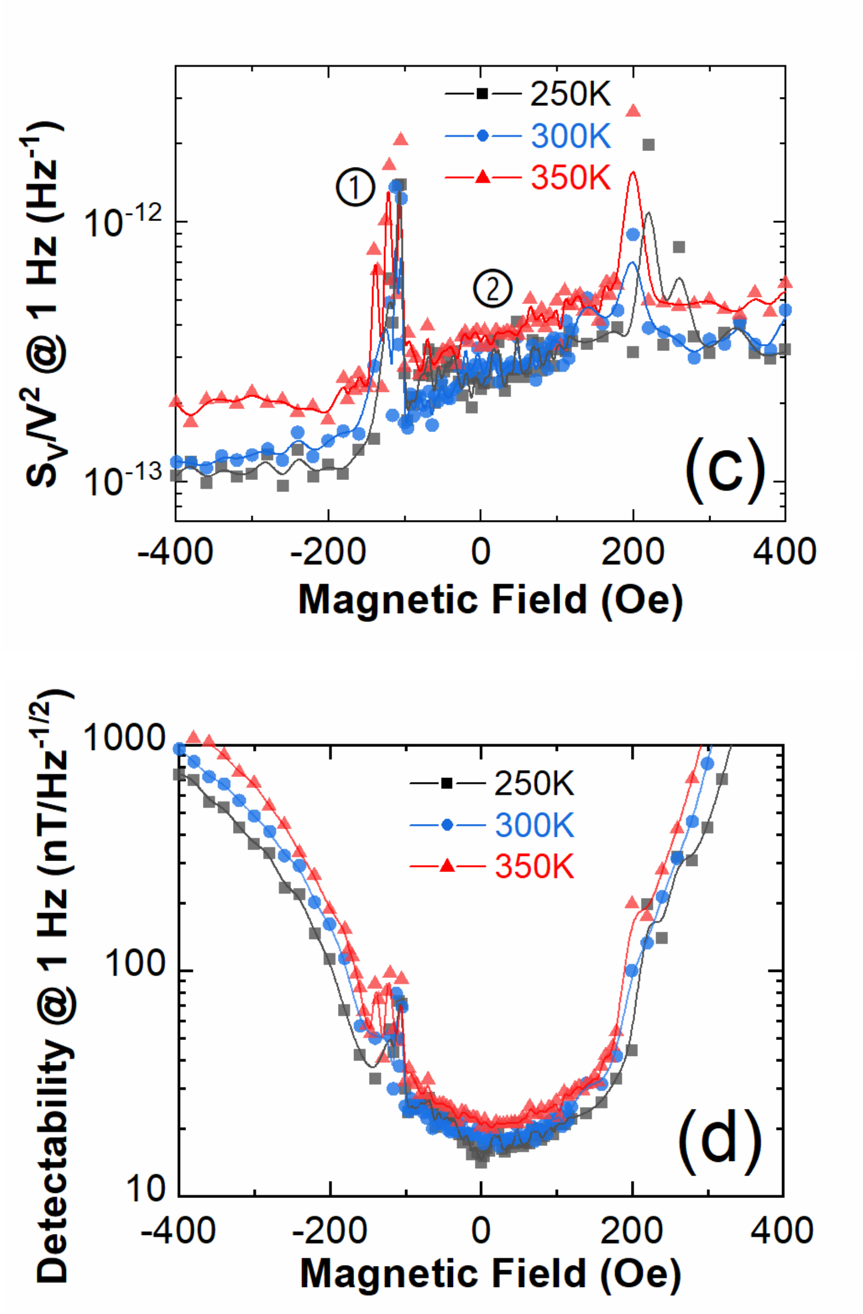

Figure 5. 10 Four diagrams from top to bottom respectively show the transfer curves, sensitivities, noise and detectability for the single-vortex MTJ sensor array, at three temperatures.

From the transfer curves shown in Fig 5.10(a), in a large range of temperature from 250 to 350 K, we can observe a clear single vortex behavior, with a central non-hysteretic response. The inset of Fig 5.10(a) further enlarged this linear range for details. In Fig 5.10(b), the sensitivity preserves its peak value of 0.3%/Oe within a dynamic range of 100 Oe. The sensitivity of vortex MTJ depends on the ratio between the free-layer thickness and diameter as discussed in section 6.3.1, and our sensor with a small such ratio shows a comparatively high sensitivity of 0.3%/Oe, while in literature it is usually lower[110]. Speaking of thermal stability, the sensitivity drops by 12% in a 100 Oe range. Fig 5.10(b) also provides an inset showing how the peak sensitivity changes with temperature, with a temperature coefficient of only 400 ppm/K. The sensor noise is given in Fig 5.10(c), which is mainly magnetic originated. Vortex magnetization holds high stability and thus comparatively low normalized noise of 10^{-13} Hz^{-1}. As a typical noise index, the Hooge-like parameter α is calculated to be below 10^{-9} μm^2, while several abnormal peaks exist in the nucleation or annihilation process of the vortex core. We mark such an unusual noise peak label "1" with its appearance in Fig 5.10(c). As the most important parameter, the field detectability of this sensor is obtained from the ratio between sensitivity and noise, given in Fig 5.10(d) in a field range of ±400 Oe, by three measurements with a temperature span from 250 to 350 K. The detectability is calculated as low as 18 nT/√Hz at 1 Hz which is also stable in a large range.

An important sensor parameter is the dynamic reserve, which is the ratio between its dynamic field range and the smallest detectable field. For this sensor, considering a 1 Hz bandwidth for typical data acquisition devices, a high dynamic reserve of 115 dB can be estimated. In conclusion, the vortex MTJ has its merits in the hysteresis free magnetic response, giving large dynamic ranges and good field detectability.

5.4.3 Noise scaling law

As mentioned in section 5.4.2, there exist several abnormal peaks indicated by label "1" in Fig 5.10(c), which will be studied in detail by the corresponding noise spectrum. Along the vortex MTJ transfer curve, we extracted the spectrum in both the region of vortex nucleation corresponding to position 1 in Fig 5.10(a), to compare with the spectrum in the core displacement, which is identified at position 2 in Fig 5.10(a). Two spectrums are put together in Fig 5.11(a).

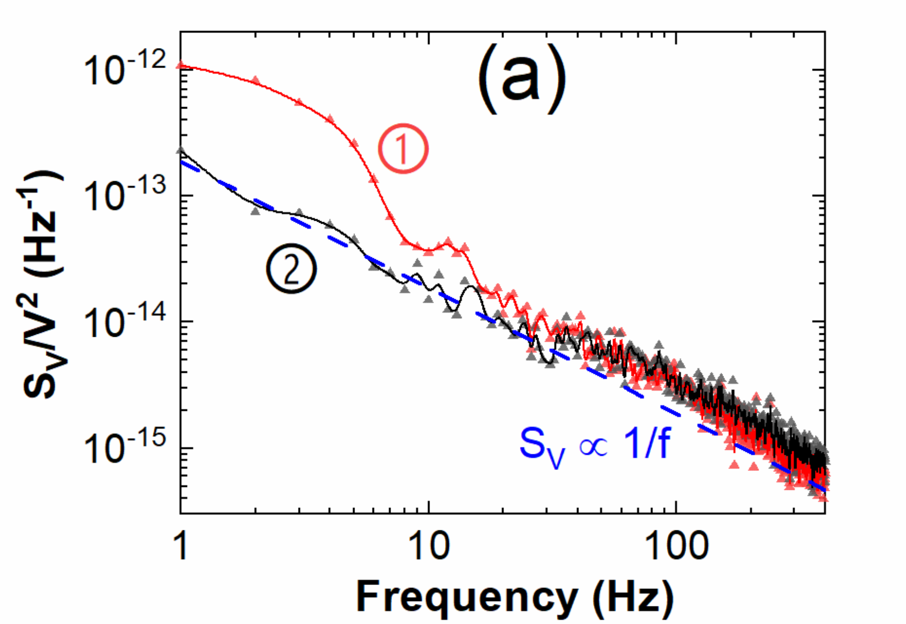

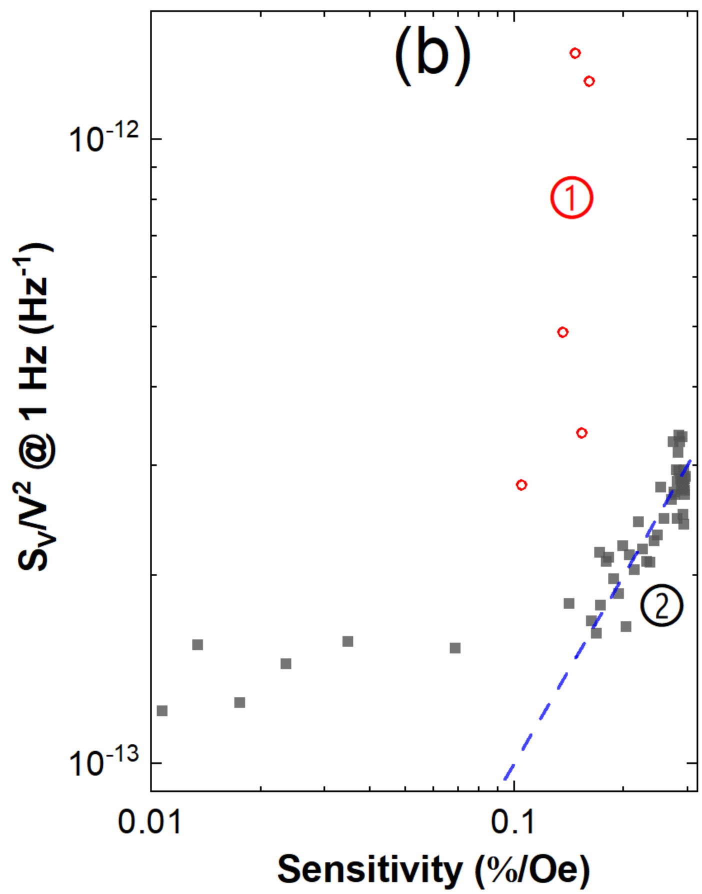

Figure 5. 11 (a) Two noise spectra measured at positions 1 and 2 of the transfer curve in Fig. 5.10(a). (b) The noise-sensitivity scaling law extracted from the measurements at 300K in Fig. 5.10.

Fig 5.11 is obtained by extracting the 300K data shown in Fig 5.10. In figure (a), the dashed line indicates the 1/f noise. In figure (b), the data points of antiparallel magnetization orientation in MTJ are ignored, which include the extra noise from the reference layer[111]; the dashed line is a linear scaling law. A normal noise following the 1/f trend is observed in the linear response region after the vortex nucleation. Before that at the beginning region of vortex nucleation, a bump coming from a Lorentzian type of noise is observed, whose roll-off frequency is around a few Hertz. The origin of this Lorentzian bump can be attributed to the magnetization hopping in the MTJ free layer, and the low roll-off frequency indicates large activation energies[112]. In the buckling state, it's very likely that magnetic large magnetic domains during vortex nucleation are frequently hopping, leading to abnormal noise behavior.

The scaling relation between noise and sensitivity in Fig 5.11 can be related to the theoretical background in section 3.2.4. From the FD theorem, the noise spectrum of the MTJ is supposed to retain a linear relation with sensitivity. In the region of high sensitivity above 0.1%/Oe, such a linear scaling is demonstrated, since data points can conform to a linear dashed line. We can conclude that in the highly sensitive region where magnetic 1/f noise dominates, the sensitivity-noise scaling is well predicted by the FD theorem. However, it is not the case for the vortex nucleation region, where a large amount of extra noise is found. Since the FD theorem is based on a quasi-equilibrium assumption[59], this unconformity is an indication that the vortex magnetization configuration change is a non-equilibrium phase transition process. Sensors operating in a non-equilibrium state should thus be avoided in any case.

Chapter 6 Tunable Magnetic Anisotropy

6.1 Introduction

This chapter will discuss the introduction of interfacial perpendicular magnetic anisotropy (PMA) into MTJ to modify the overall sensing properties. As introduced theoretically in section 3.9.2, the control of PMA strength is rewarding, such as the voltage-controlled magnetic anisotropy. We will thoroughly study the factors related to magnetic anisotropy in our MTJ system, such as the shape, annealing condition, layer composite, and the measurement temperature. With a controllable PMA strength, we can analyze the relation between sensitivity and magnetic anisotropy, to reveal the highest sensitivity achieved in a scheme of compensated magnetic anisotropy. Meanwhile, an interesting random telegraph noise (RTN) found in this layer stack is reported. Such noise has its origin in the generation-recombination process and its potential application in random number generators.

6.2 Interfacial PMA in MTJ

6.2.1 PMA generation in MTJ fabrication

Following relevant literature,[88,113] we introduced a modified MTJ layer structure which effectively induces PMA in the free layer, sequenced as: Si/SiO2/Ta(50)/Ru(150)/Ta(100)/MgO(16)/Co40Fe40B20(9)/W(t_1)/Co40Fe40B20(t_2)/MgO(27)/Co40Fe40B20(30)/Ru(8.5)/Co50Fe50(30)/Ir22Mn78(180)/Ru(100)/Ta(100), where the numbers in parentheses represent the thickness of each layer in angstrom. The magnetization of the reference layer is pinned in the thin-film plane by IrMn, on top of the MgO barrier, and a coupled free layer stack beneath the MgO layer is comprised of MgO(16)/ Co40Fe40B20(9)/W(t_1)/Co40Fe40B20(t_2). t_1 and t_2 are two-layer thicknesses, and PMA is present at both MgO/CoFeB interfaces. The magnetization of two CoFeB layers is coupled through a W spacer. As introduced in chapter 2, the complete stack is deposited by magnetron sputtering with a base pressure of 2×10^{-8} torr. Standard photolithography and physical ion milling are used to define MTJ elements, into an oval shape of lateral size $7x10.5\mu m^2$. Post growth thermal annealing is performed in vacuum condition at T_a for 1 h, under a magnetic field of 0.5 T along the long-axis direction of the MTJ oval. In our usual magneto-transport measurements, eight identical MTJs are connected in series as a sensor unit, exposed to a uniform magnetic field in the short-axis direction of each MTJ oval in the Quantum Design® Physical Property Measurement System (PPMS). The MTJ sensor is empowered by batteries, connected in series with a voltage divider resistor. Its voltage signal is first amplified by electronics on a printed circuit board it is wire-bonded to, and then read by data acquisition devices outside the PPMS. The practical sensitivity is obtained by applying a modulating field (δH = 0.3Oe) at 5Hz to the sensor and measuring its voltage signal response.

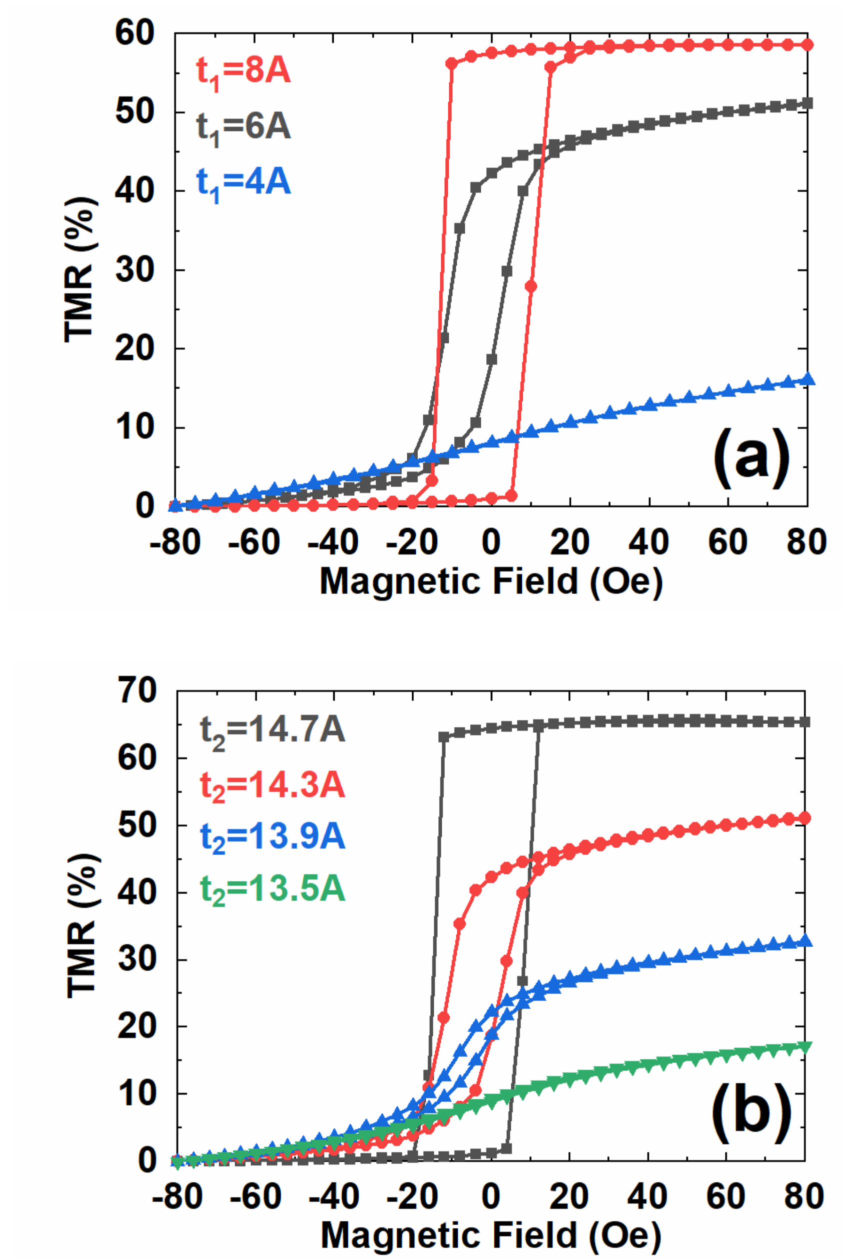

t1=8A
t1=6A
t1=4A
TMR (%)
Magnetic Field (Oe)
(a)
t2=14.7A
t2=14.3A
t2=13.9A
t2=13.5A
TMR (%)
Magnetic Field (Oe)
(b)

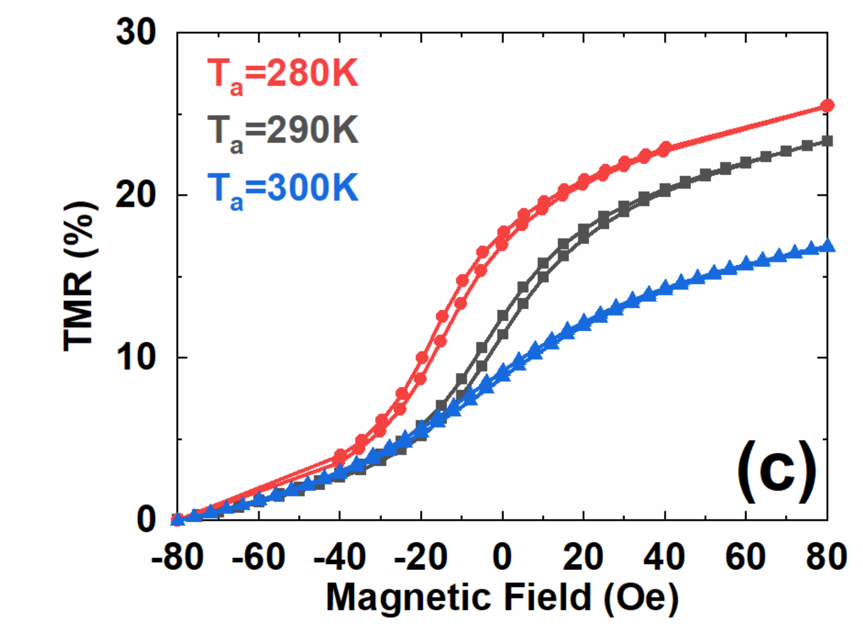

Figure 6. 1 The TMR transfer curves of MTJs with composite free layer MgO(16)/ $Co_{40}Fe_{40}B_{20}$(9)/W(t_1)/$Co_{40}Fe_{40}B_{20}$(t_2), where (a) W spacer thicknesses t_1, (b) CoFeB thickness t_2 or (c) annealing temperature T_a are changed.

All the transfer curves in Fig 6.1 is measured at room temperature by applying external magnetic fields in the in-plane direction. The PMA induced in the free layer acts as a hard axis bias field, to first align the magnetization in the out-of-plane direction. Therefore, the magnetization responds to the in-plane magnetic field linearly with small coercive force, whose original hysteresis loop appears as a square loop due to the in-plane shape anisotropy. The transformation from a square shape to linear shape is an indication of PMA gradually dominating the overall magnetic anisotropy.

For all diagrams in Fig 6.1, the MTJ shape is a 7x10.5 μm^2 oval, and the annealing is done with a magnetic field applied in the long axis. For the top figure, the CoFeB thickness t_2 = 14.3 A, and the annealing temperature T_a is 300℃. Different transfer curves are measured for different W spacer layer thickness t_1. For the middle figure, t_2 is varied with t_1 = 6A, and T_a is 300℃. For the bottom figure, the thickness t_1 = 6 A, t_2 = 13.5 A, and T_a is varied. The trend observed in the three diagrams is that the PMA strength is decreasing when W spacer thickness increases from 4 A to 8 A; it is enhanced for increasing temperature from 280 to 300 ℃. The overall magnetic anisotropy is described in section 3.9.1, and thus the decrease in the free layer thickness leads to a more linear transfer curve. The impact on PMA strength from the W layer thickness is explained by the change in the Ruderman–Kittel–Kasuya–Yosida (RKKY). The increment in spacer thickness t_2 could impair the RKKY coupling between two CoFeB layers,[114] so that PMA in the layer adjacent to MgO becomes weak leading to such a trend.

6.2.2 Spin-torque switching and PMA

The development of magnetic random-access memory (MRAM) is strongly dependent on the use of spin-transfer torque (STT), which can manipulate the magnetization of adjacent layers through spin-polarized current. Also, recent works have shown that the switching speed of STT can be enhanced by tuning the magnetic anisotropy. By inducing PMA into MTJ free layer, a non-collinear relation can be introduced between the magnetization orientations of the free layer and the pinned layer. Such PMA can be tuned by several parameters such as the free layer thickness, to present a canted magnetic anisotropy, in-plane anisotropy, or perpendicular anisotropy dominant situations. As a result, the magnetization-reversal switching speed can be modified and enhanced, which directly bring down the energy cost of each MRAM read/write operations.[84] In actual MRAM devices, the thermal stability needs to be as high as possible so that the device can be non-volatile. In this sense, the thermal stability factor defined as $\Delta = E/k_B T$ should be guaranteed by a large PMA, where E is the energy barrier between the two magnetization configurations subject to PMA strength K_u. On the other hand, it is desired to switch between these two configurations with the least amount of current I_{sw}, for energy efficiency. The quantity Δ / I_{sw} is thus the most representative index for an MRAM device. The switching current is negatively correlated to the PMA strength in perpendicular MTJ junctions, while the detailed relation is worth study to find the most efficient working condition.

In this section, we used MUMAX3 micromagnetic simulation to study the relation between PMA and the current of magnetization switching. The MTJ free layer has a PMA energy density of K_u, so that all the magnetic moments are initially in the out-of-plane direction (positive direction of y-axis). A current is injected into such layer from below, with its spin fully polarized in the -y direction opposite to the initial magnetization direction of the free layer. In this configuration, the reduced magnetization in y-axis M_y/M_S of the free layer is evolved under the Landau–Lifshitz–Gilbert (LLG) equation in the simulations. Fig 6.2 shows the evolution of M_y/M_S under different conditions.

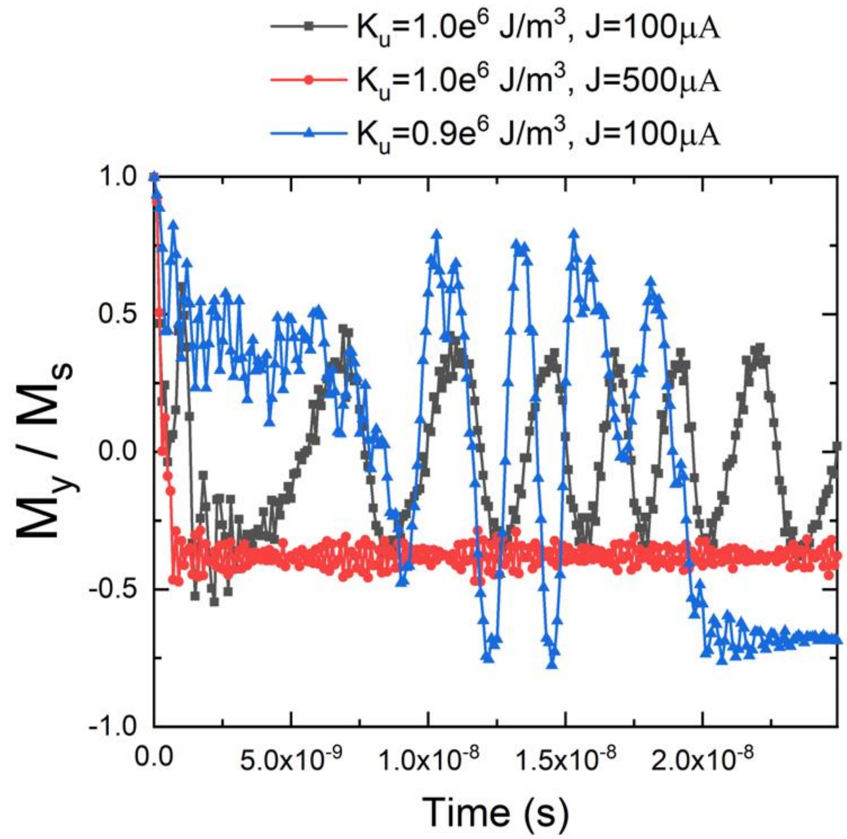

Figure 6. 2 The evolution of reduced magnetization in the MTJ free layer under different STT currents J and PMA strength K_u. After the current is applied at time t=0, M_y either oscillates or switches to the opposite direction.

In Fig 6.2 we can see that for the red curve, the magnetization switches immediately after only one ns, to the direction of the spin polarization of the current. When the switching current decreases from 500 to 100 microampere, the magnetization cannot be switched, but rather oscillates between two intermediate procession states, as shown by the black curve. By reducing the magnetic anisotropy K_u in the free layer, the blue curve shows that the magnetization switching takes place again, but for a longer time of 20 ns and still with some oscillation behavior during the switching.

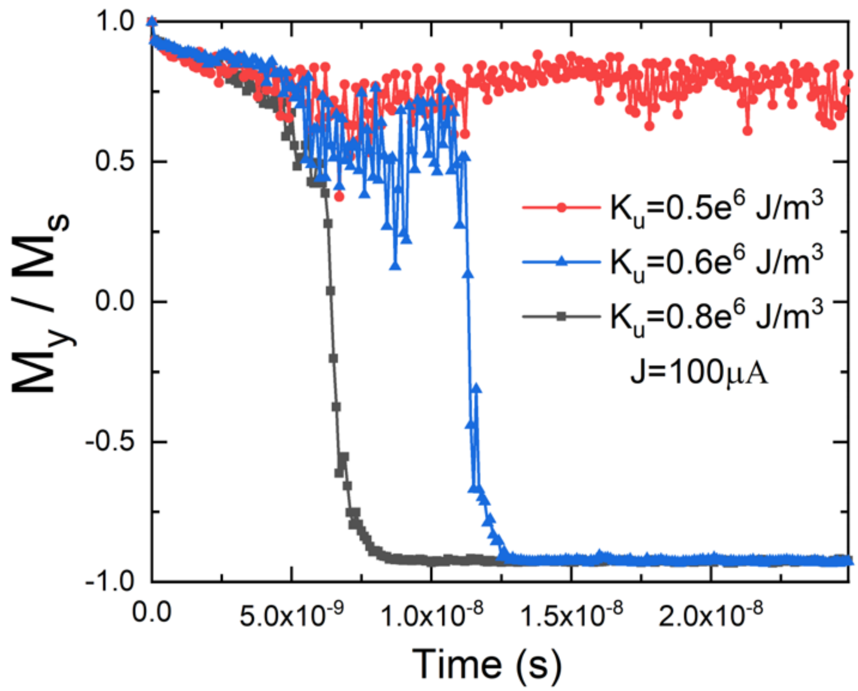

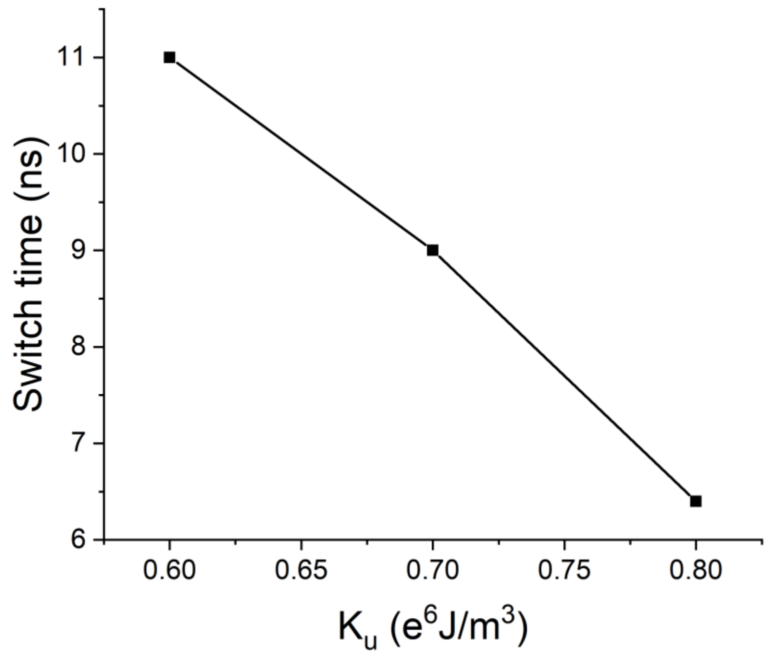

Figure 6. 3 In the top figure, the magnetization in the MTJ free layer of different PMA Ku switches its orientation due to an STT current J, after a switching process time. The relation between the PMA strength and the switching time is shown at the bottom.

In Fig 6.3 we have summarized results for similar simulations under different PMA strength K_u. We can see that by tuning the PMA in the thin-film free layer against the in-plane shape anisotropy, the magnetic switching event can take place much faster, indicating a boosted switching speed. Besides this switching time, we also studied the minimum current needed for the switching event to happen, corresponding to the purple curve in Fig 6.4, as shown below.

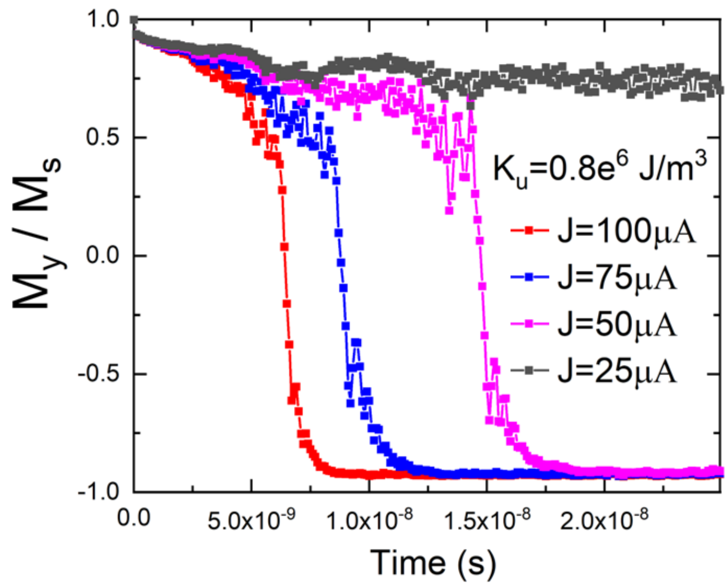

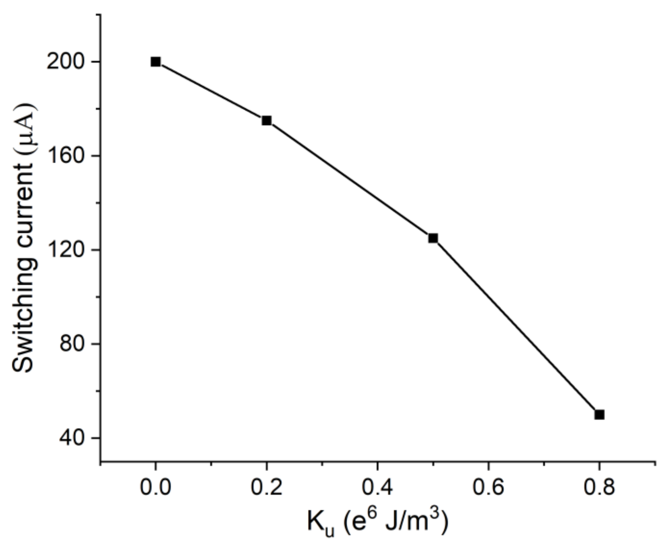

Figure 6. 4 The switching process similar to Fig 6.3 is shown, where a minimum switching current J = 50 μA is found for the PMA $K_u = 0.8\times10^6$ J/m^3. A summarized relation between other PMA values and their minimum switching current is shown at the bottom.

Fig 6.4 showed that by PMA strength tuning, we can as well control the required current to fulfill a magnetic switching event. Bring down such magnetic switching current can help to reduce the energy cost of MRAM devices, particularly in its writing operation. The effectiveness of this method remains to be experimentally confirmed.

6.2.3 MTJ sensitivity and PMA

As a map of the MTJ sensitivity at different bias magnetic fields has presented featured sensitivity peaks,[80,115] it is intriguing to know a featured map for different PMA strength as well. But in common literature, the sensitivity is merely related to magnetic anisotropy through its rough value from the transfer curve.[89,116] Unless the sensor is hysteresis-free, the sensitivity overestimated this way could deviate a lot from the practical value in low-field measurements.[101] Thus, we intend to study the impact of anisotropy on practical sensitivities more precisely to provide guidance for designing magnetic sensors in real applications. In addition, recent studies on anomalous Hall sensors imply that by a magnetic anisotropy compensation, the sensor can have enhanced sensitivities.[117,118] In this section, a similar mechanism will be revealed by tuning PMA in MTJ.

Due to the temperature dependence of PMA,[119] it is more convenient to study its impact on the sensing performance by varying the measurement temperature. The MTJ sensor with t_1 = 6A, t_2 = 13.9A, T_a=300K is cooled down and measured inside PPMS from 400K to 140K, the transfer curves are observed to become more flat with lower MR. Such an effect is due to the increase in PMA strength, which aligns more magnetization in the out-of-plane direction. The results are plotted in Fig 6.5(a).

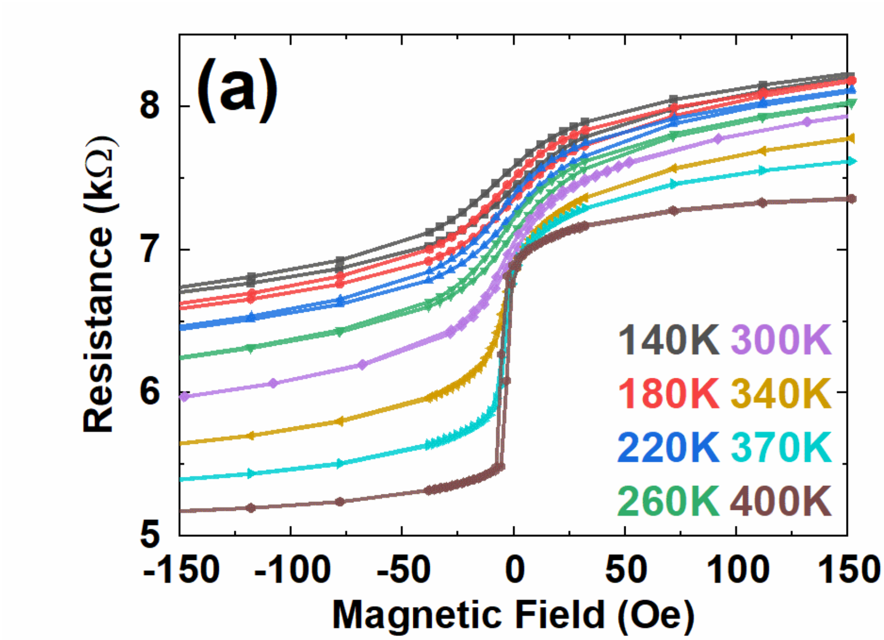

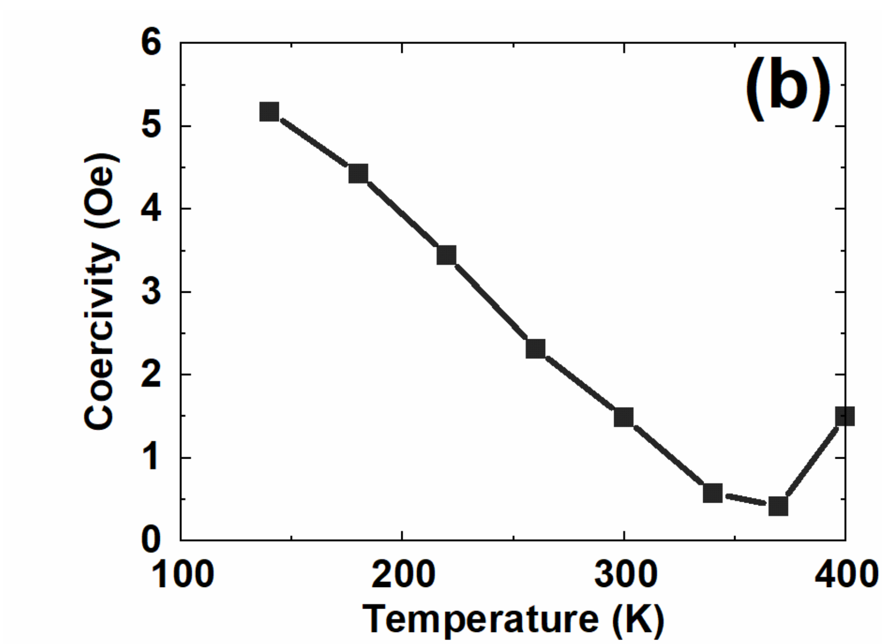

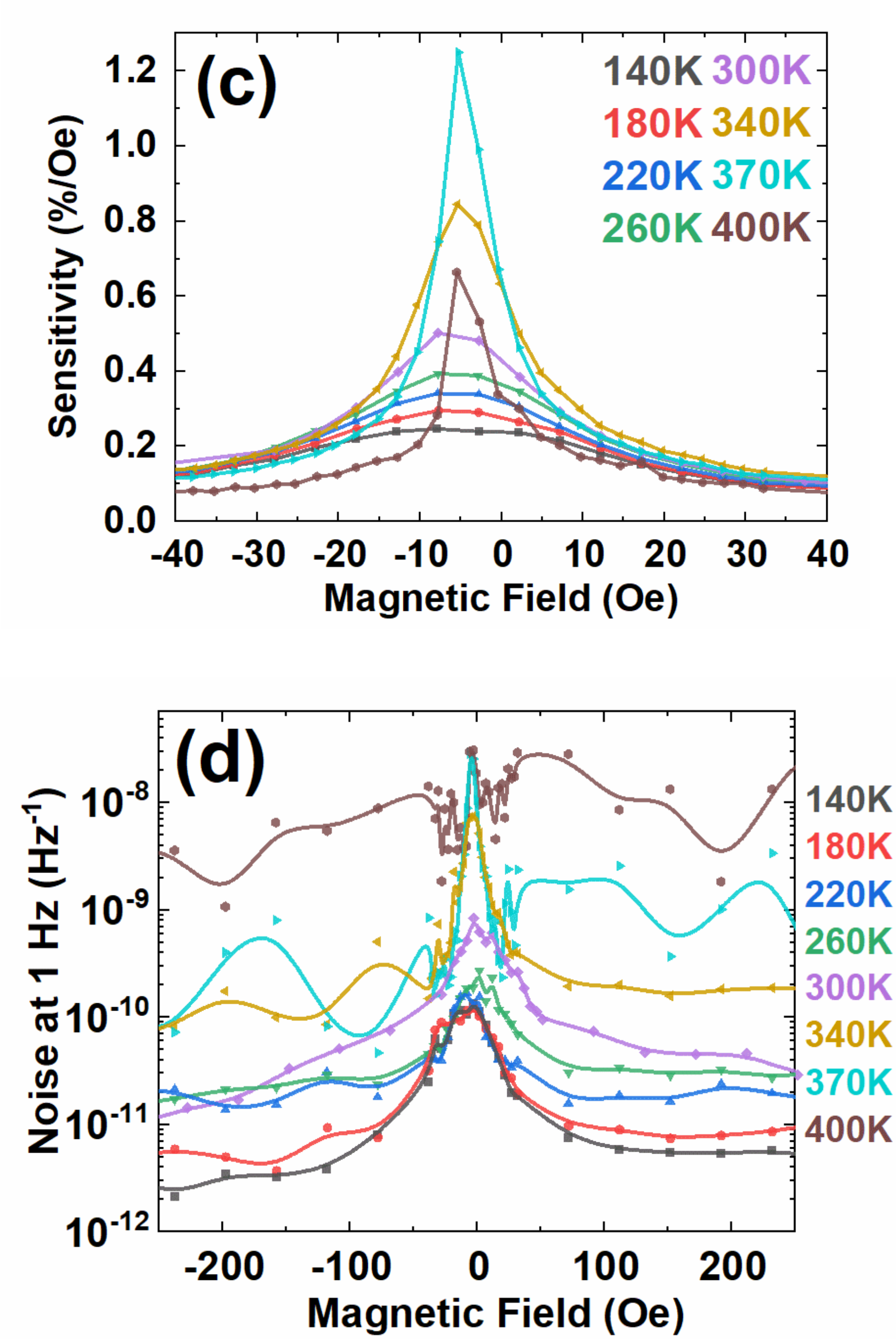

Figure 6. 5 The relation between the temperature-dependent PMA and (a) transfer curve, (b) coercivity, (c) AC sensitivity or (d) 1 Hz noise in an MTJ sensor.

In Fig 6.5(a), the transfer curves indicate that for strong PMA at low temperature, the spins in the free layer are mostly pointing to the out-of-plane direction, and their components in the in-plane sensing direction are small to show a little contribution to the magnetoresistance. The coercivity is read from the transfer curves and given in Fig. 6.5(b). This dependence of coercivity on temperature is related more to thermal-assisted domain nucleation and propagation, and less to the magnetic anisotropy change that we concern about.[120] The practical sensitivity is not monotonous, but has a peak at 370K, as observed in Fig 6.5(c). This peak sensitivity comes from the magnetic anisotropy compensation, where the PMA becomes close to the shape anisotropy. As two types of anisotropy compensate each other, the magnetic moment is free to rotate in space without any restriction. The sensor is thus highly sensitive to external magnetic fields, reaching a sensitivity above 1.2%/Oe which is the highest value in our laboratory. It is noteworthy that the highest sensitivity is reached at 370K, which coincides with the temperature of lowest coercivity in Fig. 6.5(b), but not with the transfer curve of the highest slope at 400K in Fig. 6.5(a). This reveals that the practical sensitivity can't be solely estimated from the transfer curve slope, since tiny coercivity can freeze magnetic moments for small-scale magnetic field changes, regardless of the overall transfer curve. The noise spectral density is measured and normalized by the bias voltage on the senor, and its value at 1 Hz is shown in Fig. 6.5(d). As a common result, at a saturated region under large magnetic fields, a relatively low electrical noise is observed, while a high magnetic noise appears at a sensitive region under small magnetic fields.[121] At high temperatures, the electrical noise increases to a similar level as the magnetic noise. The comparatively high noise of such a sensor leads to a field detectability of around 300 nT/√Hz at a sensitive region.

6.2.4 Magnetic anisotropy compensation

We further measured the practical sensitivities in MTJs with other t_2 and T_a values (t_1=6A). The results for four different MTJ sensors look similar to Fig. 6.5(c), whose peak sensitivity values at low magnetic fields are summarized and shown in Fig. 6.6(a). Each of them has a different fabrication condition, which is introduced previously, leading to different magnetic anisotropy strength inside the free layer. Meanwhile, we estimated the in-plane saturation field from the area between the hysteresis loop and the magnetic field axis as usual in literature, as the free layer magnetization can be calculated from MTJ resistance[35,119]. In literature, this field is called an effective anisotropy field, since the saturation fields in the out-of-plane easy-axis direction are assumed to be negligible. Without such a rough assumption, we prefer to denote it as the in-plane saturation field H_S, which is an indicator proportional to PMA strength. For the same four MTJ sensors, the in-plane saturation fields are shown in Fig. 6.6(b) and related to the peak sensitivities in Fig. 6.6(c).

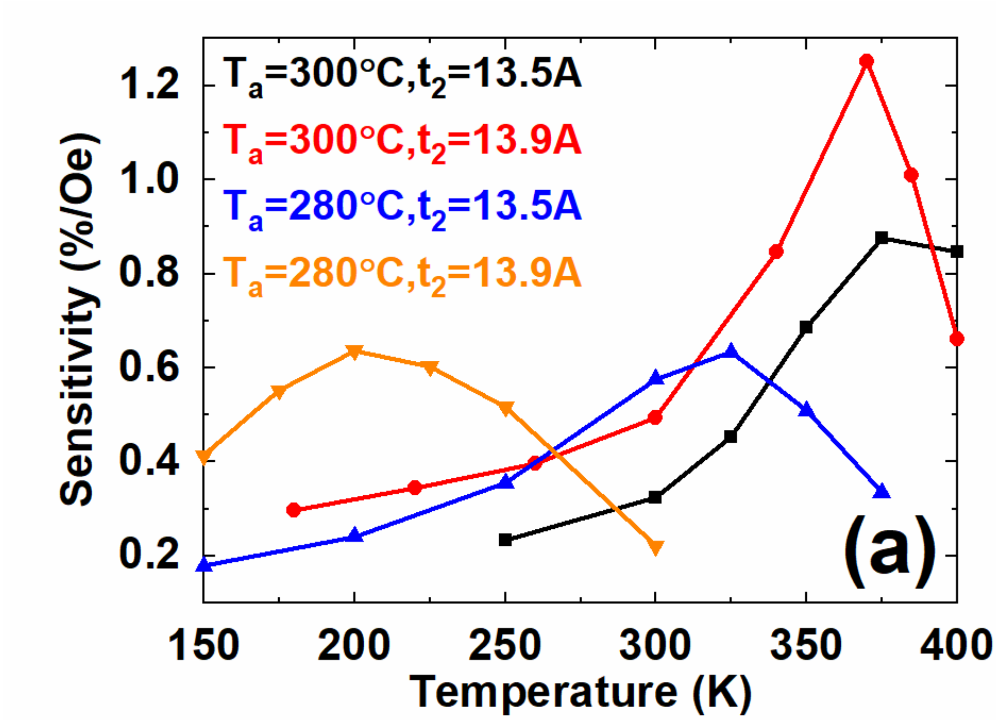

Ta=300°C,t2=13.5A
Ta=300°C,t2=13.9A
Ta=280°C,t2=13.5A
Ta=280°C,t2=13.9A
(a)
Sensitivity (%/Oe)
0.2
0.4
0.6
0.8
1.0
1.2
150
200
250
300
350
400
Temperature (K)

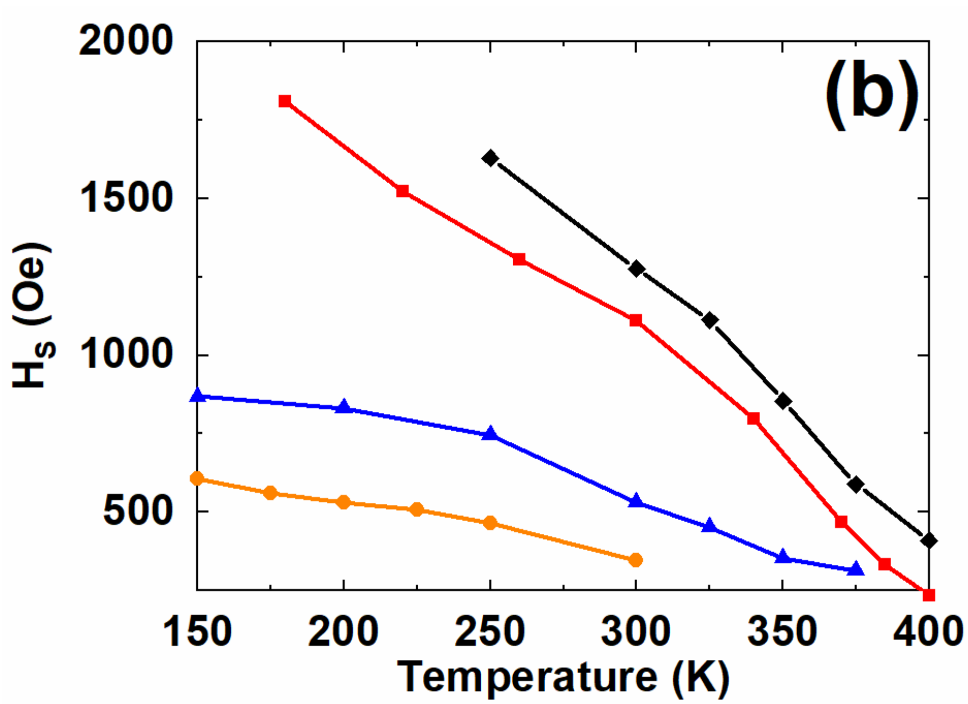

(b)
HS (Oe)
500
1000
1500
2000
150
200
250
300
350
400
Temperature (K)

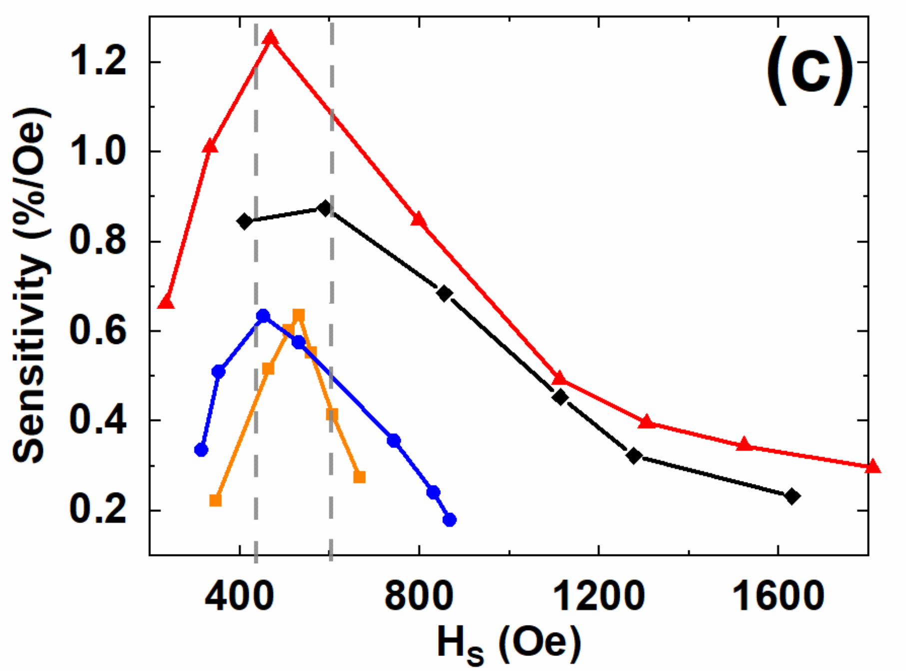

Figure 6. 6 The (a) peak sensitivities at small fields and (b) in-plane saturation magnetic fields for four MTJ sensors at various measurement temperatures, each sensor with individual free layer thickness t_2 and annealing temperature T_a. (c) The relation between the in-plane saturation field and peak sensitivity.

With more results from multiple MTJ sensors, a detailed semi-quantitative relation between PMA and sensitivity is presented, where PMA strength is represented by HS. The peak sensitivity values in Fig 6.6(a) are different for four samples due to a common magnetoresistance difference in our samples, which is directly linked to sensitivity. In Fig 6.6(b), H_S calculated from transfer curves at different temperatures increases together with the PMA strength as temperature drops. In multiple MTJ sensors, while PMA differs intrinsically as demonstrated in Fig. 6.1, the sensor sensitivities are always peaked in a narrow range of H_S, indicated by the dashed lines in Fig. 6.6(c). This is expected since all four sensors share the same shape and demagnetization energy. Thus the compensation condition for high sensitivity requires approximately the same amount of PMA.

6.3 Generation-recombination noise

6.3.1 Voltage-dependent random telegraph noise

A special random telegraph noise (RTN) is observed in these MTJ sensors with PMA in its free layer, which is not observed in MTJ of our previous studies. We have fabricated a single MTJ in a circular shape of 5μm diameter, with other conditions the same as previous MTJ samples. After applying a -400 Oe magnetic field to bring the single MTJ into its saturation as shown in the transfer curves of Fig 6.5(a), we have measured its noise spectrum at various temperatures from 150K to 300K. The tunneling resistance in MTJ is typically decreasing with measuring temperature[122], and so does the voltage drop on it in a series circuit. Therefore, by increasing the measuring temperature we can reduce the bias voltage of MTJ, which is reflected in Fig 6.7. A linear fitting $V = a + bT$ performed in the figure gives that $a = 0.304\, V, b = -1.869 \times 10^{-4}\, V/K$.

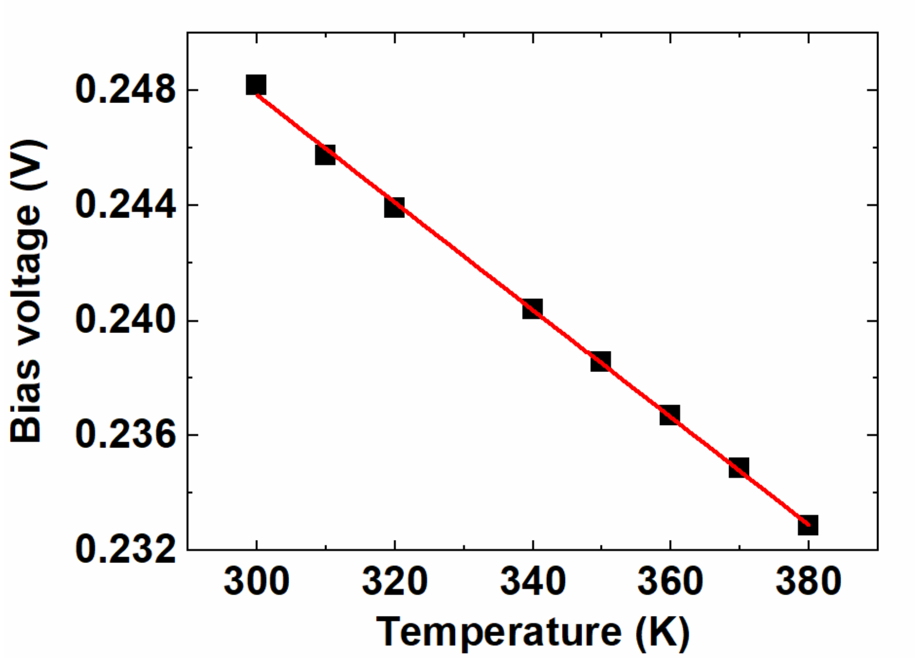

Figure 6. 7 The voltage drop across a single MTJ connected in series with a resistor, related to the ambient temperature; the red line is a linear fitting.

In the meantime, a gradual change in the Lorentzian noise is observed in the temperature scan, which is explained later by the generation-recombination (GR) process with Fermi level lifting. As shown in Fig 6.8 (a), at 150K the noise basically conforms to the dashed line indicating the 1/f noise relation. When the temperature rises to 300K, in the noise spectrum we can observe a bump due to the appearance of a Lorentzian component, with a roll-off frequency near 10 Hz. Such Lorentzian spectrum in MTJs has been previously observed and attributed to the fluctuations between quasi-stable single-domain states in the free layer[56], but the Lorentzian spectrum we observed here is a different one due to the GR process. As the temperature keeps increasing to 380K, the roll-off frequency gradually shifts to higher frequencies of a few hundred Hertz, and its signal amplitude decreases. A corresponding time domain voltage signal from this MTJ is shown in Fig 6.8 (b). At 300K, we begin to see a two-level flipping as an expression of the Lorentzian spectrum, with a long relaxation time at one state near 0.1s; at 380K, the flipping becomes much faster with a 0.001s relaxation time. By combining Fig. 6.5 (c) and (d), we plotted in Fig. 6.8(c) the scaling relation between noise and sensitivity. The data basically follows a quadratic guideline, implying that the field detectability won't be improved by higher sensitivity. Higher sensitivity just comes with an equivalently more amount of noise in this sensor.

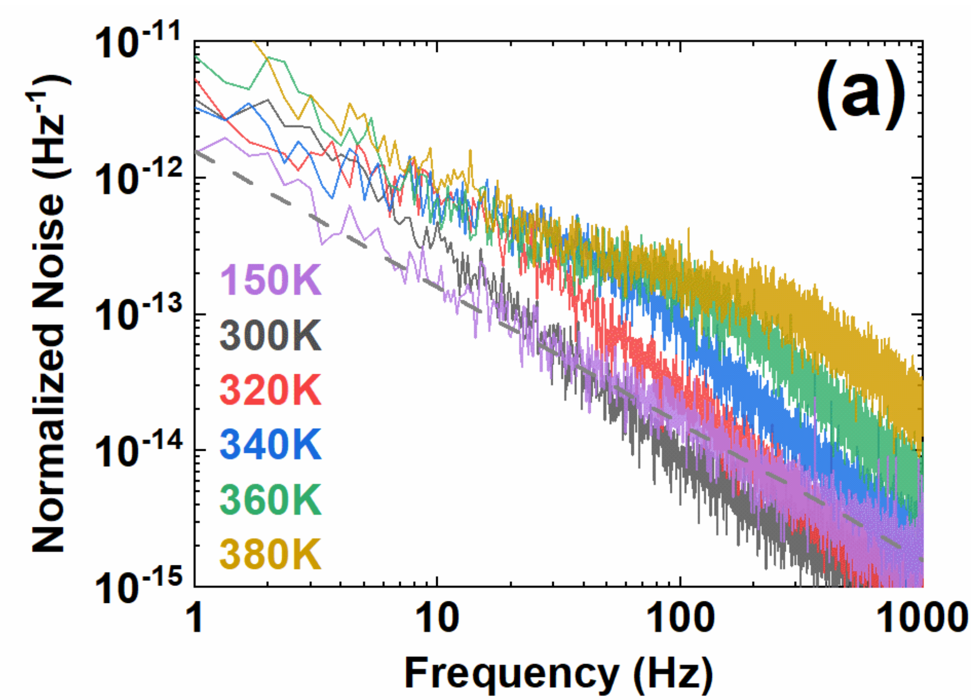

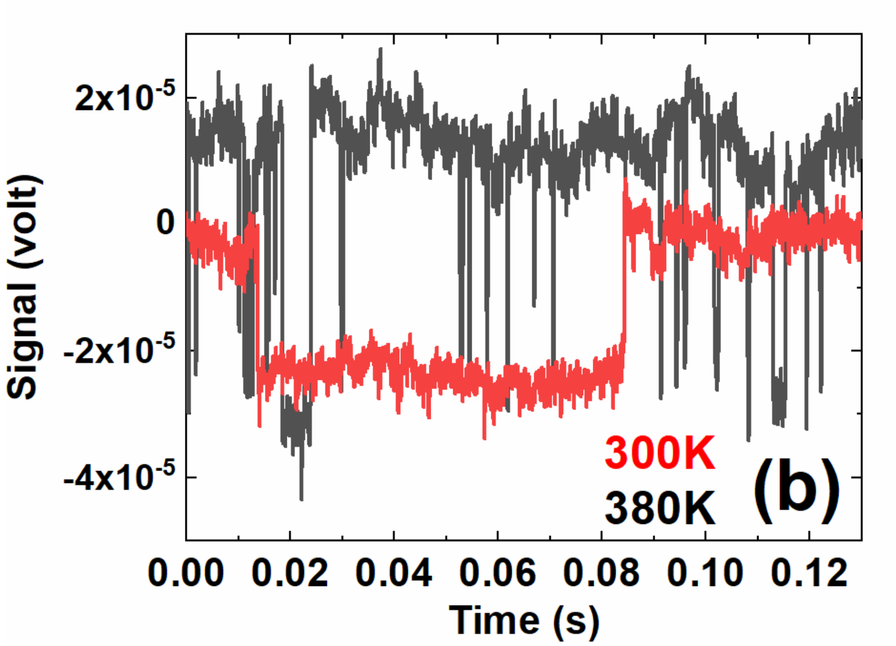

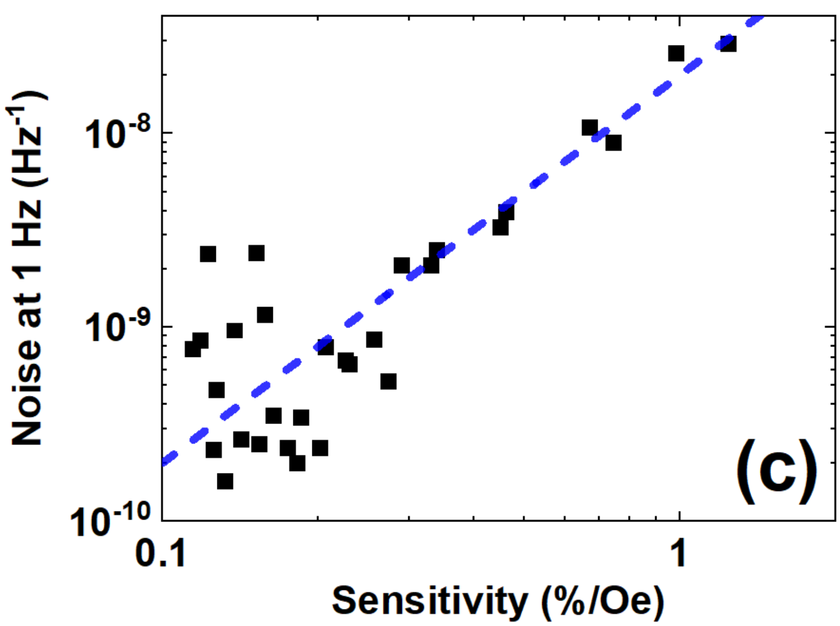

Figure 6. 8 (a) The Lorentzian spectrum of the RTN noise in MTJ at various temperatures, with a dashed line indicating 1/f noise. (b) Two-level flipping signals at two temperatures. (c) The quadratic scaling law between the noise and sensitivity of MTJ.

6.3.2 Fermi level shifting

These two-level flipping signals are originated from a GR process most likely due to certain localized states inside MTJ, instead of quasi-stable domains in the free layer. It is an electrical noise measured at saturation magnetic fields, where all magnetic noise is suppressed. In the tunneling current of MTJ, Electrons carry energy at the Fermi level of the positive electrode, which is in the conduction band of CoFeB[123]. This Fermi level can also be shifted by the bias voltage by the amount of eV, e being the electron charge[124]. Considering the RTN noise discussed theoretically in section 3.5.5, where the flipping between a localized trap state and the state in the conduction band provides such two-level signals, the relaxation time in two states can be expressed as below:

$$\begin{cases} \tau_t = \tau_0 \exp\left(\frac{E_0}{\gamma k_B \mathrm{T}}\right) \\ \tau_c = \tau_0 \exp\left(\frac{E_0 + eV}{\gamma k_B \mathrm{T}}\right) \end{cases}$$

$$\Rightarrow \begin{cases} \ln(\tau_t) = \frac{E_0}{\gamma k_B}\left(\frac{1}{T}\right) + \ln(\tau_0) \\ \ln(\tau_c) = \frac{E_0 + e(a+bT)}{\gamma k_B \mathrm{T}} + \ln(\tau_0) = \frac{E_0 + ea}{\gamma k_B}\left(\frac{1}{T}\right) + \frac{b}{\gamma k_B} + \ln(\tau_0) \end{cases}$$

where τ_t, τ_c are the relaxation time for the trapped state and the conductive state at the Fermi level respectively; τ_0 is an attempt time in the nanosecond range for the electron migration process, and γ is an empirical constant[62]. At zero bias voltage, E_0 is the energy barrier to overcome in the flipping between two states, and the trapped state is assumed to have an energy close to the Fermi level. At a bias voltage V, the Fermi level is lifted by eV, while the trapped state energy is unchanged. To confirm this theory, we have collected and calculated the average dwell time τ_t, τ_c in 30 seconds for both states in the localized trap and the conduction band. The results are plotted in Fig 6.9 in a semi-log scale, where tunneling electrons are assumed to spend less time being trapped than conductive. The fact that the flipping happens more frequently for higher temperatures is exemplified by the reduction of dwell time in both trapped and conductive state.

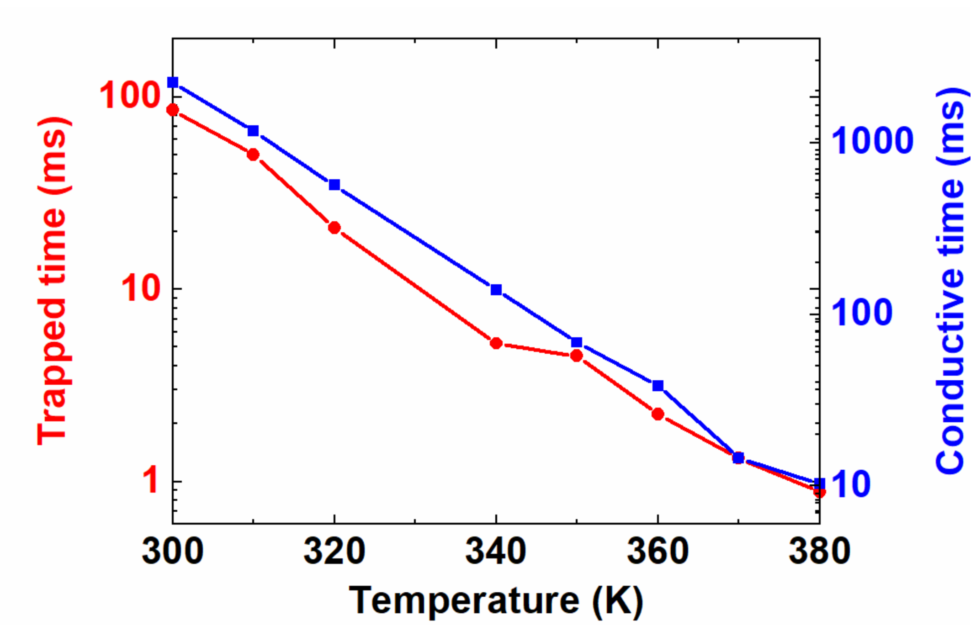

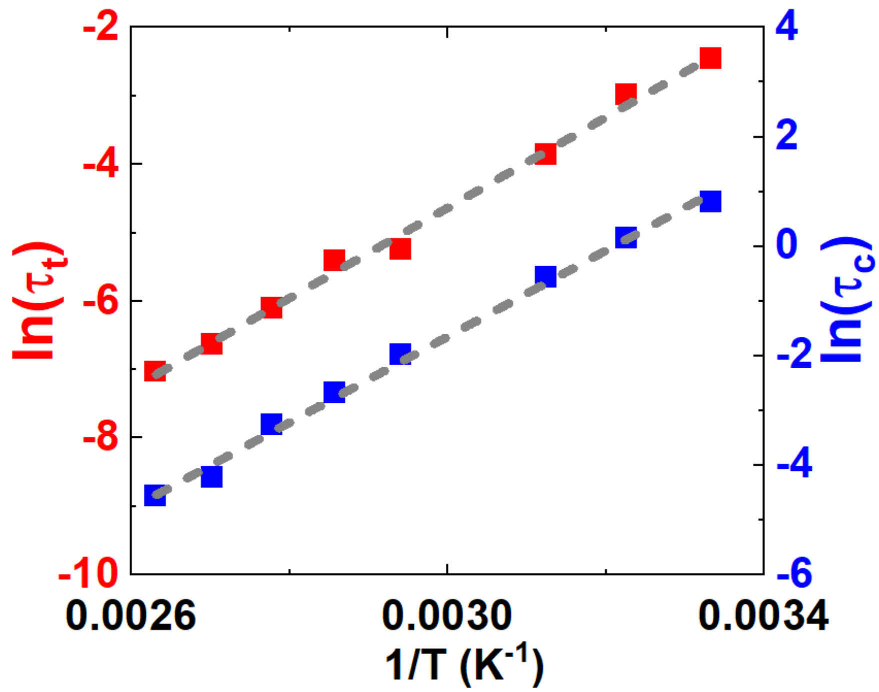

Figure 6. 9 The dwell time at two states of the two-level flipping signals in Fig 6.8, averaged at different temperatures (top); the linear relations between $\ln(\tau_t)$, $\ln(\tau_c)$ and $\frac{1}{T}$ (bottom).

In the bottom figure of Fig 6.9, by a linear fitting on the relation between $\ln(\tau_t)$, $\ln(\tau_c)$ and $\frac{1}{T}$, we obtained that $E_0 = 2.59 \times 10^{-19} J$ and $\gamma = 2.84$. So far, the temperature-dependent Lorentzian noise coincides well with the model of GR noise, while the underlying cause of the localized trap in this system remains an open question. Moreover, multiple Lorentzian spectra in Fig. 6.5(a) can be reconstructed by:

$$S(f) = \frac{4I^2}{(\tau_t+\tau_c)[(1/\tau_t+1/\tau_c)^2+(2\pi f)^2]}$$

which is expected from a general RTN theory, I being the difference in the voltage signals of two states.

MTJ with such evident two-level fluctuations can be developed into random number generators. There has been a growing interest in making random number generators using the thermal noise of superparamagnetic MTJs, which has minimal energy cost and CMOS compatibility[125,126]. The GR noise found in MTJ with PMA could also provide similar potentials, with a random number generation speed tunable by bias voltage, as we demonstrate. Compared to the nanoscale size required by superparamagnetism, GR noise can be more easily obtained in micrometer-sized MTJ patterned by typical photolithography.

Chapter 7 MTJ Gradiometer for Non-destructive Evaluations

7.1 Introduction

Based on our developments on MTJ sensors introduced in previous chapters, we will apply MTJs to a crack detection project to demonstrate its usefulness. We have first designed a magnetic gradiometer on a printed circuit board level, with vortex MTJs mounted as its sensors. The gradiometer benefits from the stability and consistency of vortex MTJs, to present a high common-mode rejection ratio of 83 dB in experiments. Afterward, a crack detection model of magnetic cement is built up, with which this magnetic gradiometer will be tested to perform a nondestructive evaluation. The testing results show that the gradiometer is remarkably effective in locating an artificial surface crack at a superior stand-off distance of 22 mm.

7.2 Critical applications

7.2.1 Non-destructive testing

Nondestructive testing (NDT) is widely used in the industry for noninvasive inspecting, diagnosing, or evaluating materials for defects and inhomogeneity. Common techniques in NDT include ultrasonic sensing, Eddy-current testing, and magnetic flux leakage (MFL) measurement. With skin depth limitations, Eddy-current testing is effective when applied to nonferrous conductors[127]. The distance between the sensor and a crack to be detected, defined as the standoff distance, is typically limited to 1 mm for Eddy-current testing[128]. MFL detects the magnetic field leakage in the vicinity of cracks, which has a high standoff distance for ferromagnetic materials[129]. Ferrous metals are prevalent in infrastructure, and even cement can become weakly magnetic by impregnating magnetic powders or steel into the cement slurry (Class H cement)[130]. As demonstrated in Fig 7.1, as steel structure is magnetized by adjacent permanent magnets placed near sensors, its abnormal shape (crack) will generate a characteristic magnetic field signal for the sensor to detect. No contact or damage is done to the steel-concrete mixture.

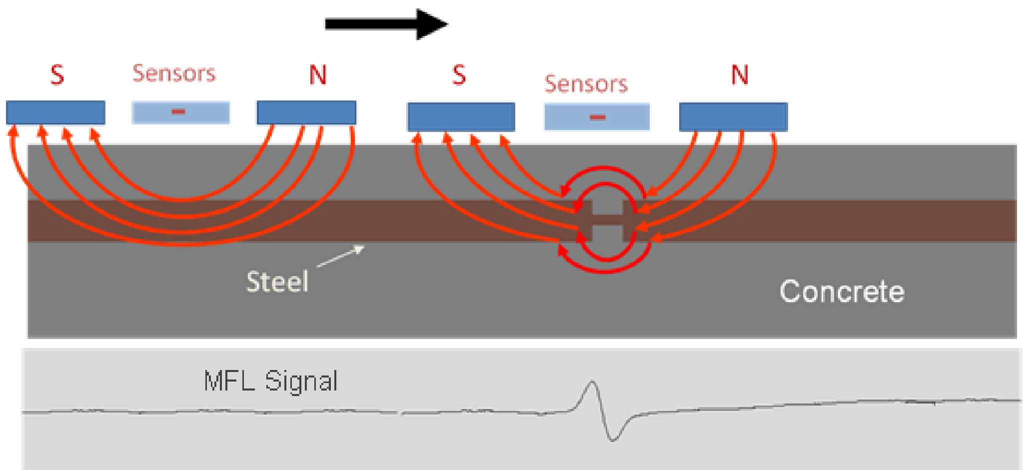

Figure 7. 1 Schematics of MFL measurement to detect steel anomalies. Steel is magnetized by the magnetic fields from the north to the south pole of a magnet, and then the signal from its anomaly can be sensed. The below figure is the signal indicating the anomaly position.

MFL probes can thus be used to inspect oil boreholes with cement sheath, without touching its surface. As the Deepwater Horizon oil spill disaster in 2010 was caused by defective cement of boreholes, the structural integrity of the cement sheath is critically important to public safety[131]. The exponential decay of magnetic signals over distance limits the standoff distance in MFL testing to 3 to 7 mm. This distance is not large enough, since a typical cement sheath has a fiberglass casing of a few centimeters thickness[132]. Therefore, extending the standoff distance of MFL beyond multiple centimeters would represent a breakthrough in NDT technology for the energy industry, which we are going to work on using our vortex MTJs.

7.2.2 Magnetic gradiometry

In MFL testing, an excitation coil is used to induce magnetization in the defective material. Compared to sophisticate self-nulling coil configurations, it is appealing to use a magnetic gradiometer, which is more compact and immune to the excitation field. A gradiometer takes the differential signal from two magnetic sensors separated by a certain distance, called base length, to distinguish a gradient signal from common backgrounds such as the excitation field, the Earth field, and the environmental electromagnetic interference[13]. The gradient field could come from localized magnetic sources such as surface cracks. Various types of magnetic sensors including optical magnetometer, fluxgate, diamond nitrogen-vacancy center magnetometer, and SQUID (Superconducting Quantum Interference Device) have been used to construct gradiometers.18-21 Nevertheless, they suffer from large physical sizes (5 – 10 cm), high power consumption (100 – 200 mW), low roll-off frequency (10 – 1000 Hz), small dynamic range (a few Oe), or the need of sophisticate accessories (laser pump to cryogenics). On the other hand, highly sensitive magnetic tunneling junction (MTJ) sensors enjoy compelling advantages, including low power consumption (~1 mW), broad bandwidth (up to GHz), miniaturized size (~10 μm), high-temperature operation (~350 °C) and a fabrication process compatible to silicon circuit technology[133].

Generally, the signal output of a gradiometer can be expressed as:

$$V = D[H(z_1) - H(z_2)] + C[H(z_1) + H(z_2)]/2$$

z_1 and z_2 are the position coordinates of the signal and reference sensors, D and C are meant to be the sensitivities for the gradient field $[H(z_1) - H(z_2)]$ and uniform field $[H(z_1) + H(z_2)]/2$, respectively. The ratio D/C yields the common-mode rejection ratio

(CMRR) of the device, and the larger the CMRR the better it can discern a small gradient signal out of various uninteresting uniform ambient backgrounds.

7.3 Prototype design and testing for detecting cracks in cement structures

7.3.1 MTJ-based gradiometer

From the working principle of a gradiometer, sensitivities of the two magnetic sensors must be precisely matched. Hysteretic sensors are thus not suitable, due to the time drift in the sensitivity caused by irreversible magnetic domain wall motions. For this purpose, we use an MTJ array sensor with single vortex magnetization in the free layer, introduced in section 5.4 to assure non-hysteretic operations. Figure 7.2 shows our gradiometer with two MTJ array sensors wire–bonded onto a green printed circuit board (PCB), whose signal conditioning circuitry is given below it.

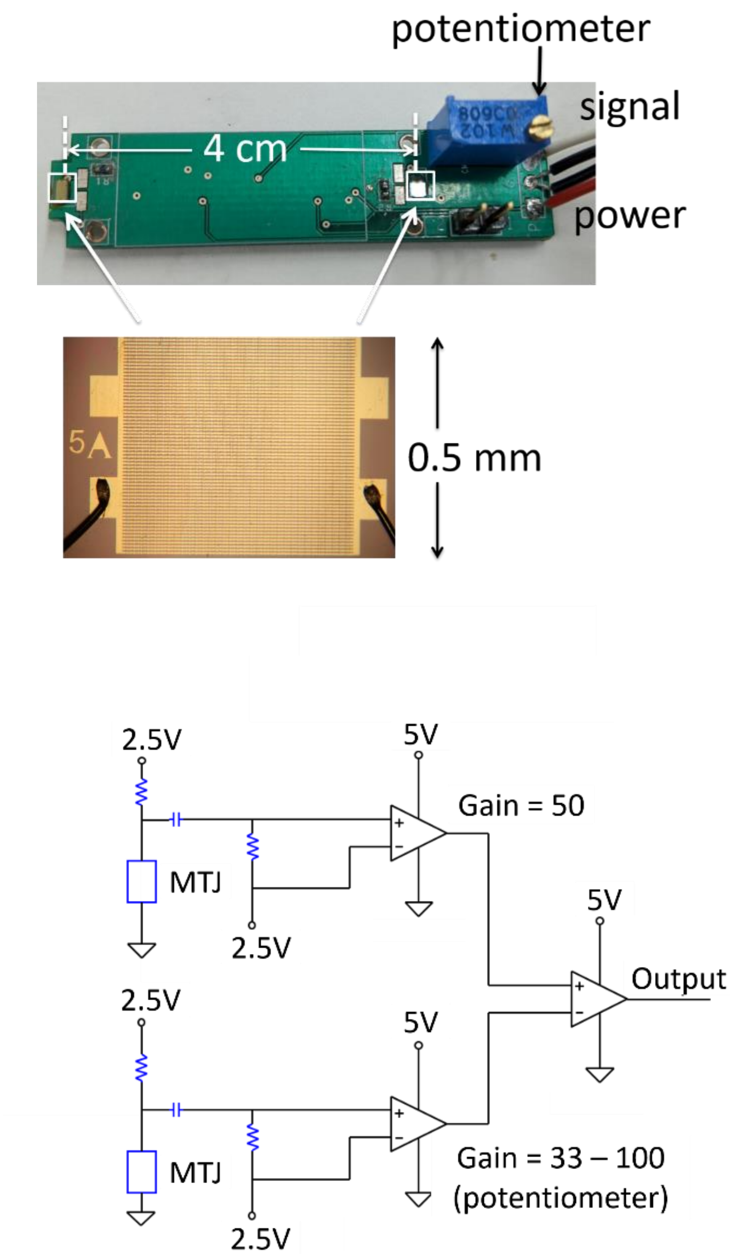

Figure 7. 2 The magnetic gradiometer on a PCB and a micrograph of the MTJ array sensor are shown in the top photo; in the bottom is its electronic circuit design, where the voltage signals from two MTJ sensors are amplified individually and then differentiated. The first amplification gain of one MTJ signal is adjustable by a potentiometer.

The circuit is powered by four AAA batteries. The two sensors under a 1 V bias voltage are separated with a base length of 4 cm. The voltage signals from two sensors first go through high-pass filters with the -3 dB point at 5 Hz, then get boosted separately by two identical amplifiers (INA828) of negligible noise. The signal from the “signal sensor” at the edge of the PCB is amplified by 50 times, while the other “reference sensor” has a tunable amplification factor between 33 and 100 adjustable by a potentiometer. After an initial adjustment of the potentiometer, a close match of two sensitivities can be achieved and maintained indefinitely. Next, the amplified signals are differentiated and read by a data acquisition device. Software-based lock-in amplification is performed finally to extract the signal at a specific frequency, with a small time constant of 200 ms corresponding to 0.7 Hz noise bandwidth.

This gradiometer is then calibrated by the magnetic field generated by a pair of standard single-axis Helmholtz coils. When the current in two coils runs in parallel directions, a uniform magnetic field is generated to give the sensitivity C for the uniform field; when in antiparallel directions, a gradient field sensitivity D is obtained. The voltage outputs from the gradiometer after around 50 times amplification are given in Fig 7.3, for the gradient and uniform field calibration in two colors respectively. We can see it responds to a gradient field with much larger voltage, while for the uniform field it’s only in micro-volt scale. The uniform field signal is mostly due to the little difference in the sensitivities of two MTJ sensors. The Helmholtz coil calibration gives D = 1000 V/T and C = 0.075 V/T, which yields a large CMRR of 83dB, even comparable to a SQUID gradiometer operating at liquid helium temperature[134].

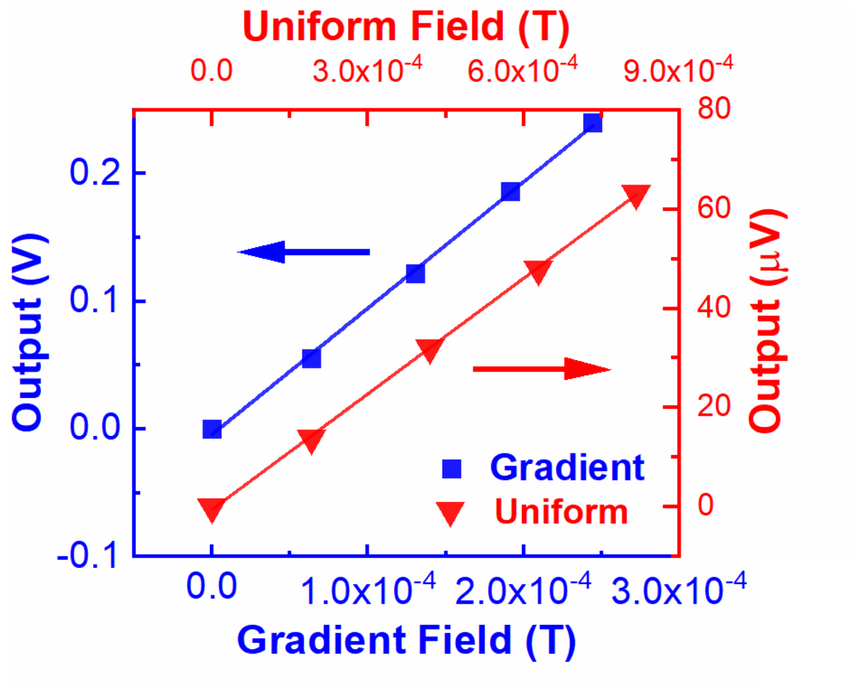

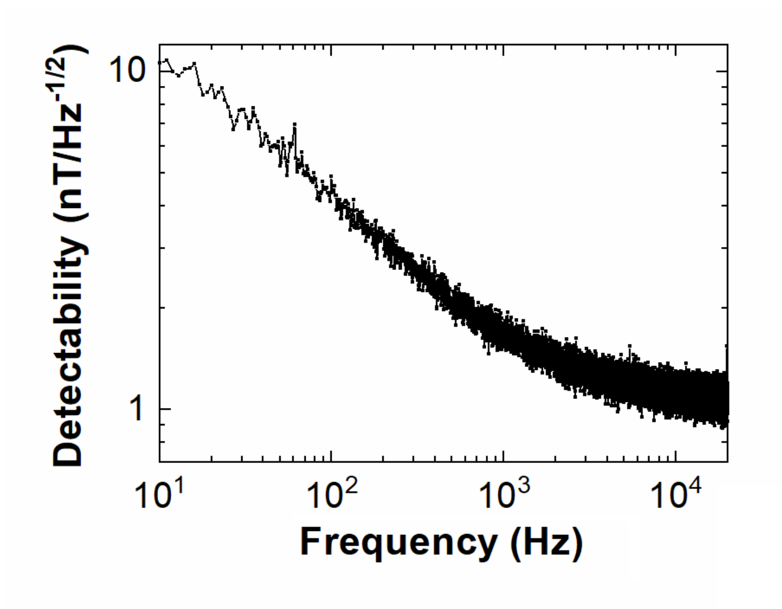

Figure 7. 3 The voltage signal of the gradiometer output in the Helmholtz coil calibration, with linear fittings giving its sensitivities for gradient and uniform fields. In the bottom figure, the field detectability of the gradiometer is derived from its noise spectrum density.

We have also measured the intrinsic noise power spectral density of the gradiometer to derive the magnetic field detectability of the gradiometer as shown in Fig. 7.3. At our usual 1 kHz operating frequency of the gradiometer, the field detectability is 1.6 nT/√Hz. The goal is to make the detectable field limit of gradiometers as low as possible to detect deep cracks. In summary, with a large dynamic range, vanishing coercivity, superior detectability, high thermal stability, and low power consumption, our robust and portable MTJ-based gradiometer is highly suitable for applications in various industries.

7.3.2 Crack detection simulation

In the beginning, we used the COMSOL® Multiphysics software to simulate a detection configuration in literature and to find possibly better configurations before any experiments[135]. In the top figure of Fig 7.4 is the configuration used in reference [10], where a coil with the equivalent magnetic moment of 1 Am^2, and a sensor 30cm away from it are used to detect the magnetic field component in the Z direction H_Z. The change in H_Z is caused by a 2 cm^3 cubic cavity inside the magnetic cement on the top. The following figure shows the configurations we designed consisting of a smaller excitation coil with the same magnetic moment in a vertical orientation, and a sensor 2 cm away from the coil measuring magnetic field component H_X near the cement surface. h_1 and h_2 are adjustable, and here they are set as 3 and 0 cm respectively in this scheme. The magnetic fields H_Z and H_X are then stimulated and given.

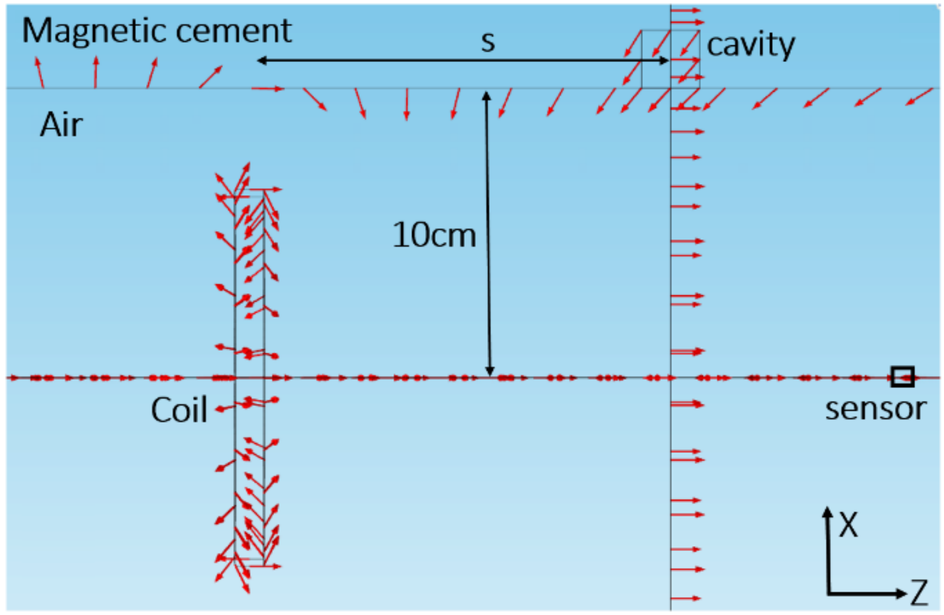
Magnetic cement
s
cavity
Air
10cm
Coil
sensor
X
Z

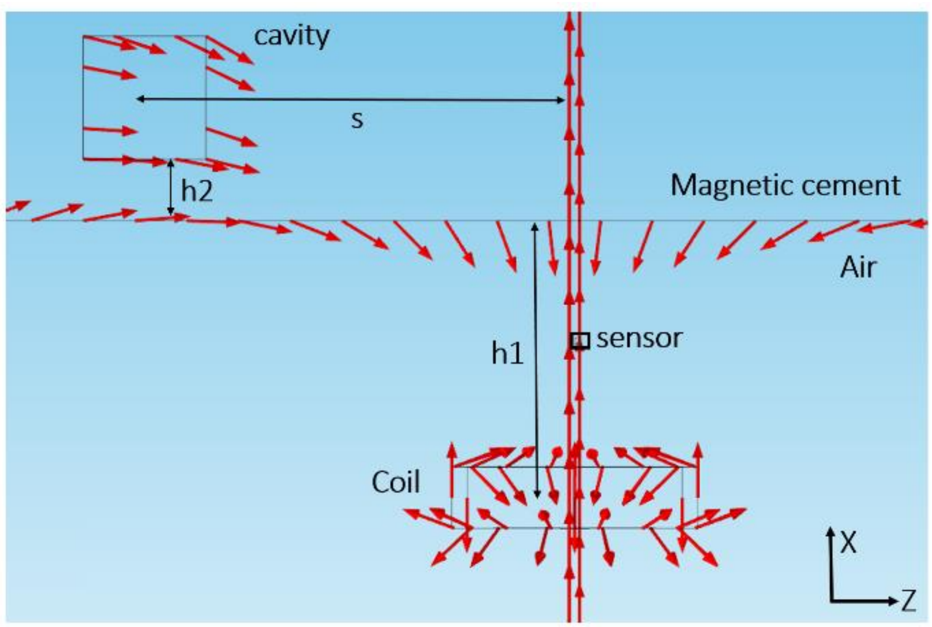
cavity
s
h2
Magnetic cement
Air
h1
sensor
Coil
X
Z

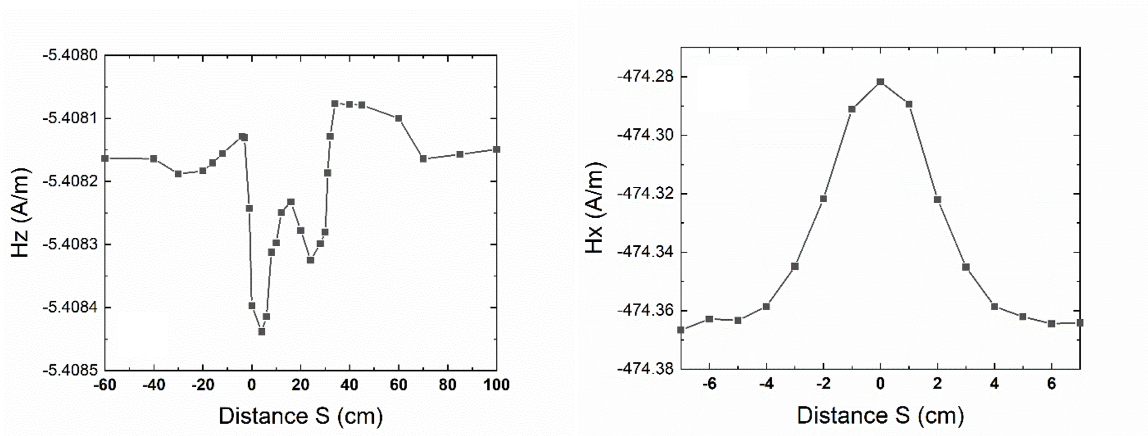

Figure 7. 4 Two detecting configurations sensing H_Z or H_X are shown respectively in the first and second figure, aiming to locate the cavity in a magnetic cement; the red arrows in the configurations show the magnetic fields in space. The corresponding H_Z or H_X field as a function of the labeled distance "S" is simulated and shown in the bottom figure for comparison.

The diagrams in Fig 7.4 below two configuration schematics are the corresponding magnetic field components calculated by simulation, as the sensor together with the excitation coil scans across the cavity horizontally. On the left diagram, H_Z changes due to the cavity only by 0.0003 A/m. Our new configuration is better in that it gives a 200 time bigger signal change of 0.08 A/m in H_X, as shown on the right diagram, which will be adopted in the following discussion due to its much larger signals. The first configuration measuring H_Z has a shortcoming in its dispersive magnetic fields, which is not concentrated spatially to the local cavity, but rather influenced by a large region of the magnetic cement. The issue in H_X component measurement is a much bigger background common-mode field of around 474 A/m, due to the proximity of an excitation coil. However, this problem turns out to be easily solved by using our gradiometer with high CMRR.

Based on our new detection configuration, Fig 7.5 shows a schematic of MFL testing we intend inside an oil wellbore, where a test platform with eight gradiometers installed in a circumferential configuration is inserted. The test platform rotates circumferentially to detect hidden cracks in the cement sheath behind the non-magnetic fiberglass casing. Considering the large size of the wellbore, close to its inner surface, the rotating scanning is equivalent to a planar measurement for each gradiometer if we neglect the surface curvature. The individual situation can thus be simplified to a planar scan shown in the right figure of Fig 7.5, where we set up a coordinate system with a Z-axis in the out-of-plane direction, and an artificial surface crack is placed for the gradiometer to locate.

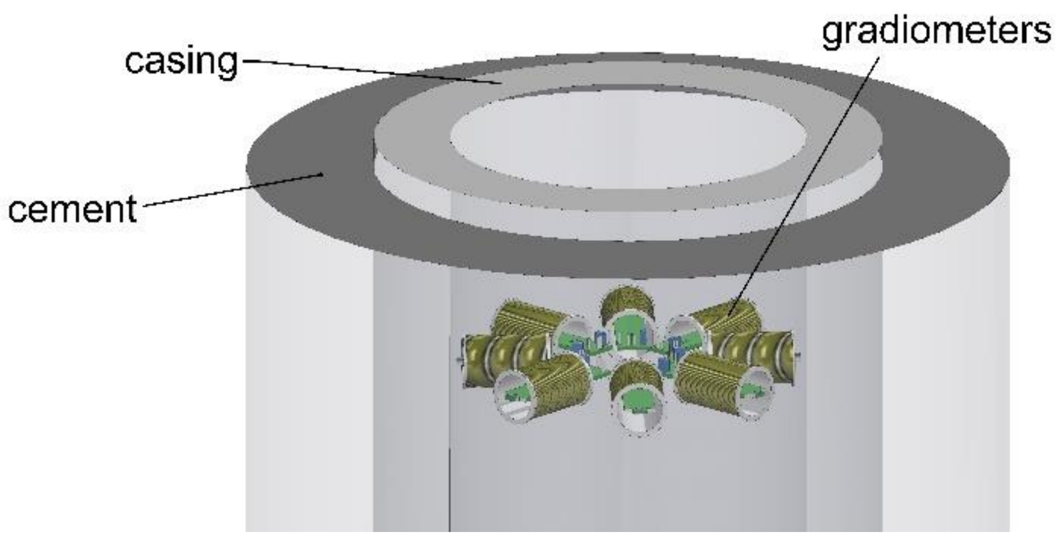

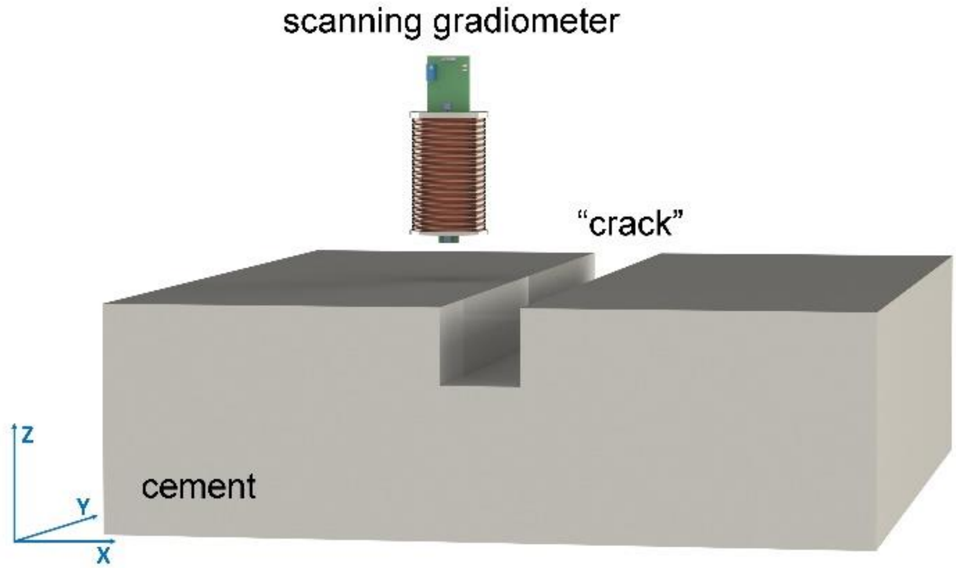

Figure 7. 5 The schematic of a test platform with 8 gradiometers mounted, inserted into a wellbore to scan possible cracks in the cement wall behind a casing (top). Each of these 8 circumferential scan is analogous to a planar scan on a flat cement surface (bottom).

Corresponding to the planar scan case in Fig 7.5, we create a simulation model where a magnetic cement slab is built with 5 cm thickness, and its top surface constitutes the X-Y plane. The X-Z plane is plotted in Fig 7.6, where the signal sensor in the gradiometer is located above the surface, where a standoff distance h_1 is defined. Embedded beneath the surface is a void crack in the shape of a long square tube along the Y-axis with a cross-section of 2×2 cm^2. The depth of the crack into the cement is defined as h_2, and the horizontal offset distance of the "crack" from the signal sensor is S. The gradiometer is placed symmetrically along the axis of an excitation coil, so that the excitation field is common to both MTJ sensors on it. Two MTJ sensors measure the Z-axis component of the magnetic fields. The excitation coil used for magnetization induction in the cement is set to have a diameter of 2.5 cm, length 3.4 cm, and winding 120 turns, operating with 1 A current at 1 kHz.

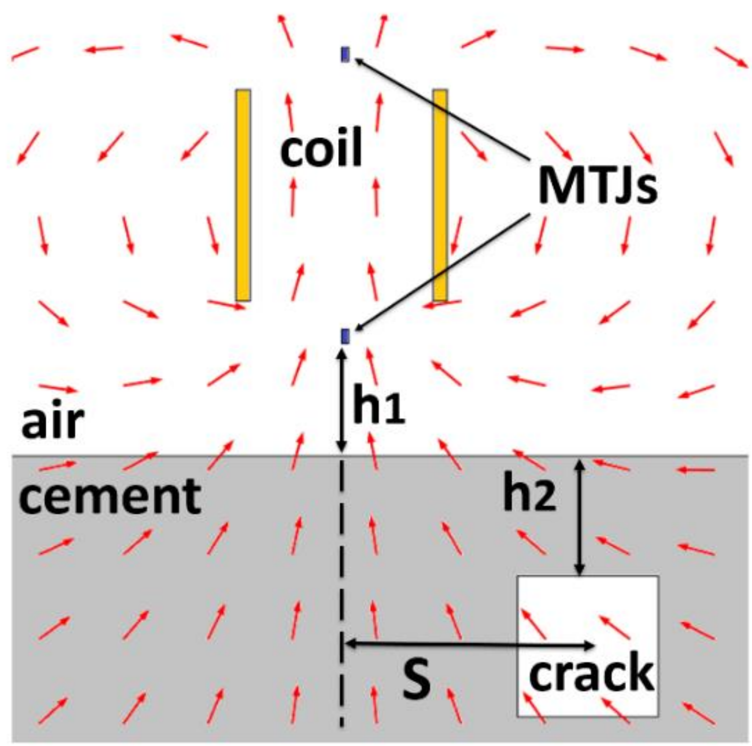

Figure 7. 6 A cross-section view of the X-Z plane of the second figure of Fig 7.5, with a square-shaped void defect in the cement, the excitation coil, and the two sensors of the gradiometer. h_1, h_2, and S are defined in the sketch and red arrows are the simulated magnetic induction lines.

The relative permeability of the magnetic cement is set as 1.09, which is the experimental value we will introduce later. Under these conditions, we simulated the magnetic field distribution with field lines shown as red arrows. The simulation is based on Ampere's law in magneto-statics. The cell size used for meshing is 0.05 cm near the sensor region, and the zero-potential boundary is a spherical surface 2 meters away from the sensors. The common-mode field from the excitation coils at two sensor positions is 11.4 Oe, no bigger than the MTJ dynamic range, and will be rejected by the gradiometer in principle. The difference between fields at the signal and reference sensor is recorded, directly corresponding to the gradiometer output. This differential field $\Delta\boldsymbol{H_Z}$ varies as the gradiometer scans across the crack, to indicate the position of an embedded crack in the magnetized cement.

Fig 7.7 shows the map of the differential field $\Delta\boldsymbol{H_Z}$ on the X-Z plane at every location of S and h_1, with $h_2 = 0$ corresponding to a crack on the surface. At distant positions away from the magnetic cement, $\Delta\boldsymbol{H_Z}$ remains low and unaffected; as the sensors move down, $\Delta\boldsymbol{H_Z}$ increase sharply due to the localized gradient field of the cement. In the central region near S = 0 the sensors are right on top of the crack, which leads to a 2 cm region of constant $\Delta\boldsymbol{H_Z}$, which is characteristic of the crack width. The bottom figure of Fig 7.7 shows the exponential decay of $\Delta\boldsymbol{H_Z}(\boldsymbol{0}, \boldsymbol{h_1})$ over h_1, plot along the S = 0 line. Considering a 300 nT detectable limit which is our experimental result to be presented later, the intercept on the fitting line implies that the gradiometer could see such surface crack with standoff distances between 2 and 3 cm.

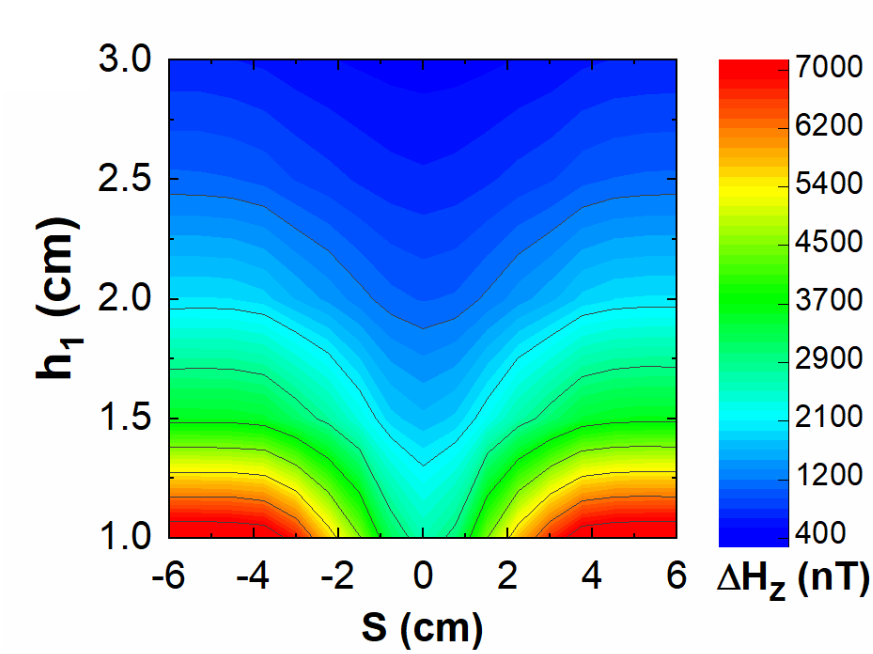

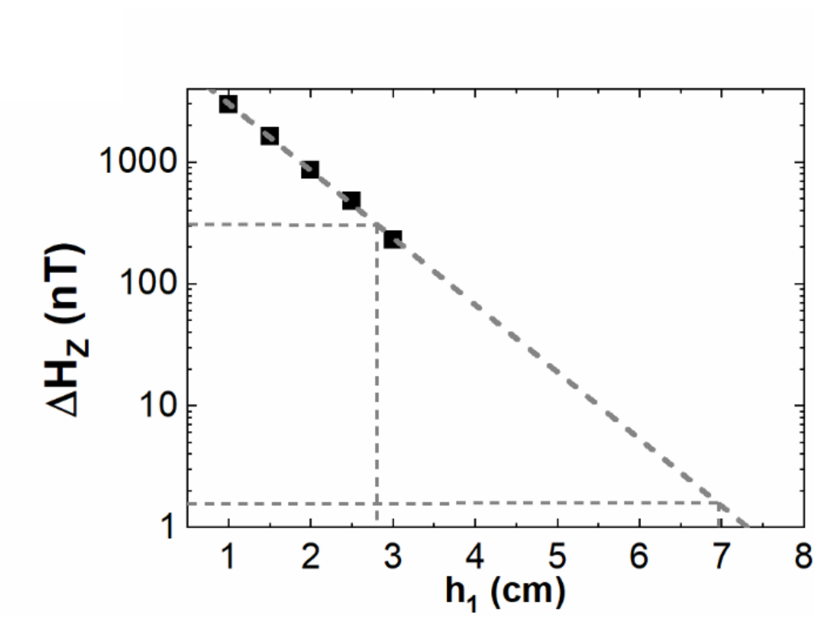

Figure 7. 7 The simulated $\Delta \boldsymbol{H}_{\boldsymbol{Z}}(S, h_1)$ in the X-Z plane for $h_2 = 0$ (top), and the exponential decay of $\Delta \boldsymbol{H}_{\boldsymbol{Z}}(0, h_1)$ over h_1 at the S = 0 position of the top figure, with a linear fitting (bottom). The standoff distances h_1 corresponding to two detectable limits $\Delta \boldsymbol{H}_{\boldsymbol{Z}}$ = 300 nT and 1.6 nT are shown by dashed guidelines.

During an actual MFL measurement, the gradiometer scans horizontally across the crack region at a constant stand-off distance of h_1. By performing simulation at different sets of $h1$, $h2$ values (in cm) to mimic actual measurements, Fig 7.8 shows $\Delta \boldsymbol{H_Z}$ in the range of S within S = ±6 cm, which indicates the presence of the crack at S = 0 position. For each curve, its value at S=±6 cm is deducted as the offset signal, since only the change in the signal across the crack matters to the overall measurement.

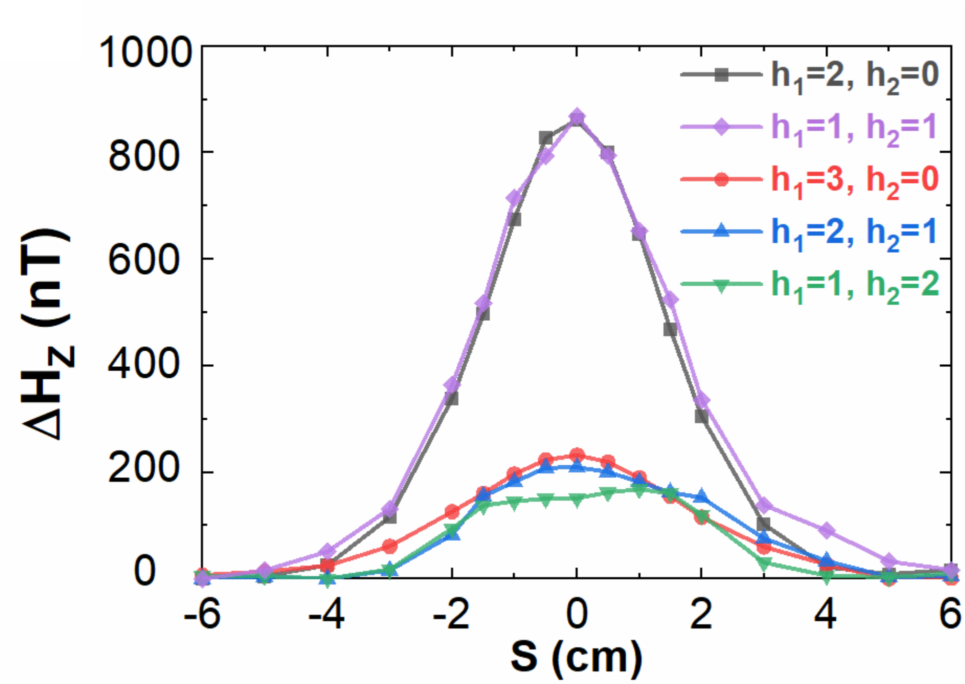

Figure 7. 8 The simulated $\Delta \boldsymbol{H_Z}$(S) profile scanned at multiple (h1 + h2) distances to the crack, under the same excitation field.

Under the condition h_1+ h_2 = 2, the cases of a surface crack (h_1= 2, h_2 = 0) and an embedded crack (h_1= 1, h_2 = 1) both show $\Delta \boldsymbol{H_Z}$ (S) profiles of similar bell curves with a peak value of 860 nT and an FWHM (full width at half maximum) of about 3.2 cm. Increasing h_1+ h_2 to 3 cm, we examined three cases: a surface crack (h_1= 3, h_2 = 0), a shallow crack (h_1= 2,h_2 = 1), and a deep crack (h_1= 1, h_2 = 2). Again, all the scanned profiles resemble each other, with a peak value of 210 nT and an FWHM of about 4.2 cm. Conclusively speaking, regardless of how deep the crack is, a differential magnetic field is generated whose peak value decreases exponentially with the sensor-to-crack distance h_1+ h_2, and its spatial spread is characteristic of the lateral dimension of the crack. Considering a 300 nT detectable limit, which is the limit of our device to be discussed later, the simulated peak signal in $\Delta \boldsymbol{H_Z}$ (S) indicates that the gradiometer can see surface cracks with a maximum standoff distance around 2 to 3 cm. Next, we proceed to test the gradiometer on real magnetic cement for experimental confirmation.

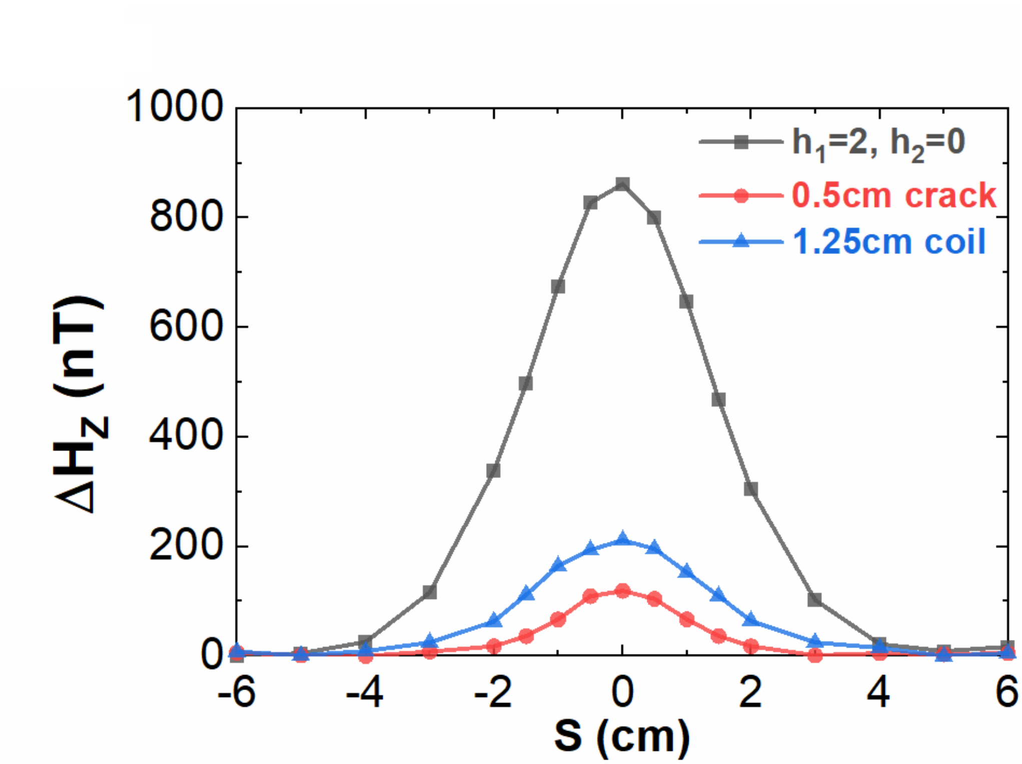

Figure 7. 9 The similar $\Delta \boldsymbol{H_Z}$(S) profiles for a smaller coil or crack, in comparison with the h_1=2, h_2=0 case in Fig 7.8.

The characteristic FWHM is further studied in Fig. 7.9 for a smaller coil of 1.25 cm diameter and a smaller crack with a cross-section of 0.5×0.5 cm^2, with other conditions the same as the (h_1= 2, h_2 = 0) case in Fig. 7.8. FWHM decreases from 3.2 to 2.2 cm reasonably for a smaller crack. With a smaller coil the FWHM doesn't change, but the amplitude of ΔH_Z decreases. This is on account of a more localized field, in which magnetic induction lines are all concentrated near the small coil to magnetize less cement region.

7.3.3 Experimental testing of cement structures with cracks

Finally, we proceed to test the gradiometer on real magnetic cement for experimental confirmation. The setup for MFL testing using our gradiometer is illustrated in the photo in Fig 7.10, basically identical to the configuration in Fig 7.6. The magnetic cement used in the model is made by mixing a small amount of ferromagnetic Fe_3O_4 particle powder (Alpha Chemicals®) into non-magnetic plaster before the cement setting. The volume fraction of the Fe3O4 particles is 4.6 % corresponding to a mass fraction of 6.0 %. The bottom diagram in Fig. 7.10 shows its magnetic hysteresis loop at room temperature, measured by the vibrating sample magnetometer in PPMS. The central slope of the magnetic hysteresis curve gives a relative permeability of 1.09 for the magnetic cement, as we used previously in the simulations. The surface crack (h_2 = 0) case is realized by embedding a square-shaped plastic rod into the magnetic cement. Relevant works in the literature typically use similar volume fractions of magnetic particles in cement (4%), larger values of cement permeability (above

1.25), or wellbore structures with big cracks (10 to 20 cm)[136]. Instead of that, our experiment has focused on small crack sizes and a more reasonable permeability.

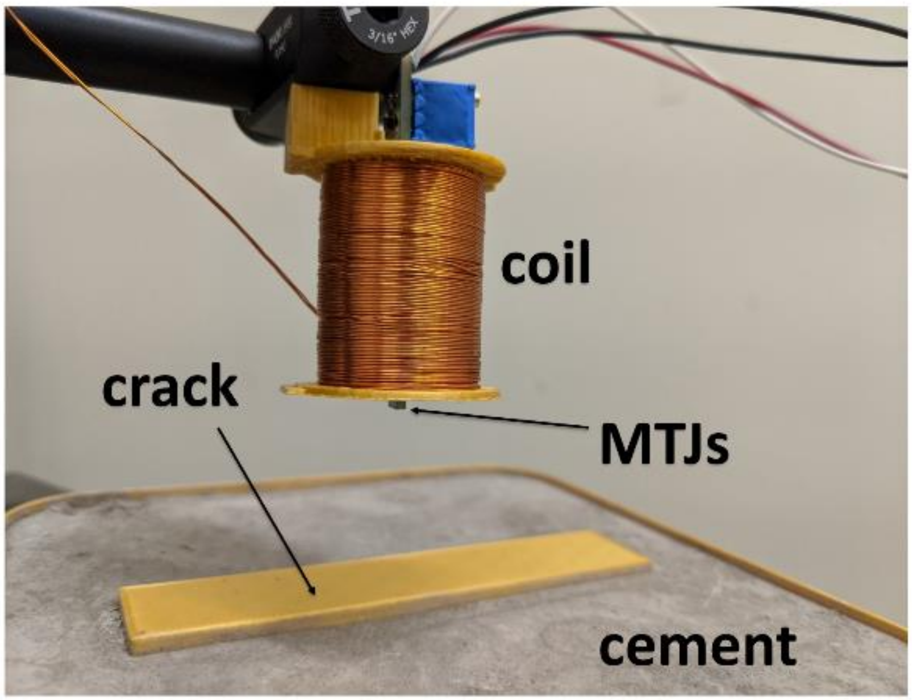

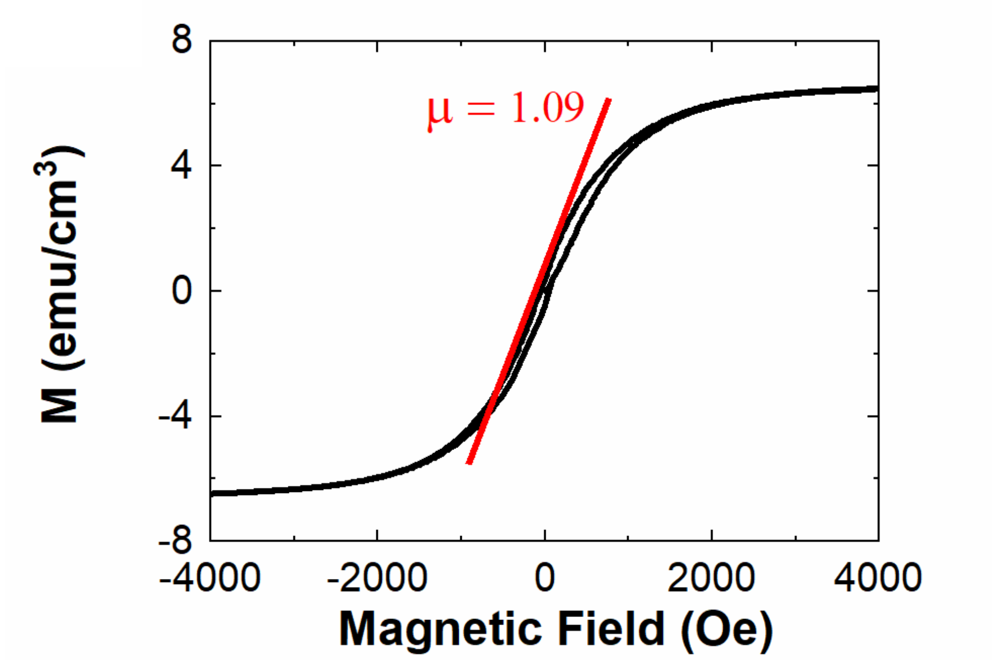

Figure 7. 10 Experimental setups to detect an artificial crack in the cement using our gradiometer enclosed by the excitation coil. The tip of the gradiometer at the center bottom of the coil is visible (left); Magnetic hysteresis loop of the magnetic cement mixed with small ferromagnetic Fe_3O_4 particle (right).

The iron powder in the impregnated cement has shown a negligible impact on overall mechanical behavior as we observe during experiments. The top diagram in Fig 7.11 below shows the 5-second averaged signals during a point-by-point scan across the crack, with a 300 μV voltage fluctuation observed as error bars. Considering the gradient field sensitivity D = 1000 V/T mentioned in section 7.3.1, the corresponding differential field $\Delta \boldsymbol{H_Z}$ is also calculated with an equivalent error bar of $\Delta \boldsymbol{H_Z}$ = 300 nT. In the diagram, a clear signal change is observed when the probe moves right above the crack at S = 0 position since the crack breaks the homogeneous magnetization of the cement resulting in a magnetic field change. The probe is capable of detecting a 2 cm wide surface crack from around 22 mm high above, since the signal change is still discernible near such standoff distance. 22 mm measuring distance is also consistent with our previous simulation by the end of section 7.3.2, indicating a maximum standoff distance around 2 to 3 cm.

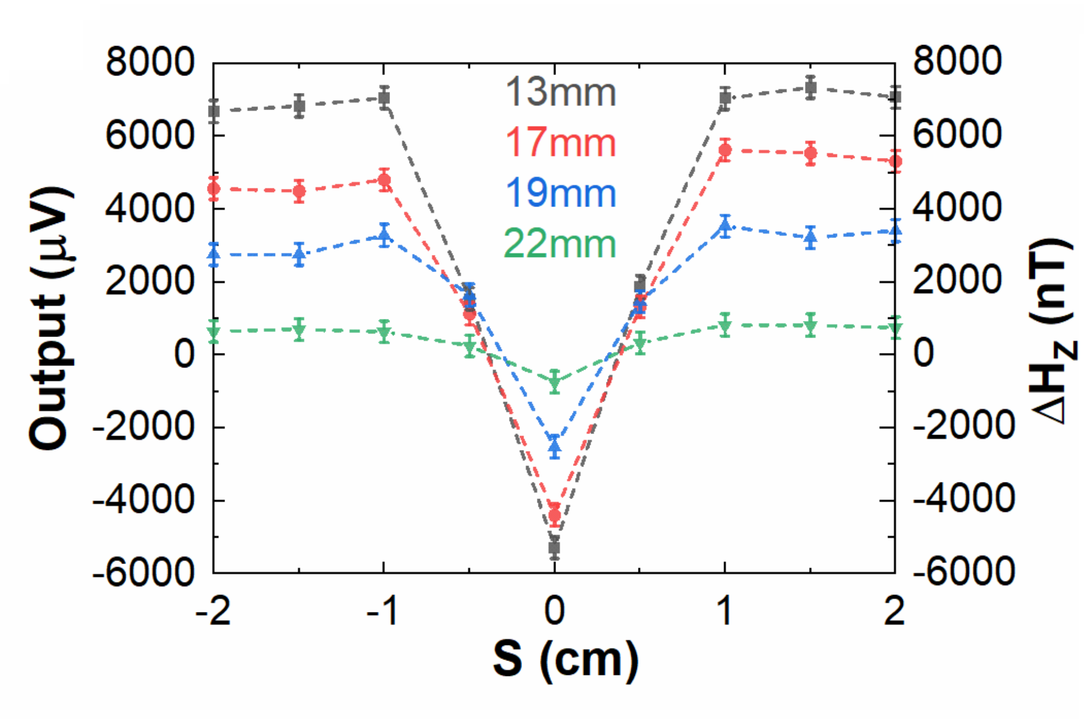

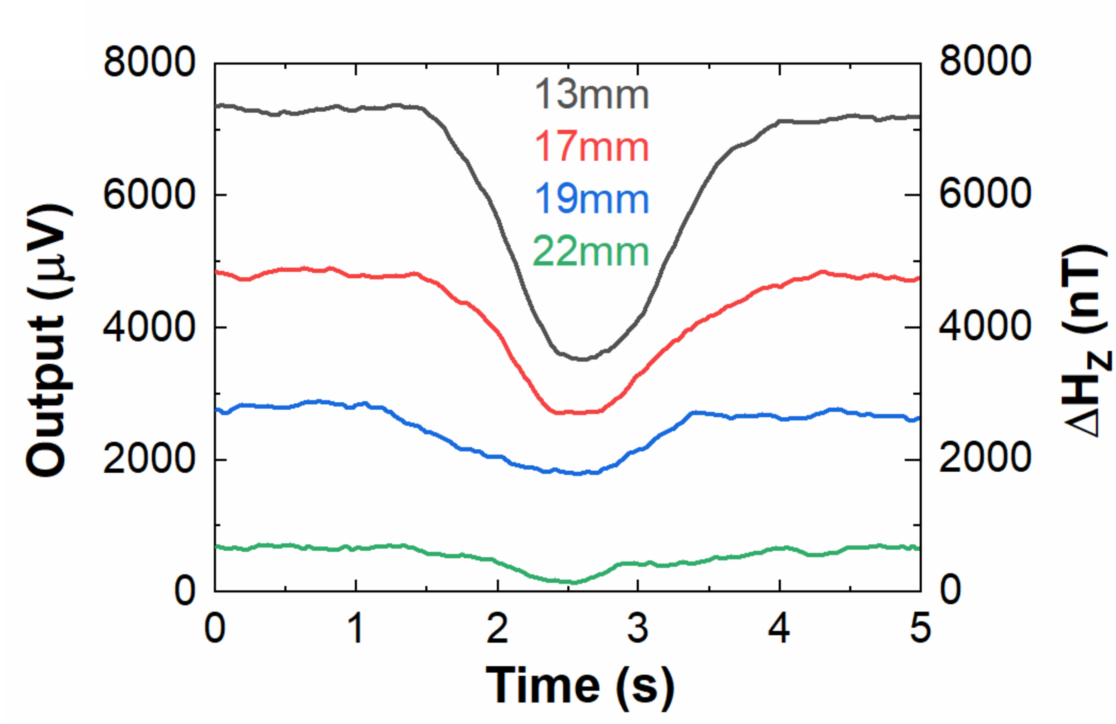

Figure 7. 11 The experimental voltage output of the gradiometer with 5-second averaging (left axis), and the deduced magnetic field ΔH_Z generated by the "crack" (right axis) are shown in the top figure. The bottom figure shows similar results but is measured in a continuous scan at a 2 cm/s scanning speed without time averaging. In both figures, the gradiometer scans at 13, 17, 19, 22 mm standoff distance above the "crack", and ΔH_Z is calculated by the previous mentioned sensitivity $D = 1000\ V/T$.

The previous scan with a 5-second averaging time is rather static. To test the response speed of the gradiometer for application purposes, we have moved the gradiometer across the crack in the cement while recording the signal continuously, as shown in the bottom of Fig 7.11. The moving speed is roughly 2 cm/s, and the standoff distances still vary from 13 to 22 mm. The presence of the crack is visible at all four distances tested, confirming the practicability of this method in crack detection. Nevertheless, the peak height is smaller than that of the static measurement, and this effect is due to the large time constant of the lock-in amplification which limits the signal slew rate.

To further improve the detectable limit, the signal can be enhanced by increasing the relative permeability of the magnetic cement or generating a stronger excitation field. Noticing that with the excitation field and the lock-in amplifier, the 300 nT fluctuation is significantly larger than the intrinsic sensor noise 1.6 nT/√Hz at 1 kHz in Fig. 7.3, considering a 1 Hz bandwidth of our DAQ. One possible origination of the extra noise is the electromagnetic interference from the excitation coil at the excitation frequency, which may be suppressed by better circuitry isolation. Also, the large current in the excitation coil causes Joule heating which increases current fluctuation. If the extra noise issues can be solved, the detection limit could reach 1.6 nT. Such detection limit in the intercept of the fitting in Fig. 7.7 (bottom) implies an enhanced standoff distance of 7 cm.

The spatial resolution of this probe is mostly limited by the working principle of MFL, where the gradient field is contributed by a large magnetic region instead of the local crack itself. As shown in Fig. 7.9, a smaller coil doesn't help with the FHWM. A smaller coil just results in a decrease in the signal peak, because in this configuration the magnetic fields are more concentrated near the coil, instead of penetrating the cement below it. For smaller cracks, we see a correspondingly smaller FHWM, but the decrease in FHWM is not proportional to the decrease in the crack volume. This suggests that such MFL configuration is in principle not suitable for detecting tiny cracks, and performs best with a centimeter spatial resolution.

In brief, this prototype gradiometer has proven its viability and superiority in the task of MFL crack detection, for oil well inspection in the energy industry or other applications. There is still much room for modifications and further enhancement, to broaden the range of non-destructive evaluation into more infrastructural systems or other kinds of cracks.

Chapter 8 Conclusion

In the search for the ideal sensor for magnetic field detection, our study focuses on the improvements in the sensitivity, hysteresis, and field detectability of magnetic tunnel junctions (MTJs). MTJ as a type of magneto-resistance device has been widely applied in field sensors or biomedical imaging, with its bright features such as large signals, low power consumption, complementary metal-oxide-semiconductor (CMOS) capabilities and so on. This study presents methods such as the magnetic flux concentrator (MFC) and perpendicular magnetic anisotropy (PMA) to modify the MTJ sensitivity. Different physical mechanisms such as superparamagnetism and vortex states are incorporated into MTJs for hysteresis elimination. These results could provide insights into the realization of low magnetic field detectability and the principle of designing a good magnetic sensing device.

With the help of MFC, we can boost up the signals from MTJ by a design of two-stage concentration. We improved the magnetic property of MFC through the use of CoZrNb alloy. With many iterations in the magnetron sputtering conditions, the material is tuned to its most amorphous condition exhibiting high permeability and small coercivity. Such magnetically soft material can concentrate external magnetic flux with high efficiency and be deposited close to the MTJ with a micrometer separation distance. It provides a high signal amplification factor of 16.8 on a chip-scale. The overall two-stage concentration design enhanced the sensing performance of MTJ with a detectability of $30\mathrm{pT}/\sqrt{\mathrm{Hz}}$ at 10 kHz.

To reach a low detectability, we also improved the MTJ layer composition by inserting several buffer layers such as CoFe, to prevent the diffusion of elements like Boron or Manganese. The tunneling magnetoresistance ratio (TMR) increased from 70% to 120%, as a sign of improved junction quality.

In our detailed characterization of magnetic sensors, the magnetic hysteresis turns out to be a practical issue that is ignored in the literature. It severely limits the sensor sensitivity for low-field measurements. To address this issue, we first resorted to the superparamagnetic free layer. We adjusted the layer stack of MTJ to observe a ferromagnetic-superparamagnetic transition with increasing temperatures. MTJs can be well-linearized with zero hystereses in the superparamagnetic state. The sensor noise is characterized at different temperatures, and two scaling relations between sensitivity and noise are revealed. Superparamagnetic state turns out to be superior to ferromagnetic with a linear scaling relation, but insufficient temperature stability.

Considering the shortcomings of superparamagnetic MTJ, we continued developing another method for hysteresis elimination by using vortex magnetization. Such magnetization is first found in our micro-magnetic simulations for the MTJ free layer disks of different shapes. Due to the competition between the demagnetization energy and exchange energy, the generation of a single vortex magnetization or other configurations such as double vortex and anti-vortex can be realized. After comparing their magnetic properties, we decide to use single vortex magnetization in our MTJ free layer experimentally. Due to the topology in vortex magnetization, the single vortex magnetization is free of any hysteresis with a large saturation field, which serves perfectly as a field sensor. As a result, we obtained an MTJ with zero coercivity and an extensive dynamic range. It has an unprecedented dynamic reserve of 115 dB, and high-temperature stability better than superparamagnetic MTJs. In addition to a great non-hysteretic sensor, we also obtained more insight into the noise scaling law. It is found that the vortex sensor can show a linear scaling relation between noise and sensitivity only in the non-hysteretic part of its transfer curve. The rare appearance of linear scaling in the vortex state and our previous superparamagnetic state exemplified the significance of eliminating hysteresis. To realize such a desirable scaling relation for sensing purposes, we can claim that a general prerequisite is to make the system non-hysteretic or thermally reversible.

Meanwhile, we have enhanced the sensitivity by the manipulation of magnetic anisotropy in our MTJ system. A new layer stack is designed, which effectively induces interfacial PMA in the free layer. Several fabrication parameters are capable of tuning the PMA strength to the desired value. Detailed relation between the PMA strength and the sensitivity is revealed by a temperature scan. A compensated anisotropy between PMA and in-plane anisotropy is realized to enhance the sensor sensitivity from 0.1 to 1.2 %/Oe. Such a method in MTJ can be a general method to enhance the response of a magnetic sensing device. Moreover, a voltage-related random telegraph noise (RTN) is found in such MTJ at its saturation condition, explained by a generation-recombination (GR) process and Fermi level shifting. The clear two-level fluctuation signal in this RTN can be potentially developed into random number generators.

Finally, a magnetic gradiometer for practical wellbore crack detection is developed with the vortex MTJ sensor. This productized sensing prototype is integrated with MTJ sensors and the necessary signal conditioning circuits on a printed circuit board, communicating with a computer through the LabVIEW program. We placed it into cement crack detection experiments based on the COMSOL simulation to measure a nano-tesla field from cracks on a piece of magnetic cement. In the demonstration, the prototype performed well to detect a 2 cm crack on a weakly magnetized cement at a large stand-off distance above 2 cm. It demonstrated the effectiveness of our sensor in practical application and guided general MFL testing designs. Every experimental parameter in the demonstration is based on practical industrial considerations, as this probe is designed to provide a ready solution for the wellbore inspection in the oil exploitation industry.

Conclusively, the sensitivity of MTJ is studied and improved by the methods of MFC and PMA; we also used superparamagnetism and vortex magnetic states to eliminate the magnetic hysteresis, as a critical issue for reaching ultralow field detectability. As discussed in previous chapters, these methods have shown their advantages in the low-field detectability of $30\mathrm{pT}/\sqrt{\mathrm{Hz}}$ at 10 kHz, the non-hysteretic behavior, or the high sensitivity above 1.2%/Oe. Results from this research serve the goal of making ultrasensitive magnetic sensors with MTJs.

Appendix

Oxidation furnace baking operation manual

1. In the furnace temperature controller, set the middle temperature controller to be 1150℃ (three values should all change).
2. Over the flow rate controller, there is a row of gas valve switches, make sure the second one from the left for Nitrogen is open; the flow rate reading (indicator"△" to "Oxide purge") shown on the right screen should set to be near 0.225 (reading 0.012 for no flow).
3. Turn off the Nitrogen switch, and press the second button from the top in the flow rate controller "Oxygen Dry/wet 5L/M" to release Oxygen. The Oxygen rate should be set as 0.5 LPM on the left screen (left screen: Ch2 M=.500LPM; right screen: 0.012≈0). When "O2 A=.500" is achieved on the left screen, the furnace is ready. After 30mins the temperature achieves the needed value for oxidation.
4. Wear rubber gloves, and load the sample into the furnace like Figure 2.1; make sure the sample stays in the middle of the furnace (view from the side);
5. Wait for 24 hours; Take out the sample and set everything back; Leave Nitrogen gas open for tube cleaning.

Below is a sketch of the handling method of our furnace and detailed instructions.

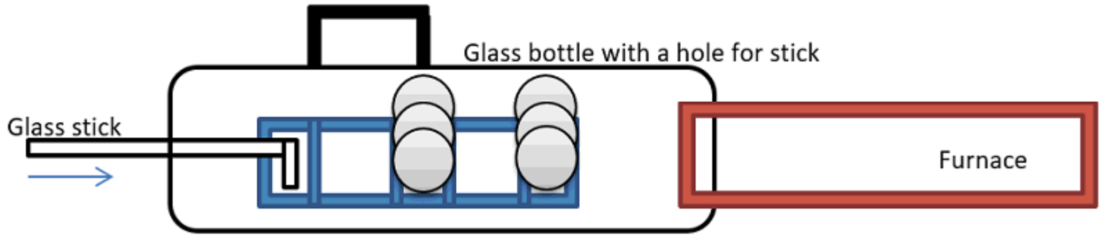

Figure A. 1 Furnace loading schematic diagram.

Old sputtering system operation manual

For the old sputtering system, never sputter all samples at one time, since the sample rotation started by Labview is unstoppable until finished. In case unwanted sputtering starts, turn off plasma and wait for the program to finish. If plasma fails to generate, use a lower gate valve angle or generate plasma by nearby targets first. If there is no plasma or no cooling water, the power dumped on the gun would be too much to break its magnetic field distribution. If the computer reboots, to use the Labview program user needs to first enter “windows XP mode”.

An operational manual is given here for the old sputtering system, and an operation panel diagram:

1. Turn on the Baratron gauge by the button “IG2”, let it “Degas” for 1 min, and then record the ion gauge pressure reading. The first line shows the ion gauge reading for the chamber, the second line for the cryopump, third line for another rough chamber pressure reading from the Granville gauge. Make sure the temperature reading of cryopump is below 20K, or the pump needs regeneration purge.

2. At the bottom left of the front panel as shown in the figure, rotate the big black switch bar first so it's in parallel with the arrow label, then rotate each small green switch above it. If the cooling water starts to flow, the pipes behind should flicker each time a green bar is quickly rotated.
3. Open the gas tank on the left so it provides gas pressure for solenoid to operate (70 psi needed); Open the solenoids at the top left of the front panel ("CH1 Argon") to let in the gas needed for sputtering plasma generation.
4. Connect two wires on the top lid of chamber, plug them into the power outlet on the wall. Therefore the rotator is powered on.
5. Set the gate valve angle from 90 degree to near 30 degree; the lower angle the higher chamber pressure.
6. Turn on the flow rate controller "Type 247 4 channel" so its reading stabilizes to 0 after a while; Turn on the gas switches on the flow rate controller. Use the setting of "22.5sccm Ar" for general deposition and "25 sccm O2, 65 sccm Ar" for SiO2 sputtering; at present channel 2 is O2 and channel 4 is Ar.
7. Open the N2 tank on the further side, set its pressure corresponding to the shutter to be used, and manually test if the shutter moves smoothly. Each shutter has a label indicating the proper pressure.
8. Turn on the sample holder rotation via "bottom motor on/off" knob. Check the rotation condition of every sample holder on the top.
9. Check the wire number underneath the sputtering gun that is going to be used, then turn on the corresponding power supply; Two DC powers have switches on their rear side and knobs on front side to choose the wire that the power is delivered to; To use RF power, press the red button, set the regulator on top to be

around “0.3, 0.7” for manual setting, then press start; Turn the regulator to “Auto” after plasma successfully generates.

10. During 5-10 min pre-sputtering with identical condition of actual sputtering, use Labview program “system initial” to adjust the round sample holder position so that the number one sample holder is closest to the front window panel; Align the mark line on the window, the main rotation rod in the center of chamber, and the center of the number one sample holder to be overlapping. Press “set variable” button when they’re aligned. If the main rotation gets stuck, try to reconnect the two wires on the chamber lid and rotate in bigger steps like 200. “material info” sub VI can be used to change sputtering rate recorded for Labview.
11. Use “new multiple layer cluster 6.vi” to start sputtering; the program would calculate the sputtering time from the power and thickness entered; After sputtering, close everything and let the chamber cool down for 1.5 hour.

If the cryopump is not working normally, then regenerate operation is needed:

1. Turn off the cryopump compressor, close the gate valve, open the purge gas (the same tank to purge chamber), and turn on “purge heat” toggle switch.
2. During N2 purging, the gas line will be hot and the output gas will spray near the rubber ring. Purge 2.5 hours with flow rate around 60, about 2000 psi N2 would be consumed.
3. Open the gate valve to let rough pump evacuate the cryopump together with the chamber to 1.5e-1 torr. Now turn off rough valve, close the gate valve, and check if the pump can pass the “ROR” test, which is that the pressure doesn’t go above 2e-1 after 5 mins. Open the compressor, in 2.5 hours the pump should reach low working temperature near 10K.

New sputtering system operation manual

Below is the operational manual for our new sputtering system, which is more automatic compared to the old sputtering system:

1. Close the valve on the wall for the school gas pipeline (mutually perpendicular position) which is used to provide the pressure holding the gate valve open; open the nearby gas tank that provide pressure to hold/close the gate valve (65 psi pressure required); use the black outer rotary knob instead of the one on top of the tank.
2. Using VI "Write Dig Chan PCI 6515" to close the gate valve (button 7.3), then use Nitrogen in the other tank to vent the chamber by opening its two switch.
3. Close venting gas switch, place on samples after chamber open, tighten loose shutters (especially MgO shutter) by screwing up two screws on the coupler; then close the chamber, making sure the shaft from top fits into the pole in the bottom of chamber.
4. Evacuate the chamber by the VI used above: open mechanical pump(6.1), open rough valve(7.2) to 80 mtorr; close these two and open gate valve for cryopump to work, with gate valve angle 100 degrees. Close the tank providing gas pressure and use the school gas pipeline again. In one day it should reach 2e-8 torr, which can be read in VI "High vacuum Pressure Indicator_ion gauge".
5. Change from school gas to the gas of our lab to control gate valve, also open Argon gas and shutter gas on the other side of chamber (10 psi). Use VI " Labview-02-presputter" to do pre-sputtering: Set "Ion gauge min" to be 0.2. After the program starts, observe first a "zero" message which reads the pressure before Argon enters the chamber, usually -0.22; When "Baffle valve closed" message appears, set gate

valve angel 20 and fix it there; after all green lightbulbs on, click “Set stepper variable” button if the number one sample is placed near the front window. During pre-sputtering observe every eight minutes whether the plasma is generated successfully, and whether the shutter moves freely; if not repeat the pre-sputtering.

6. For pressure monitors, on the top of chamber is the Baratron gauge reading sputtering pressure; The Convectron gauge reads rough atmosphere pressure, and the ion gauge reads base pressure after evacuation. Use VI “Labview-03-Deposition-test-MgO-thickness” to start sputtering. When finished, run “Labview-04-venting” to close everything, then open gate valve (7.3). Bright green light means one corresponding switch is open.

The regenerate operation for this device is different from the old sputtering system as below:

1. Close gate valve, turn off the compressor power under desk. In the small grey control panel on the right side of cryopump, press “Regenerate” then “1”, “2”. It will show “cryo off”, “warm up”, and “Ext purge xx” in a sequence where “xx” is usually set as 40 minutes. Open the purge gas and the gate valve control to start the regeneration.
2. After regeneration it goes to “Rough 999/50”, when the mechanical pump needs to be manually turned on to evacuate the cryopump. Then it will try to pass “ROR #1” test 6 times to check the air tightness of the pump. Finally it begins to cool down with message “cool 309/14 K”. The mechanical pump should be closed now, and within 2 hours it will show “complete”. Press “Monitor” to return to its normal working state.

As for the Labview controlling programs, in “Labview-02-presputter”; “Rotations” is the rotation times for the central axis which is usually 34. The “time” setting for each row of pre-sputtering materials are 8 minutes and there are 4 rows of them; the total running time thus need to be set more than 32 minutes. "P_{set}" is the pressure reading. IrMn will help create plasma for MgO. In "Labview-03-Deposition-test-MgO-thickness", "Si" is meant for MgO. The DC power needs to be set manually. Before every MgO sputtering a target pre-sputtering is executed, and "MgO Rotate" sets the central axle rotation times for this pre-sputering process. We can change the gate valve angle during sputtering to modify the sputtering pressure, or change the "Baratron" set value.

Photolithography operation manual

1. Before any operations in the ultra-clean room, the samples taken from outside need to undergo a cleaning sequence of using Acetone (cleaning PR, rubber, plastic, and other organics), Methanol (cleaning organics), IPA (isopropyl alcohol, cleaning grease) and deionized water. For each procedure samples need to be rinsed in the corresponding solutions and sonicated for 3 to 10 minutes, until they look clean and smooth under microscope. For persistent PR residues, soaking the sample in AZ400T solution and sonicate at 80℃.
2. The spin coating device is used to spread a layer of PR onto the clean sample. Load on spin head, set in "program 1" a rotation speed of 4000 rpm, a rotation acceleration of 4000 rpm/s, rotation time 30s, corresponding to a PR coating of 1.2 ± 0.2 μm. Open the main gas switch on the top of the experiment table, enabling spin head to vacuum the sample. Place the sample and adjust its position, click "Run" to run program 1. Click "start" and "0" several times to make the sample centered on the spin head. Take a pipette and use the airbrush to clean its

inner surface. Use the cleaned pipette to drop PR onto the sample uniformly. Close the lid and press “start”.

3. The photoresist on samples is not robust after spin coating, and it requires further baking. There are positive and negative patterns, each requires different baking and UV light exposure conditions.
4. For positive patterning, put the temperature measuring wire between the iron plate and the heater, and set the heater 110℃. When the temperature is stable, put the sample on the iron plate right after spin coating. After baking for 2 minutes, take the sample and put it in a light-proof box. The corresponding exposure time is 22 seconds. With positive patterning, the area exposed to UV light will remain.

   For negative patterning, bake the PR at 100℃ for 2 min, expose for 6 seconds, bake again at 145 ℃ for 1 minutes, and expose again without any mask for 1 minutes. With negative patterning, the area exposed to UV light will be removed.
5. After baking the samples can be loaded for UV light exposure. On the control table of photolithography, open two rotary knobs under the table, “N2 Purge” toggle switch on the front side of table, two toggle switch of the upper gas controller on the table, a toggle switch on a small white box on the left for microscope light, and etch light control box on the left. For the last one, press “start” after “Ready” message appears, and make sure the power shown afterwards is near 270 watts. Make sure the lens we use are of wavelength “365nm” instead of “404nm” and we are using a transparent filter. The typical UV light dose is 200 mJ/cm^2, and “defoc” value -3. Place the mask on the glass

plate, press button “vacuum mask” and load the mask in. The mask is designed to block UV light at certain positions of the sample, so that a pattern is left on the sample after exposure. Stick the sample on its plate with water drops and load it in.

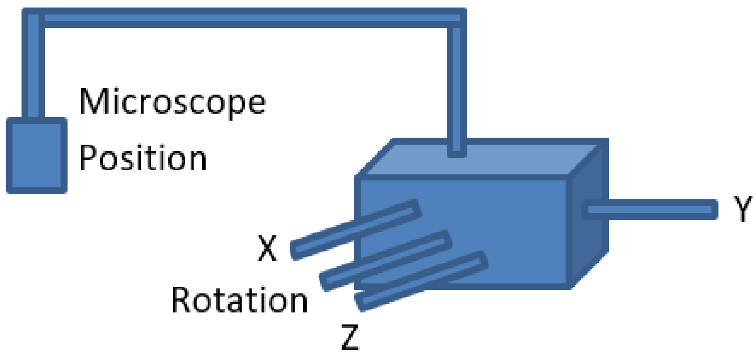

Figure A. 2 The schematics of our photolithography control bars and their functions.

6. Pull back a rod on the left side of the lithographer to reach “separation” light from “contact”. Lower z coordinate (clockwise, z is vertical coordinate) so that the rotary rod adjustment doesn’t elevate the sample to press the mask. When the sample is close to the mask, start alignment in microscope. Use rotation to align the cross mark, then use X, Y controls to align other pattern. After alignment, maximize z coordinate until many diffraction fringes show up on the mask. Switch back to “contact” light. Set the lithography time on the right dial plate, where “△” lable indicates the unit time. Press the button “Vacuum chamber”, then press “Exposure” to start the procedure. Don’t watch the lithographer during

the process which is hazardous to eyes. When finished, Lower the sample using "Z" and "rotation" rods to retrieve the sample.

7. Soak the sample in PR developer AZ917, open deionized water faucet, and start timer counting. After rinsing the sample for 20 to 50 seconds, the PR coating in expected region should be observed to disappear. Persistent rremnant PR of irregular shapes can be removed by cotton tips brushing. Flush the sample under the faucet and the patterning process is finished. When leaving, long press "DS" button of the etching light control box to record the filament time; Leave two rotary knobs under the table, "N2 Purge" toggle, two toggle switch of gas controller open for 15mins to cool down the lithographer.

Maskless Aligner operation manual

We also have a commercial mask-less aligner (MLA 150) photolithography device from Heidelberg Instruments, with a high spatial resolution of 2µm, whose operation manual can be found online. The dose of laser exposure and the time of subsequent developing can be different, so testing photolithography needs to be done beforehand. It performs photolithography patterning automatically after loading the sample, and the virtual mask can be designed by software like AutoCAD. In AutoCAD, the mask design is better saved as "dwg" file for frequent editing, and as "2013 dxf" file to upload into MLA. "R12 dxf" file type is more compatible but the file size is significantly bigger. For consecutive patterning process as used in MTJ fabrication, it is advisable to create a single file with each patterning mask as one layer, without any elements crossing different layers. To create markers with known coordinates in the mask file is the easiest way to align the sample under MLA microscope, otherwise the alignment needs to be done by manually inputting coordinates of at least two points on the loaded sample. Double-sided adhesive tape can always be used for sample loading, when the vacuum suction has insufficient pressure. Don't use the inbuilt "Automatic Centering" function of MLA when you have multiple levels to align which causes misalignments. You should instead set up your file such that the center of the CAD file is at the center of your design. Always use the microscope and the step profiler (Dektek device) to check and confirm the morphology of the samples. For example, check the PR residue, sample cleanness and etching depth before next photolithography, or check the PR shape and height after the photolithography.

Ion milling maching operation manual

Detailed operational manual for our ion milling machine is given below:

1. In the front panel, use "vent" toggle switch to vent the chamber with Nitrogen gas. Load samples onto the rotator, with clean gaskets and dummy samples so that all base part is covered from being etched. Close the chamber and lock it using the lever on top. Make sure different samples are distinguished by their loading positions.
2. Turn on "Rough" switch to pump the chamber pressure to 100 mtorr. Close "rough" valve and open "Hi" valve to let cryopump evacuate the chamber. Push down the toggle switch for "Vaccum gauge" to read in the correct range. Its pressure should reach 2×10^{-6} torr after 1 hour.
3. Open cooling water switch and turn on DC power supply to 22 volts, for the cooling and rotation of samples. Open argon gas flowrate controller with flow rate setting 40 sccm; after flow rate shown on the controller stabilize, switch from "close" to "Auto"

label. After a while the pressure meter should switch measuring range to 10^{-4} torr. Adjust the flow rate manually to set a working pressure of 1.6×10^{-4} as usual.

4. Turn on ion milling power by pulling the triple throw switch near “milling control” to “man”. Turn on “neutralizer” in the bottom crate to adjust the “Ion current” value to 0 for neutralization. With neutralizer turned off, rotate the knob of the “Source” label to adjust the ion current to a normal value 0.142. Repeat these two adjustments until the ion current gets stable.
5. With neutralizer on, start timing and rotate the lever on top of the milling chamber to open the internal shutters, which starts the ion etch process. Change the ion milling angle by the lever on the right side of chamber if needed. Record readings on all electronics on the crate simultaneously.
6. Pull the triple throw switch to “Off” when the etching is finished. Close everything and push up the toggle switch for vacuum gauge. Wait for 1 hour for system to cool down.

For cryopump regeneration, it is basically the same as the old sputtering cryopump, but without gas heater. Use the switch on the compressor or the “HI vac” button the crate to turn off the compressor of the pump. Use the key near the “HI vac” button to switch the system state from “cryopump on” to “normal”, so the purging process starts with power off. When purging is done the compressor could be turned back on after cryopump evacuation. After 6 hours the thermometer reading should decrease below 20K as a sign of completion.

Magnetic field assisted thermal annealing operation manual

1. Clamp the sample with the correct annealing direction on the metal plates, and gently load them into the cube metal container inside the chamber. The copper container is between two strong permanent magnets, so be aware not to let anything magnetic gets close. Use screwdriver rod to close the container after loading.
2. Close the venting hole on the left side, open the power of mechanical pump behind the chamber, and turn on the front rotary knob to begin evacuation. Keep pressing the front gate for half a minute for a good sealing vacuum condition. In 5 minutes it should reach below 10^{-3} torr.
3. Turn off the front knob to close the gate valve of mechanical pump, but keep the mechanical pump running for cooling water circulation; Turn on the rear knob to open gate valve of the turbo pump. Turn on the turbo pump. When the "stop" light is on, press "start" button. Open the green pipeline valve on the wall for cooling water. In 10 minutes with turbo pump evacuation it should reach below 10^{-6} torr. The normal gauge has a lowest reading of 10^{-3} torr; to measure below that, use the ion gauge and degas for few seconds to read the precise pressure.
4. Set up the annealing temperature controller. Press the most left of the four square buttons to go to "ProG" menu, then use the second left one (arrow sign) to set up the whole temperature varying progress. Set "CYC" (cycle) to be 1, then set parameters for each "Sec" (section). "Type rmP.E" (ramp) is the section for temperature ramping up, followed by the setting of expected temperature. The time it spends at that temperature is set by section "during". Each temperature ramp should be followed by a "Type dwell" section, during which temperature will be held fixed. All the units are in minute. Set the final step to be "Type:end" followed by "end-stop". A usual temperature ramping sequence is like 0-150-235-280-300-310-315-320°C, and the

"ramp" and "during" time is 20-10-10-5… Usually it stays in the final temperature for 1 to 4 hours. Press the button "Run" to start.

5. When the annealing is finished, press and hold the button next to "Run" until the light goes off. There are two temperature readings in the panel, the upper one is the temperature inside for the time being, and the lower one is the highest temperature reached during the whole annealing process. After the temperature cools down below 60°C, close turbo pump, and wait for 20 minutes. Shut down Mechanical pump and cooling water.

X-ray diffraction operation manual

1. Stick the sample onto the measurement area with double-sided tape. Check the beam slit, load the "0.2mm" size one for XRR and "1.2mm" one for XRD. Larger slit receives stronger signals but less angle resolution.
2. Open the program "Diffraction measurement". Click on "File", go to "Application", and set "high resolution". Click "Commander", then "Pathfinder", in "Varslit" set the voltage to be 40 and current 40. Click "set" in "X-ray". In "Detector" choose "Scinti" for XRR, or "LYNXEYE (0 mode)" for XRD.
3. Set all values above "Primary Rotary Abs" to be 0. Set "Primary Rotary Abs" to be 58.22, "Detector Slit" to be 2, and "Pathfinder" 2. Click "=3,45" to confirm all values.
4. Choose "scan type" to be "Z", which scans to find sample position. Set "Time" to be 0.1s and total 15s. Set scan range between 0 and 1.5 radius with 0.02 as scan step. Start Z scan and double click the middle point of the resultant curve.

5. Change “scan type” to “Rocking curve” to measure the sample inclination. Set “omega” from -1 to 1. Start the scan and double click the peak position of the resultant curve.
6. Repeat previous Z scan one more time.
7. For XRR, repeat Rocking curve scan one more time with “Theta 2-H” value 0.5.
8. Set “Primary Rotary Abs” to be “Auto”. For XRR set “Detector slit” to be 0.2 and “Path finder” 0.2; For XRD set both values to be 2, and “Detector” to be “LYNXEYE (1D mode)”. Set “Scan type” to be “2 Theta-omega”.
9. Start the main scan, usually a rough scan to find the angle region of information; in the following fine scan set “Time” to be 0.2s, “2 Theta” scan step to be 0.005 radius. View the result in log scale and save it as “v4 file.raw”.
10. Use software “File exchange” to exchange the v4 file into txt file. Restore all previous settings of X-ray device to initial values and log off.

Bibliography

[1] K. Tsukada, Y. Haga, K. Morita, N. Song, K. Sakai, T. Kiwa, and W.Y. Cheng, IEEE T MAGN **52** (7), 1 (2016). "Detection of Inner Corrosion of Steel Construction Using Magnetic Resistance Sensor and Magnetic Spectroscopy Analysis"

[2] M.H. Acuna, Review of Scientific Instruments **73** (11), 3717 (2002). "Space-based magnetometers"

[3] M. Pannetier-Lecoeur, L. Parkkonen, N. Sergeeva-Chollet, H. Polovy, C. Fermon, and C. Fowley, Applied Physics Letters **98** (15), 153705 (2011). "Magnetocardiography with sensors based on giant magnetoresistance"

[4] E.Y. Tsymbal and I. Zutic, *Handbook of spin transport and magnetism*. (CRC press, 2011).

[5] M. Julliere, Physics letters A **54** (3), 225 (1975). "Tunneling between ferromagnetic films"

[6] C.H. Tsang, R. Fontana, T. Lin, D.E. Heim, B.A. Gurney, and M. Williams, IBM journal of research and development **42** (1), 103 (1998). "Design, fabrication, and performance of spin-valve read heads for magnetic recording applications"

[7] J.S. Moodera, L.R. Kinder, T.M. Wong, and R. Meservey, Physical review letters **74** (16), 3273 (1995). "Large magnetoresistance at room temperature in ferromagnetic thin film tunnel junctions"

[8] S. Yuasa, T. Nagahama, A. Fukushima, Y. Suzuki, and K. Ando, Nature materials **3** (12), 868 (2004). "Giant room-temperature magnetoresistance in single-crystal Fe/MgO/Fe magnetic tunnel junctions"

[9] T. Miyazaki and N. Tezuka, Journal of magnetism and magnetic materials **139** (3), L231 (1995). "Giant magnetic tunneling effect in Fe/Al2O3/Fe junction"

[10] J. Mathon and A. Umerski, Physical Review B **63** (22), 220403 (2001). "Theory of tunneling magnetoresistance of an epitaxial Fe/MgO/Fe (001) junction"

[11] W. Butler, X.-G. Zhang, T. Schulthess, and J. MacLaren, Physical Review B **63** (5), 054416 (2001). "Spin-dependent tunneling conductance of Fe| MgO| Fe sandwiches"

[12] S. Blakley, I. Fedotov, S.Y. Kilin, and A. Zheltikov, Optics letters **40** (16), 3727 (2015). "Room-temperature magnetic gradiometry with fiber-coupled nitrogen-vacancy centers in diamond"

[13] C. Affolderbach, M. Stähler, S. Knappe, and R. Wynands, Applied Physics B **75** (6-7), 605 (2002). "An all-optical, high-sensitivity magnetic gradiometer"

[14] M.E. Huber, N.C. Koshnick, H. Bluhm, L.J. Archuleta, T. Azua, P.G. Björnsson, B.W. Gardner, S.T. Halloran, E.A. Lucero, and K.A. Moler, Rev. Sci. Instrum. **79** (5), 053704 (2008). "Gradiometric micro-SQUID susceptometer for scanning measurements of mesoscopic samples"

[15] D. Sheng, A.R. Perry, S.P. Krzyzewski, S. Geller, J. Kitching, and S. Knappe, Applied physics letters **110** (3), 031106 (2017). "A microfabricated optically-pumped magnetic gradiometer"

[16] J.M. Merayo, P. Brauer, and F. Primdahl, Sensors and Actuators A: Physical **120** (1), 71 (2005). "Triaxial fluxgate gradiometer of high stability and linearity"

[17] D. Ménard, G. Rudkowska, L. Clime, P. Ciureanu, A. Yelon, S. Saez, C. Dolabdjian, and D. Robbes, Sensors and Actuators A: Physical **129** (1-2), 6 (2006). "Progress towards the optimization of the signal-to-noise ratio in giant magnetoimpedance sensors"

[18] M. Janošek, A. Platil, and J. Vyhnánek, IEEE T MAGN **51** (1), 1 (2015). "The effect of sensor size on axial gradiometer performance"
[19] P. Ripka, M. Tondra, J. Stokes, and R. Beech, Sensors and Actuators A: Physical **76** (1-3), 225 (1999). "AC-driven AMR and GMR magnetoresistors"
[20] A. Guedes, R. Macedo, G. Jaramillo, S. Cardoso, P. Freitas, and D. Horsley, Sensors **18** (3), 790 (2018). "Hybrid GMR sensor detecting 950 pT/sqrt (Hz) at 1 Hz and room temperature"
[21] R. Popovic, P. Drljaca, and C. Schott, presented at the 2002 23rd International Conference on Microelectronics. Proceedings (Cat. No. 02TH8595), 2002 (unpublished).
[22] J. Daughton, Journal of Magnetism and Magnetic Materials **192** (2), 334 (1999). "GMR applications"
[23] M. Takagishi, K. Koi, M. Yoshikawa, T. Funayama, H. Iwasaki, and M. Sahashi, IEEE Transactions on Magnetics **38** (5), 2277 (2002). "The applicability of CPP-GMR heads for magnetic recording"
[24] P. Brown, B. Whiteside, T. Beek, P. Fox, T. Horbury, T. Oddy, M. Archer, J. Eastwood, D. Sanz-Hernández, and J. Sample, Review of Scientific Instruments **85** (12), 125117 (2014). "Space magnetometer based on an anisotropic magnetoresistive hybrid sensor"
[25] P.P. Freitas, R. Ferreira, S. Cardoso, and F. Cardoso, J Phys-Condens Mat **19** (16), 165221 (2007). "Magnetoresistive sensors"
[26] G. Bertotti, *Hysteresis in magnetism: for physicists, materials scientists, and engineers*. (Academic press, 1998).
[27] X. Yin, Y.-F. Liu, D. Ewing, C.K. Ruder, P.J. De Rego, A. Edelstein, and S.-H. Liou, presented at the Spintronics VIII, 2015 (unpublished).
[28] P.K. Amiri and K.L. Wang, presented at the Spin, 2012 (unpublished).
[29] Y. Lu, R. Altman, A. Marley, S. Rishton, P. Trouilloud, G. Xiao, W. Gallagher, and S. Parkin, Applied physics letters **70** (19), 2610 (1997). "Shape-anisotropy-controlled magnetoresistive response in magnetic tunnel junctions"
[30] M. Wang, Y. Zhang, X. Zhao, and W. Zhao, Micromachines **6** (8), 1023 (2015). "Tunnel junction with perpendicular magnetic anisotropy: Status and challenges"
[31] J.G. Alzate, P. Khalili Amiri, G. Yu, P. Upadhyaya, J.A. Katine, J. Langer, B. Ocker, I.N. Krivorotov, and K.L. Wang, Applied physics letters **104** (11), 112410 (2014). "Temperature dependence of the voltage-controlled perpendicular anisotropy in nanoscale MgO| CoFeB| Ta magnetic tunnel junctions"
[32] H.I. Smith, R.J. Aucoin, J.M. Carter, W. Chu, R.C. Fleming Jr, R.A. Ghanbari, N. Gupta, S.D. Hector, H. Li, and A.M. Moel, 1992.
[33] J. Nabity, JC Nabity Lithography Systems, PO Box **5354**, 1996 (1988). "Nanometer Pattern Generation System"
[34] Y. Zhang, G. He, X. Zhang, and G. Xiao, Applied Physics Letters **115** (2), 022402 (2019). "Magnetotransport and electronic noise in superparamagnetic magnetic tunnel junctions"
[35] G. He, Y. Zhang, and G. Xiao, Physical Review Applied **14** (3), 034051 (2020). "Nonhysteretic Vortex Magnetic Tunnel Junction Sensor with High Dynamic Reserve"
[36] E. Meyer, H.J. Hug, and R. Bennewitz, *Scanning probe microscopy: the lab on a tip*. (Springer Science & Business Media, 2003).
[37] C. Kittel, P. McEuen, and P. McEuen, *Introduction to solid state physics*. (Wiley New York, 1996).

[38] L.V. Azároff, R. Kaplow, N. Kato, R.J. Weiss, A. Wilson, and R. Young, *X-ray Diffraction*. (McGraw-Hill New York, 1974).
[39] M. Belmoubarik, H. Sukegawa, T. Ohkubo, S. Mitani, and K. Hono, Applied Physics Letters **108** (13), 132404 (2016). "MgAl2O4 (001) based magnetic tunnel junctions made by direct sputtering of a sintered spinel target"
[40] C.B. Duke, *Tunneling in solids*. (Academic Pr, 1969).
[41] J.C. Slonczewski, Physical Review B **39** (10), 6995 (1989). "Conductance and exchange coupling of two ferromagnets separated by a tunneling barrier"
[42] X. Zhang, B.-Z. Li, G. Sun, and F.-C. Pu, Physical Review B **56** (9), 5484 (1997). "Spin-polarized tunneling and magnetoresistance in ferromagnet/insulator (semiconductor) single and double tunnel junctions subjected to an electric field"
[43] X. Zhang and W. Butler, Journal of Physics: Condensed Matter **15** (41), R1603 (2003). "Band structure, evanescent states, and transport in spin tunnel junctions"
[44] S. Yuasa and D. Djayaprawira, Journal of Physics D: Applied Physics **40** (21), R337 (2007). "Giant tunnel magnetoresistance in magnetic tunnel junctions with a crystalline MgO (0 0 1) barrier"
[45] P. Bruno and C. Chappert, Physical review letters **67** (12), 1602 (1991). "Oscillatory coupling between ferromagnetic layers separated by a nonmagnetic metal spacer"
[46] W. Chen, L. Qian, and G. Xiao, Scientific reports **8** (1), 1 (2018). "Deterministic current induced magnetic switching without external field using giant spin Hall effect of β-W"
[47] C. Yoshida, T. Takenaga, Y. Yamazaki, H. Uehara, H. Noshiro, K. Tsunoda, Y. Iba, A. Hatada, M. Nakabayashi, and A. Takahashi, IEEE Transactions on Magnetics **50** (11), 1 (2014). "Reduction of Offset Field in Top-Pinned MTJ With Synthetic Antiferromagnetic Free Layer"
[48] Q. Ma, J. Feng, G. Feng, K. Oguz, X. Han, and J. Coey, Journal of magnetism and magnetic materials **322** (1), 108 (2010). "Annealing effect on tunneling magnetoresistance in MgO-based magnetic tunnel junctions with FeMn exchange-bias layer"
[49] S. Mukherjee, R. Knut, S.M. Mohseni, T.A. Nguyen, S. Chung, Q.T. Le, J. Åkerman, J. Persson, A. Sahoo, and A. Hazarika, Physical Review B **91** (8), 085311 (2015). "Role of boron diffusion in CoFeB/MgO magnetic tunnel junctions"
[50] H. Hosoya, Y. Nagamine, K. Tsunekawa, V. Zayets, and S. Yuasa, Applied Physics Express **6** (6), 063003 (2013). "Characterization of Ultrathin Fe–Co Layer Grown on Amorphous Co–Fe–B by In situ Reflective High-Energy Electron Diffraction"
[51] K. Tsunekawa, D.D. Djayaprawira, M. Nagai, H. Maehara, S. Yamagata, N. Watanabe, S. Yuasa, Y. Suzuki, and K. Ando, Applied Physics Letters **87** (7), 072503 (2005). "Giant tunneling magnetoresistance effect in low-resistance CoFeB∕MgO (001)∕CoFeB magnetic tunnel junctions for read-head applications"
[52] T. Musha, S. Sato, and M. Yamamoto, *Noise in physical systems and 1/f fluctuations*. (IOS Press, 1992).
[53] B. Kaulakys and T. Meškauskas, Physical Review E **58** (6), 7013 (1998). "Modeling 1/f noise"
[54] Z. Lei, G. Li, W.F. Egelhoff, P. Lai, and P.W. Pong, IEEE T MAGN **47** (3), 602 (2011). "Review of noise sources in magnetic tunnel junction sensors"
[55] Y. Zhang and G. Xiao, Physical Review B **100** (22), 224402 (2019). "Spin-dependent shot noise in MgO-based magnetic tunnel junctions under noncollinear magnetization alignment"

[56] T. Arakawa, T. Tanaka, K. Chida, S. Matsuo, Y. Nishihara, D. Chiba, K. Kobayashi, T. Ono, A. Fukushima, and S. Yuasa, Physical Review B **86** (22), 224423 (2012). "Low-frequency and shot noises in CoFeB/MgO/CoFeB magnetic tunneling junctions"
[57] R. Kubo, Reports on progress in physics **29** (1), 255 (1966). "The fluctuation-dissipation theorem"
[58] D. Des Cloizeaux, in *Theory of condensed matter. Lectures presented at an international course* (1968).
[59] L. Jiang, E. Nowak, P. Scott, J. Johnson, J. Slaughter, J. Sun, and R. Dave, Physical Review B **69** (5), 054407 (2004). "Low-frequency magnetic and resistance noise in magnetic tunnel junctions"
[60] S. Kogan, *Electronic noise and fluctuations in solids*. (Cambridge University Press, 2008).
[61] 2010 (unpublished).
[62] C. Rogers and R. Buhrman, Physical review letters **53** (13), 1272 (1984). "Composition of 1 f Noise in Metal-Insulator-Metal Tunnel Junctions"
[63] T. Kiyoshi, S. Choi, S. Matsumoto, T. Asano, and D. Uglietti, IEEE transactions on applied superconductivity **19** (3), 2174 (2009). "Magnetic flux concentrator using Gd-Ba-Cu-O bulk superconductors"
[64] A. Edelstein, J. Burnette, G. Fischer, K. Olver, W. Egelhoff Jr, E. Nowak, and S.-F. Cheng, Journal of Applied Physics **105** (7), 07E720 (2009). "Validation of the microelectromechanical system flux concentrator concept for minimizing the effect of 1/f noise"
[65] A. Edelstein, G. Fischer, M. Pedersen, E. Nowak, S.F. Cheng, and C. Nordman, Journal of applied physics **99** (8), 08B317 (2006). "Progress toward a thousandfold reduction in 1∕f noise in magnetic sensors using an ac microelectromechanical system flux concentrator"
[66] M. Marolt and Z. Jaglicic, University of Ljubljana Faculty of Mathematics and Physics (2014). "Superparamagnetic materials"
[67] J. Cao, Y. Liu, Y. Ren, F. Wei, and P. Freitas, Applied surface science **314**, 443 (2014). "Effect of annealing temperature on formation of superparamagnetism in CoFeB/MgO/CoFeB magnetic tunnel junctions"
[68] X. Liu, C. Ren, and G. Xiao, Journal of Applied Physics **92** (8), 4722 (2002). "Magnetic tunnel junction field sensors with hard-axis bias field"
[69] Z. Zeng, P. Khalili Amiri, J. Katine, J. Langer, K. Wang, and H. Jiang, Applied Physics Letters **101** (6), 062412 (2012). "Nanoscale magnetic tunnel junction sensors with perpendicular anisotropy sensing layer"
[70] W. Skowroński, P. Wiśniowski, T. Stobiecki, S. Cardoso, P.P. Freitas, and S. van Dijken, Applied Physics Letters **101** (19), 192401 (2012). "Magnetic field sensor with voltage-tunable sensing properties"
[71] X. Zhu, Z. Liu, V. Metlushko, P. Grütter, and M.R. Freeman, Physical Review B **71** (18), 180408 (2005). "Broadband spin dynamics of the magnetic vortex state: Effect of the pulsed field direction"
[72] W. Hiebert, A. Stankiewicz, and M. Freeman, Physical Review Letters **79** (6), 1134 (1997). "Direct observation of magnetic relaxation in a small permalloy disk by time-resolved scanning Kerr microscopy"
[73] K.Y. Guslienko, V. Novosad, Y. Otani, H. Shima, and K. Fukamichi, Physical Review B **65** (2), 024414 (2001). "Magnetization reversal due to vortex nucleation, displacement, and annihilation in submicron ferromagnetic dot arrays"

[74] K.Y. Guslienko, X. Han, D. Keavney, R. Divan, and S. Bader, Physical review letters **96** (6), 067205 (2006). "Magnetic vortex core dynamics in cylindrical ferromagnetic dots"
[75] K.Y. Guslienko and K.L. Metlov, Physical Review B **63** (10), 100403 (2001). "Evolution and stability of a magnetic vortex in a small cylindrical ferromagnetic particle under applied field"
[76] N.A. Usov, C.-R. Chang, and Z.-H. Wei, Journal of Applied Physics **89** (11), 7591 (2001). "Nonuniform magnetization structures in thin soft type ferromagnetic elements of elliptical shape"
[77] G. Hrkac, P.S. Keatley, M.T. Bryan, and K. Butler, Journal of Physics D: Applied Physics **48** (45), 453001 (2015). "Magnetic vortex oscillators"
[78] P. Wiśniowski, J. Almeida, S. Cardoso, N. Barradas, and P. Freitas, Journal of Applied Physics **103** (7), 07A910 (2008). "Effect of free layer thickness and shape anisotropy on the transfer curves of MgO magnetic tunnel junctions"
[79] D. Guo, F. Cardoso, R. Ferreira, E. Paz, S. Cardoso, and P. Freitas, Journal of Applied Physics **115** (17), 17E513 (2014). "MgO-based magnetic tunnel junction sensors array for non-destructive testing applications"
[80] W. Zhang, G. Xiao, and M.J. Carter, Physical Review B **83** (14), 144416 (2011). "Two-dimensional field-sensing map and magnetic anisotropy dispersion in magnetic tunnel junction arrays"
[81] S. van Dijken and J. Coey, Applied Physics Letters **87** (2), 022504 (2005). "Magnetoresistance sensor with an out-of-plane magnetized sensing layer"
[82] A.V. Silva, D.C. Leitao, J. Valadeiro, J. Amaral, P.P. Freitas, and S. Cardoso, The European Physical Journal Applied Physics **72** (1), 10601 (2015). "Linearization strategies for high sensitivity magnetoresistive sensors"
[83] C.-Y. Yang, S.-J. Chang, M.-H. Lee, K.-H. Shen, S.-Y. Yang, H.-J. Lin, and Y.-C. Tseng, Scientific reports **5**, 17169 (2015). "Competing anisotropy-tunneling correlation of the CoFeB/MgO perpendicular Magnetic tunnel junction: An electronic approach"
[84] O. Bultynck, M. Manfrini, A. Vaysset, J. Swerts, C.J. Wilson, B. Sorée, M. Heyns, D. Mocuta, I.P. Radu, and T. Devolder, Physical Review Applied **10** (5), 054028 (2018). "Instant-on spin torque in noncollinear magnetic tunnel junctions"
[85] Y. Fu, I. Barsukov, J. Li, A. Gonçalves, C. Kuo, M. Farle, and I. Krivorotov, Applied Physics Letters **108** (14), 142403 (2016). "Temperature dependence of perpendicular magnetic anisotropy in CoFeB thin films"
[86] S. Peng, M. Wang, H. Yang, L. Zeng, J. Nan, J. Zhou, Y. Zhang, A. Hallal, M. Chshiev, and K.L. Wang, Scientific reports **5**, 18173 (2015). "Origin of interfacial perpendicular magnetic anisotropy in MgO/CoFe/metallic capping layer structures"
[87] M. Wang, Y. Zhang, X. Zhao, and W. Zhao, Micromachines **6** (8), 1023 (2015). "Tunnel junction with perpendicular magnetic anisotropy: Status and challenges"
[88] J. Chen, S. Peng, D. Xiong, H. Cheng, H. Zhou, Y. Jiang, J. Lu, W. Li, and W. Zhao, Journal of Physics D: Applied Physics (2020). "Correlation of interfacial perpendicular magnetic anisotropy and interlayer exchange coupling in CoFe/W/CoFe structures"
[89] T. Nakano, M. Oogane, H. Naganuma, and Y. Ando, IEEE Transactions on Magnetics **51** (11), 1 (2015). "Systematic investigation on correlation between sensitivity and nonlinearity in magnetic tunnel junction for magnetic sensor"

[90] A. Khvalkovskiy, D. Apalkov, S. Watts, R. Chepulskii, R. Beach, A. Ong, X. Tang, A. Driskill-Smith, W. Butler, and P. Visscher, Journal of Physics D: Applied Physics **46** (7), 074001 (2013). "Basic principles of STT-MRAM cell operation in memory arrays"
[91] D. Apalkov, B. Dieny, and J. Slaughter, Proceedings of the IEEE **104** (10), 1796 (2016). "Magnetoresistive random access memory"
[92] F. Matsukura, Y. Tokura, and H. Ohno, Nature nanotechnology **10** (3), 209 (2015). "Control of magnetism by electric fields"
[93] G. Yu, P. Upadhyaya, Y. Fan, J.G. Alzate, W. Jiang, K.L. Wong, S. Takei, S.A. Bender, L.-T. Chang, and Y. Jiang, Nature nanotechnology **9** (7), 548 (2014). "Switching of perpendicular magnetization by spin–orbit torques in the absence of external magnetic fields"
[94] W.-G. Wang, M. Li, S. Hageman, and C. Chien, Nature materials **11** (1), 64 (2012). "Electric-field-assisted switching in magnetic tunnel junctions"
[95] Z. Wang, W. Zhao, E. Deng, J.-O. Klein, and C. Chappert, Journal of Physics D: Applied Physics **48** (6), 065001 (2015). "Perpendicular-anisotropy magnetic tunnel junction switched by spin-Hall-assisted spin-transfer torque"
[96] Y. Shiota, T. Nozaki, F. Bonell, S. Murakami, T. Shinjo, and Y. Suzuki, Nature materials **11** (1), 39 (2012). "Induction of coherent magnetization switching in a few atomic layers of FeCo using voltage pulses"
[97] K. Wang, J. Alzate, and P.K. Amiri, Journal of Physics D: Applied Physics **46** (7), 074003 (2013). "Low-power non-volatile spintronic memory: STT-RAM and beyond"
[98] H. Yang, M. Chshiev, B. Dieny, J. Lee, A. Manchon, and K. Shin, Physical Review B **84** (5), 054401 (2011). "First-principles investigation of the very large perpendicular magnetic anisotropy at Fe| MgO and Co| MgO interfaces"
[99] K. Khoo, G. Wu, M. Jhon, M. Tran, F. Ernult, K. Eason, H.J. Choi, and C. Gan, Physical Review B **87** (17), 174403 (2013). "First-principles study of perpendicular magnetic anisotropy in CoFe/MgO and CoFe/Mg 3 B 2 O 6 interfaces"
[100] A. Guedes, J. Almeida, S. Cardoso, R. Ferreira, and P. Freitas, IEEE transactions on magnetics **43** (6), 2376 (2007). "Improving magnetic field detection limits of spin valve sensors using magnetic flux guide concentrators"
[101] G. He, Y. Zhang, L. Qian, G. Xiao, Q. Zhang, J.C. Santamarina, T.W. Patzek, and X. Zhang, Applied Physics Letters **113** (24), 242401 (2018). "PicoTesla magnetic tunneling junction sensors integrated with double staged magnetic flux concentrators"
[102] R. Chaves, P. Freitas, B. Ocker, and W. Maass, Applied Physics Letters **91** (10), 102504 (2007). "Low frequency picotesla field detection using hybrid MgO based tunnel sensors"
[103] J. Almeida and P. Freitas, J. Appl. Phys. **105** (7), 07E722 (2009). "Field detection in MgO magnetic tunnel junctions with superparamagnetic free layer and magnetic flux concentrators"
[104] H. Nhalil, T. Givon, P.T. Das, N. Hasidim, V. Mor, M. Schultz, S. Amrusi, L. Klein, and A. Grosz, IEEE Sensors Letters **3** (12), 1 (2019). "Planar Hall effect magnetometer with 5 pT resolution"
[105] K. Wang, L. Qian, S.-C. Ying, and G. Xiao, Physical Review B **102** (14), 144430 (2020). "Manipulation of the interlayer exchange coupling in perpendicular magnetized thin films via tunable magnetic-layer and spacer thicknesses"

[106] A. Vansteenkiste, J. Leliaert, M. Dvornik, M. Helsen, F. Garcia-Sanchez, and B. Van Waeyenberge, AIP advances **4** (10), 107133 (2014). "The design and verification of MuMax3"

[107] T. Pokhil, D. Song, and J. Nowak, Journal of Applied Physics **87** (9), 6319 (2000). "Spin vortex states and hysteretic properties of submicron size NiFe elements"

[108] J.C. Slonczewski, Physical Review B **39** (10), 6995 (1989). "Conductance and exchange coupling of two ferromagnets separated by a tunneling barrier"

[109] W. Zhang, Q. Hao, and G. Xiao, Physical Review B **84** (9), 094446 (2011). "Low-frequency noise in serial arrays of MgO-based magnetic tunnel junctions"

[110] H. Weitensfelder, H. Brueckl, A. Satz, K. Pruegl, J. Zimmer, S. Luber, W. Raberg, C. Abert, F. Bruckner, and A. Bachleitner-Hofmann, Physical Review Applied **10** (5), 054056 (2018). "Comparison of Sensitivity and Low-Frequency Noise Contributions in Giant-Magnetoresistive and Tunneling-Magnetoresistive Spin-Valve Sensors with a Vortex-State Free Layer"

[111] R. Stearrett, W. Wang, X. Kou, J. Feng, J. Coey, J. Xiao, and E. Nowak, Physical Review B **86** (1), 014415 (2012). "Influence of exchange bias on magnetic losses in CoFeB/MgO/CoFeB tunnel junctions"

[112] S. Ingvarsson, G. Xiao, S. Parkin, W. Gallagher, G. Grinstein, and R. Koch, Physical review letters **85** (15), 3289 (2000). "Low-frequency magnetic noise in micron-scale magnetic tunnel junctions"

[113] M. Wang, Y. Zhang, X. Zhao, and W. Zhao, Micromachines **6** (8), 1023 (2015). "Tunnel junction with perpendicular magnetic anisotropy: Status and challenges"

[114] J. Chatterjee, S. Auffret, R. Sousa, P. Coelho, I.-L. Prejbeanu, and B. Dieny, Scientific reports **8** (1), 1 (2018). "Novel multifunctional RKKY coupling layer for ultrathin perpendicular synthetic antiferromagnet"

[115] D. Mazumdar, W. Shen, X. Liu, B. Schrag, M. Carter, and G. Xiao, Journal of applied physics **103** (11), 113911 (2008). "Field sensing characteristics of magnetic tunnel junctions with (001) MgO tunnel barrier"

[116] P. Wisniowski, J. Wrona, T. Stobiecki, S. Cardoso, and P. Freitas, IEEE transactions on magnetics **48** (11), 3840 (2012). "Magnetic tunnel junctions based on out-of-plane anisotropy free and in-plane pinned layer structures for magnetic field sensors"

[117] Y. Zhang, K. Wang, and G. Xiao, Applied Physics Letters **116** (21), 212404 (2020). "Noise characterization of ultrasensitive anomalous Hall effect sensors based on Co40Fe40B20 thin films with compensated in-plane and perpendicular magnetic anisotropies"

[118] K. Wang, Y. Zhang, and G. Xiao, Physical Review Applied **13** (6), 064009 (2020). "Anomalous Hall Sensors with High Sensitivity and Stability Based on Interlayer Exchange-Coupled Magnetic Thin Films"

[119] J.G. Alzate, P. Khalili Amiri, G. Yu, P. Upadhyaya, J.A. Katine, J. Langer, B. Ocker, I.N. Krivorotov, and K.L. Wang, Applied physics letters **104** (11), 112410 (2014). "Temperature dependence of the voltage-controlled perpendicular anisotropy in nanoscale MgO| CoFeB| Ta magnetic tunnel junctions"

[120] H. Liu, R. Wang, P. Guo, Z. Wen, J. Feng, H. Wei, X. Han, Y. Ji, and S. Zhang, Scientific reports **5**, 18269 (2015). "Manipulation of magnetization switching and tunnel magnetoresistance via temperature and voltage control"

[121] Z. Lei, G. Li, W.F. Egelhoff, P. Lai, and P.W. Pong, IEEE Transactions on Magnetics **47** (3), 602 (2011). "Review of noise sources in magnetic tunnel junction sensors"
[122] G. Xiao, (2012). "Magnetoresistive sensors based on magnetic tunneling junctions"
[123] Y. Lu, X. Li, G. Xiao, R. Altman, W. Gallagher, A. Marley, K. Roche, and S. Parkin, Journal of applied physics **83** (11), 6515 (1998). "Bias voltage and temperature dependence of magnetotunneling effect"
[124] Y. Sakuraba, K. Takanashi, Y. Kota, T. Kubota, M. Oogane, A. Sakuma, and Y. Ando, Physical Review B **81** (14), 144422 (2010). "Evidence of Fermi level control in a half-metallic Heusler compound Co 2 MnSi by Al-doping: Comparison of measurements with first-principles calculations"
[125] D. Vodenicarevic, N. Locatelli, A. Mizrahi, J.S. Friedman, A.F. Vincent, M. Romera, A. Fukushima, K. Yakushiji, H. Kubota, and S. Yuasa, Physical Review Applied **8** (5), 054045 (2017). "Low-energy truly random number generation with superparamagnetic tunnel junctions for unconventional computing"
[126] B. Parks, M. Bapna, J. Igbokwe, H. Almasi, W. Wang, and S.A. Majetich, AIP Advances **8** (5), 055903 (2018). "Superparamagnetic perpendicular magnetic tunnel junctions for true random number generators"
[127] B. Wu, Y. Wang, X. Liu, and C. He, Smart Materials and Structures **24** (7), 075007 (2015). "A novel TMR-based MFL sensor for steel wire rope inspection using the orthogonal test method"
[128] L.S. Rosado, F.A. Cardoso, S. Cardoso, P.M. Ramos, P.P. Freitas, and M. Piedade, Sensors and Actuators A: Physical **212**, 58 (2014). "Eddy currents testing probe with magneto-resistive sensors and differential measurement"
[129] M.A.I. Mohd Noor Sam, Z. Jin, M. Oogane, and Y. Ando, Sensors **19** (21), 4718 (2019). "Investigation of a Magnetic Tunnel Junction Based Sensor for the Detection of Defects in Reinforced Concrete at High Lift-Off"
[130] S.D. Nair, T. Patzek, and E. van Oort, (2017). "Detecting Poor Cement Bonding and Zonal Isolation Problems Using Magnetic Cement Slurries"
[131] C. Vipulanandan and A. Mohammed, Smart Materials and Structures **24** (12), 125020 (2015). "Smart cement modified with iron oxide nanoparticles to enhance the piezoresistive behavior and compressive strength for oil well applications"
[132] H.Q. Pham, B.V. Tran, D.T. Doan, Q.N. Pham, K. Kim, C. Kim, F. Terki, and Q.H. Tran, IEEE Transactions on Magnetics **54** (6), 1 (2018). "Highly sensitive planar Hall magnetoresistive sensor for magnetic flux leakage pipeline inspection"
[133] E.Y. Tsymbal and I. Zutic, *Handbook of spin transport and magnetism*. (CRC press, 2011).
[134] H.G. Meyer, R. Stolz, A. Chwala, and M. Schulz, physica status solidi (c) **2** (5), 1504 (2005). "SQUID technology for geophysical exploration"
[135] T. Eltsov and T. Patzek, presented at the SPE Middle East Oil and Gas Show and Conference, 2019 (unpublished).
[136] S.D. Nair, T. Patzek, and E. van Oort, (2017). "Detecting Poor Cement Bonding and Zonal Isolation Problems Using Magnetic Cement Slurries"